The Zebrafish Larva as a Model System for Myeloid Malignancies

Jan-Lukas Førde

Thesis for the degree of Philosophiae Doctor (PhD)
University of Bergen, Norway
2024

UNIVERSITY OF BERGEN

The Zebrafish Larva as a Model System for Myeloid Malignancies

Jan-Lukas Førde

Thesis for the degree of Philosophiae Doctor (PhD)
at the University of Bergen

Date of defense: 23.02.2024

Year: 2024

Title: The Zebrafish Larva as a Model System for Myeloid Malignancies

Name: Jan-Lukas Førde

Print: Skipnes Kommunikasjon / University of Bergen

Scientific environment

This work was performed at the Herfindal Lab, located at the Department of Clinical Science, Faculty of Medicine, University of Bergen, with Prof. Lars Herfindal as main supervisor and Assoc. Astrid Marta Olsnes as co-supervisor.

Funding for the presented work was provided by a three-year PhD grant awarded by the Western Norway Regional Health Authority and managed by Helse Bergen (Grant no. F-12533). Additional funding was supplied by the NordForsk Nordic Center of Excellence "NordAqua" (Paper I), 'Astri og Edvard Riisøens legat" (Paper I), and the Norwegian Society for Children's Cancer (Paper I and II).

Work on EHop-016 was done in close collaboration with Anette Lodvir Hemsing and Prof. Håkon Reikvam, also part of the Department of Clinical Science, leading to a shared first authorship with Hemsing in Paper II. Work on Paper III was done in collaboration with PhD Abdelnour Alhourani and Assoc. Prof Hanne Røland Hagland at the University of Stavanger. For the same paper, work on creating transgenic zebrafish was done in collaboration with Prof. Kari Espolin Fladmark at the Department of Biological Sciences (University of Bergen), while graphene materials and characterization thereof was provided by Tian Carey, University of Cambridge.

Acknowledgments

I would like to express my sincere gratitude to the following individuals, without whom the completion of my PhD thesis would not have been possible:

First and foremost, I extend my deep appreciation to my main supervisor Prof. Lars Herfindal and co-supervisor Prof. Astrid Marta Olsnes, for their invaluable knowledge, support, and constant encouragement. I especially thank Prof. Lars Herfindal for his availability around the clock and swift, comprehensive feedback which has been instrumental for my research.

My profound thanks go to all members of my research group during this journey. Reidun Æsøy, Edvin Tang Gundersen, Ronja Bjørnstad and Ingeborg Nerbø Reiten, your friendship and assistance have been the pillars of my academic experience. Special gratitude is due to my fellow PhD student Ingeborg Nerbø Reiten, with whom I shared the journey of establishing the zebrafish model in our laboratory and who has been my ever-reliable office neighbor and lunch companion.

I am grateful to Prof. Kari Espolin Fladmark for her support in all matters related to zebrafish and her significant aid in the development of the transgenic zebrafish line, and Anette Lodvir Hemsing with whom I extensively collaborated on Paper II. My heartfelt thanks also go to Assoc. Hanne Røland Hagland and Dr. Abdelnour Alhourani, with whom I have enjoyed a close collaboration since my master's studies, particularly in all aspects related to biomedical research of graphene.

Lastly, I want to acknowledge the unwavering support of my friends and family, who provided me with motivation and encouragement, especially during the challenging initial phases of my PhD during the pandemic. Your support has been a source of strength throughout.

Thank you all for being a part of this remarkable journey and for your invaluable contributions to my academic and personal growth.

Jan-Lukas Førde
Bergen, October 2023

Abstract

English

Acute myeloid leukemia (AML) and myelodysplastic neoplasms are cancers of myeloid progenitor cells in the bone marrow. These diseases are most frequently diagnosed in older patients and are characterized by poor prognoses. The current treatment regimens of chemotherapy or hematopoietic stem cell transplantation are often poorly tolerated by older patients, which fuels the need for novel treatment options. Zebrafish larvae have seen ever increasing usage as an animal model for drug development. Compared to other animal models such as mice, this model excels through its small size and transparency facilitating imaging of fluorescent cells *in vivo*, and short time needed for experiments. In this work we aimed to refine and evaluate the use of zebrafish larvae as a myeloid malignancy model. For this, our objectives were to develop a new software tool to improve data acquisition, followed by the validation of this software through investigation of a novel drug, EHop-016, and a nano-sized drug delivery system (NDDS), graphene.

Our software tool proved to be vital for our work. Using this tool, we were able to segment and measure single cells from confocal images of larvae and position them in three dimensions, greatly improving the quality of the collected data, and thereby the value of the following studies. In our investigation of EHop-016, this model demonstrated that the *in vitro* findings on the drug's effects on AML cells were possible to reproduce *in vivo* in zebrafish larvae. This includes both the ability of AML cells to migrate, as well as the efficiency of a combination of EHop-016 and daunorubicin. For investigation of the NDDS graphene, our research focused on the biodistribution and immunoreactivity of two different production methods for the material. Here, we found less immunoreactivity in samples produced through microfluidization compared to sonication. Using a zebrafish larvae model with fluorescent macrophages, we found an increased macrophage production following exposure to sonicated graphene. Taken together, the work presented in this thesis demonstrates the value of the zebrafish model for treatment development against myeloid malignancies through its flexibility and valuable insights gained from its

combination of single cell studies in an *in vivo* environment. The software tool we developed greatly aided in this research and will be a valuable asset in future early preclinical *in vivo* studies on cancer therapy development.

Norwegian

Myeloid kreft er ein ukontrollert deling av dei myeloide stamcellene som finst i beinmergen. Døme på myeloid kreft er akutt myeloid leukemi (AML) og myelodysplastisk syndrom. Desse kreftformane er vanlegast hjå eldre pasientar og er assosierte med dårlege prognosar. Dei noverande behandlingane består av kjemoterapi eller hematopoietisk stamcelletransplantasjon, begge tøffe behandlingar som vert dårleg tolerert av eldre og skrøpelege pasientar, og det einaste alternativet for mange er ikkje-kurativ behandling. Det er altså eit stort behov for nye behandlingsalternativ for myeloide kreftformer. I det siste har sebrafisklarver vorte populær innan legemiddelutvikling som ein modell for tidleg *in vivo* utprøving. Samanlikna med andre dyremodellar som mus, har sebrafisklarver fleire fordelar som liten storleik, og transparens, som mogleggjer avbilding av fluorescerande celler *in vivo.* Vidare kan ein oppnå resultat i løpet av dagar i staden for månader. I dette arbeidet hadde vi som mål å forbetra sebrafisklarver som modell for myeloid kreft, samt evaluera våre nye verktøy. Dette gjennomførte vi ved å utvikle et nytt programvareverktøy for å forbetre datainnsamlinga og handsaminga, etterfølgt av validering av denne programvara gjennom undersøkinga av ein ny legemiddelkandidat, EHop-016, og ein legemiddelbærar, grafén. Vårt programvareverktøy viste seg å være avgjerande for vårt arbeid. Ved hjelp av dette verktøyet kunne vi raskt segmentera og måla celler frå konfokalbilete av larver, som vidare gav betydeleg forbetra utbyttet av dei påfølgande studiane. I vår undersøking av EHop-016 viste denne modellen at EHop-016 hadde evne til å hemma migrasjon av AML-celler frå blodet til den hematopoietiske nisja. En kombinasjonsstudie med daunorubisin *in vitro* synte synergistiske effektar, noko vi også kunne demonstrera i sebrafisklarver. For undersøkinga av legemiddelbæraren grafén, ønskte vi å studera i kva grad to ulike produksjonsmetodar påverkja biodistribusjonen og immuninteraksjonar. Her fant vi mindre immunreaktivitet i prøver produsert gjennom

mikrofluidisering samanlikna med sonikering. Ved bruk av sebrafisklarver med fluorescerande makrofager karakteriserte vi desse interaksjonane nærmare og fant eit auka tal av makrofager etter eksponering for sonikert grafén. Vårt arbeid demonstrerte verdien av sebrafiskmodellen for tidleg utvikling av nye behandlingsmåtar mot myeloid kreft. Modellen er fleksibel, og særskildt bruken av fluorescerande celler og monitorering av desse *in situ* i levande larver gjer verdfull innsikt. Programvareverktøyet vi utvikla, var til stor hjelp i denne forskinga og vil vera ein verdifull ressurs i slike studiar framover.

List of publications

Paper I:

Førde JL, Reiten IN, Fladmark KE, Kittang AO, Herfindal L. **A new software tool for computer assisted in vivo high-content analysis of transplanted fluorescent cells in intact zebrafish larvae**. Biol Open. 2022 Dec 15;11(12):bio059530. Doi: 10.1242/bio.059530. Epub 2022 Dec 13. PMID: 36355409; PMCID: PMC9770244.

Paper II:

Hemsing AL, **Førde JL**, Reikvam H, Herfindal L. **The Rac1-inhibitor EHop-016 attenuates AML cell migration and enhances the efficacy of daunorubicin in MOLM-13 transplanted zebrafish larvae**. Transl Oncol 2023 (under review).

Paper III:

Førde JL, Alhourani A, Carey T, Arbab A, Fladmark KE, Silje S, Mollnes TE, Herfindal L, Hagland H R. **Impact of the graphene production methods sonication and microfluidization on in vitro and in vivo toxicity and immunoreactivity**. (Manuscript)

Contents

Abbreviations

3D:	Three-dimensional
AFM:	Atomic force microscopy
AML:	Acute myeloid leukemia
A-V:	Annexin-V
Aza:	Azacytidine
CHT:	Caudal hematopoietic tissue
CMC:	Carboxymethylcellulose salt
DA:	Dorsal aorta
DLS:	Dynamic light scattering
DNR:	Daunorubicin
dpf:	Days post fertilization
FFT:	Fast Fourier transform
FITC:	Fluorescein isothiocyanate
FLT3:	FMS-like tyrosine kinase 3
FLT3-ITD:	FLT3 internal tandem duplication
For:	Formazan
HCT:	Hematopoietic stem cell transplantation
hpf:	Hours post fertilization
HUVECs:	Human umbilical vein endothelial cells
IL-3:	Interleukin-3
IV:	Intravenous
Len:	Lenalidomide
MDS:	Myelodysplastic neoplasms
MTD:	Maximum tolerable dose
NDDS:	Nano-sized drug delivery system
P:	Phosphatidylserine
PBI:	Posterior blood island
PCV:	Posterior cardinal vein
PI:	Propidium iodide
PM:	1-methoxy phenazinium methylsulfate

Prim:	Primordium
Rac1:	Ras-related C3 botulinum toxin substrate 1
SDC:	Sodium deoxycholate
SDF-1:	Stromal cell-derived factor 1
SEM:	Scanning electron microscopy
T:	Thymidine
Tet:	Tetrazolium salt
WST-8:	Water soluble tetrazolium salt 8

1 Introduction

Myeloid malignancies such as acute myeloid leukemia (AML) and myelodysplastic neoplasms (MDS, previously called myelodysplastic syndromes) are cancers that arise from myeloid stem cells in the bone marrow. Like other cancers, these diseases are highly individual, and necessitate a wide range of treatments suitable for the given mutations and contributing factors such as patient age, genetic background, and other conditions [1, 2]. Nevertheless, for treatment of a disease such as AML, the backbone remains a chemotherapy regimen developed more than 50 years ago [1, 3].

In the early phase of drug development, a multitude of compounds are tested for activity towards relevant targets, such as cancer cells, adverse effects, and practical feasibility, such as cost or solubility. Eventually, this process leads to the identification of promising compounds that enter animal studies and possibly clinical trials in humans [4]. In this early development process, *in vitro* experiments are highly effective, but even with recent advances, the model systems are lacking the complexity of an entire organism, and more advanced models can become costly [5]. *In Vivo* research in animals such as mice can be a more suitable stand-in for humans but performs poorly in large scale screening due to a high demand of time and money, as well as ethical concerns [5, 6]. A model organism combining benefits from both *in vitro* and *in vivo* models is the zebrafish larva.

1.1 The zebrafish

The zebrafish, (*Danio rerio)*, is a small freshwater fish, native to the tropical and subtropical regions of South Asia (Figure 1A) [7]. These fish are popular in aquariums, where they are especially suitable due to their ease of breeding and resilience to a wide range of water temperatures and conditions [8]. As vertebrates, zebrafish belong to the same subphylum as humans [7]. To illustrate the evolutionary connections between zebrafish, humans and other animals used in research, a phylogenic tree is shown in Figure 1B.

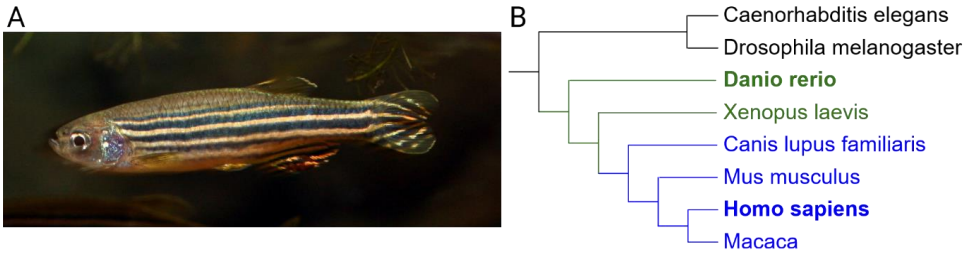

Figure 1: Overview of the zebrafish. A mature female zebrafish is shown in A [9]. In B, a phylogenic tree is shown, illustrating the evolutionary connection between humans (Homo sapiens), zebrafish (Danio rerio) and other laboratory animals. Vertebrates and mammals are shown in green and blue respectively (created using [10] and BioRender.com).

In this project, the focus is on zebrafish in the embryonal and larval stages of development. A detailed description of the developmental process from the single cell zygote to a hatched larva was published by Kimmel *et al*. in 1995 [11]. Here we give a brief summation, highlighting the important stages relevant for our research. An approximate time following fertilization is given for the highlighted stages as hours post fertilization (hpf) or days post fertilization (dpf), however, even embryos of a clonal strain can develop at different rates. Furthermore, the time is given for development at 28.5 °C, with higher and lower temperatures increasing and decreasing the development rate respectively [11].

The one-cell stage (0 hpf): Following fertilization of the zebrafish egg, the chorion lifts from the yolk sack and fertilized egg cell (Figure 2, Zygote), and the single cell starts to divide after approximately 45 minutes. It is prior to this first division that genetic modification, such as via the Tol2 transposon system, can be performed [12].

The cells continue to divide, first forming a dome on top of the yolky region of the egg (Figure 2, 256-cell), before completely encompassing it at approximately 10 hpf (Figure 2, Bud stage). At this stage, the segmentation period begins and lasts until 24 hpf. During this period, the somites, early stages of the vertebrae, are formed, and early indications of head, tail and organs become visible.

Pharyngula period (24 hpf – 48 hpf): In the pharyngula period, the tail elongates, and extensive organogenesis takes place, where among other organs the brain and

heart are formed. The heart starts to beat early in this period and major blood vessels are taking shape, with blood circulation starting prior to 30 hpf. Hematopoiesis is now transitioning from primitive to definitive stage, starting in the posterior blood island (PBI) and dorsal aorta (DA) (Figure 2, Prim-5) [13].

Hatching period (2 dpf – 3 dpf): Following the pharyngula period, most of the early organ development, apart from the gut and related organs, is completed. Usually, the embryos also hatch from their chorion during this period, the precise time of hatching is however not definitely linked to a certain developmental event and happens sporadically during this stage. Early in this period, hematopoiesis starts in the caudal hematopoietic tissue (CHT) (Figure 2, Long pec) [13].

Early larval period (3dpf – 5 dpf): During the early larval period most of the larva's morphogenesis is completed, and the larva starts to move more actively. Hematopoiesis now also starts in the thymus and kidney at three and four dpf respectively [13]. During this development, the yolk sac diminishes, and at approximately five dpf, the larva is capable of independent feeding (Figure 2, Larva at five dpf) [14].

The point where the larva is capable of independent feeding is an important zebrafish development stage for researchers. This marks the point where the zebrafish larva is sufficiently developed to be included in Article 1(3)(a)(i) of Directive 2010/36/EU on the protection of animals in research [15]. Prior to this, zebrafish embryos and larvae are not considered research animals in respect to regulations.

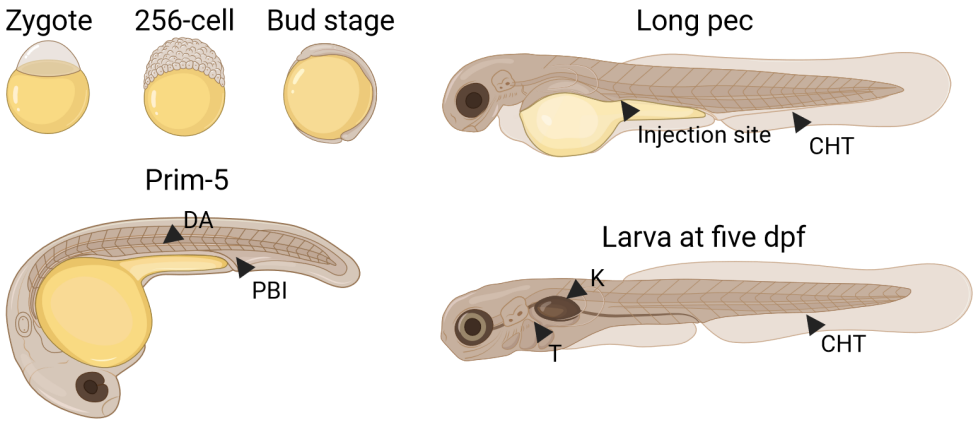

Figure 2: Development of the zebrafish larva. Different stages of zebrafish development are shown as classified by Kimmel *et al*. [11]. Following fertilization, the single cell zygote starts to divide, and after 2.5 hours, or eight cell division cycles, arrives at the 256-cell stage. The cells continue to divide, and gradually start to encapsulate the yolky part of the egg. At 10 hours post fertilization (hpf), the yolk is fully encapsulated, and the tail bud becomes visible, giving name to the bud stage. The pharyngula period starts at 24 hpf, here, the most accurate staging is done by observing the posterior lateral line primordium (prim) migrating towards the posterior end of the embryo. Staging is performed by counting the number of somites the primordium has passed, such as the prim-5 stage at 24 hpf. At approximately 48 hpf, the embryo enters the hatching period. The early staging in this period is determined by the development of the pectoral fin. In the long pec stage, at 48 hpf, the pectoral fin bud, while not looking like a fin at this point, has elongated. The final illustration depicts a larva at five days post fertilization. Arrows indicate the site of injection in the long pec stage, and the hematopoietic sites: dorsal aorta (DA), posterior blood island (PBI), caudal hematopoietic tissue (CHT), kidney (K) and thymus (T) [13]. The figure was created using BioRender.com.

1.1.1 Zebrafish as a model for human diseases

The use of animals in medical research is a vital part to bridge the gap between *in vitro* studies and clinical studies in humans [6]. While the animal used largely depends on the research goals of a study, common animals are rodents like mice, rats, rabbits, and guinea pigs [16]. The use of zebrafish as a research animal has been steadily growing. While these animals are not as phylogenetically close to humans as other options (Figure 1B), they still share the common vertebrate heritage, and with 70% shared genome and 80% of human proteins having an orthologue in zebrafish, they are a relevant model for several human disorders, such as deafness, epilepsy, and cancer [7]. This is also true for research on hematopoietic aspects, and despite the

different locations of the hematopoietic niches, their signaling molecules, transcription factors and genetic processes controlling hematopoiesis are highly conserved [13].

Zebrafish make up for the more distant genetic relationship with humans by multiple benefits compared to other research animals. The main benefits being their small size, ease and low cost of maintenance, external fertilization of eggs, subsequent ease of genetic modification, and their optically transparent skin during the early developmental stages, which can even persist throughout adulthood for genetically modified strains such as casper [7, 12, 17]. Using the wide range of available genetic modifications for zebrafish, the model animal can be tailored to fit the given experiments by for example expressing fluorescence in desired cell types, expressing human signaling molecules or be modified with organism wide reporter genes [7, 18].

For cancer research, zebrafish in the embryonic and larval stage are particularly useful since the absence of an adaptive immune system until three weeks following fertilization allows for transplantation of human cancer cells without producing an immune reaction [19]. With their small size and transparency during these stages of development, this allows for large scale experiments to be carried out in 96-well plates and anatomical and physiological changes observed by conventional microscopy without the need to euthanize the animal. Furthermore, fluorescent objects like stained cells can be tracked throughout the organism using fluorescence microscopy.

1.2 Myeloid malignancies

Cancer is a disease in which healthy cells malfunction in a way that induces uncontrolled cell division [20]. Usually, these mutated cells are killed by programmed cell death, apoptosis, initiated either through intracellular mechanisms or by the immune system [21, 22]. However, if the mutated cells are able to evade apoptosis, cell division can continue unchecked. The growth of this malfunctioning cell population, and potential spread to other tissues, interferes with the normal function of the human body, and thus leads to the severe symptoms of cancer [20]. For this work, the focus is

on cancers originating in myeloid progenitor cells. In healthy individuals, these cells are part of the machinery producing blood cells, a process called hematopoiesis.

1.2.1 Hematopoiesis

The bone marrow is a soft tissue found in the medullary cavity and cancellous tissue of long and axial bones. Surrounded by venous sinuses, it hosts the hematopoietic islands, which in humans, and other mammals, serve as the main site of formation of the cellular blood components [23].

Hematopoiesis starts with the hematopoietic stem cell. This self-renewing stem cell produces the progenitor cells for the two lineages of blood cells, the myeloid and lymphoid cell lineage (Figure 3). Following a chain of committed progenitor cells, the common myeloid progenitor and common lymphoid progenitor, differentiate into the megakaryocytes, erythrocytes, granulocytes and monocytes in the myeloid lineage, and B-cells, T-cells and natural killer cells in the lymphoid lineage [24].

To facilitate and control the production, differentiation and maturation of blood cells, the microenvironment of the bone marrow supplies a myriad of growth factors and chemokines. For this project, two of these signaling molecules are especially of interest: Interleukin-3 (IL-3), a growth factor facilitating the proliferation of various hematopoietic progenitor cell lineages, and the stromal cell-derived factor 1 (SDF-1), a signaling molecule used as an attractant for hematopoietic stem cells [25, 26].

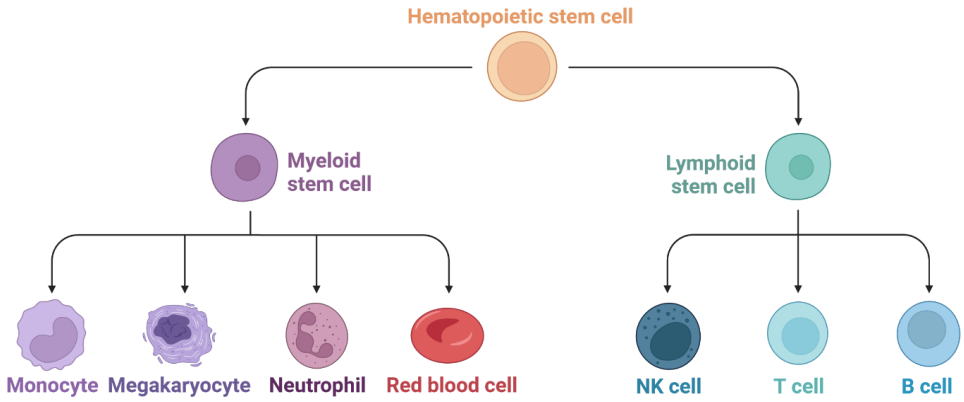

Figure 3: Overview of hematopoiesis. The hematopoietic stem cell undergoes self-renewal and produces the progenitors of the myeloid and lymphoid cell lineages [24]. Through a chain of progenitor cells (not shown in figure) these stem cells produce the monocytes, megakaryocytes, neutrophils, red blood cells, NK cells, T cells and B cells. The figure was created using BioRender.com.

1.2.2 Leukemias

Leukemias are cancers that originate from progenitor cells that are part of the hematopoietic process and naturally reside in the bone marrow. When a hematopoietic progenitor cell becomes cancerous, its further differentiation into functional blood cells is halted. Instead, these cells start proliferating. This proliferation of non-functional cells in the bone marrow leads to the suppression of functional progenitor cells by depriving the bone marrow of space and nutrients, thereby leading to cytopenia. From the lack of functional blood cells, the common symptoms of leukemia such as fatigue, frequent infections, and bleeding originate, which in turn can lead to death [20, 27].

The classification of leukemias is still under debate with multiple classification systems coexisting [28, 29]. In general, leukemias can be divided into four main categories, depending on the cell linage affected, underlying genetics, and disease progression. Chronic leukemias usually result in a slower disease progression and better prognosis compared to acute leukemias. In acute leukemias the blast count can be higher, usually above 20% in the bone marrow. This form of leukemia is characterized by a more aggressive growth and comparatively poor prognosis.

Depending on the hematopoietic lineages from which the cancer originate, we divide between myeloid and lymphoid leukemia [27]. In our research, the focus is on novel treatment options for AML, as well as a separate group of leukemia, MDS. MDS features similarities to AML and while previously thought of as an early phase of the latter, it was later re-classified as a separate type of myeloid malignancy [30].

1.2.2.1 Acute myeloid leukemia

AML is a cancer in the myeloid lineage of progenitor cells (Figure 3) leading to the typical symptoms of leukemia and an expected five-year survival of 30.5% [31]. In its 5th edition of 2022, the World Health Organization has further divided AML into two groups, AML with defining genetic abnormalities and AML types without defining genetic abnormalities. With genetic abnormalities playing a pivotal role for determining treatment strategies, the second group is expected to diminish with novel genetic discoveries [29].

For 2023, the American Cancer Society estimates around 20 380 new cases and 11 310 deaths from AML in the United States of America [32]. In Norway, the yearly average of new cases was 177 between 2016 and 2022, leading to a frequency of approximately three per 100 000 inhabitants per year [33]. While only accounting for around 1% of all cancer incidences, AML is one the most common types of leukemia in adults. AML mainly occurs in older people, with an average age at diagnosis of about 68 years [32].

AML can be suspected from routine blood tests or in patients exhibiting symptoms associated with leukemias such as fatigue, frequent infections, and bleeding [34]. Diagnosis of AML is based on morphological examination and immunophenotyping of bone marrow samples. Cytogenetic analysis can also detect AML-defining aberrancies and further determine the type of AML. Additional factors such as germline predisposition, therapy-relation or a history of myelodysplastic neoplasms are appended to the diagnosis, however with defining genetic abnormalities taking precedence [1].

1.2.2.2 Myelodysplastic neoplasms

MDS is a group of disorders of myeloid stem cells resulting in the production of differentiated, but defective myeloid blood cells. This disease can lead to symptoms similar to those seen in AML but can also be asymptomatic for years [35]. Between the years of 2012 to 2018, the five year survival rate was 36.9 % [31]. While the preceding factors of MDS are not entirely understood, over one hundred gene mutations common for MDS have been mapped. In some cases, MDS can progress to AML. This secondary AML is characterized by especially poor prognosis [35].

The number of yearly MDS diagnoses in the United States is not accurately known but estimated to be around 10,000. The disease is mostly diagnosed in patients in their seventies, and MDS before the age of 50 is uncommon [36]. In Norway, age of onset is similar, with a median age of diagnosis of 73. Yearly, approximately four to five new diagnoses are seen per 100 000 inhabitants according to the Norwegian Directorate of Health [37].

As with AML, determining the cytogenetics of MDS is of high importance to establish a prognosis and course of treatment. Number and type of genetic aberration, number of blast cells in the bone marrow and number and degree of cytopenias determine the risk of progression to AML and death [35].

1.3 Treatments for AML and MDS

For MDS patients, the only curative treatment is hematopoietic stem cell transplantation (HCT), a treatment for which older patients often are unsuitable for. However, in mild cases, treatment might not be necessary, with supportive measures such as blood transfusions or hematopoietic growth factors counteracting the symptoms of the disease [35]. While MDS has been proven to be resistant to cytotoxic chemotherapy, the use of hypomethylating agents and lenalidomide (Len) has shown promise [35]. Following three months of daily administration, Len has been shown to reduce the need for blood transfusions in some low and intermediate risk patients, especially in patients with a del 5q mutation [35, 38]. For high-risk patients, the hypomethylating agent azacytidine (Aza) was found to improve survival and has

shown the potential to delay the development of AML, however, following prolonged treatment, cytopenias often worsen and the disease progresses [35].

Following a diagnosis of AML, a standard treatment regimen is induction therapy. Induction therapy consists of treatment with high doses of cytarabine and an anthracycline, such as the drug daunorubicin (DNR), in cycles of seven days continuous cytarabine infusion with additional anthracycline infusions the first three days [39]. In patients with an FMS-like tyrosine kinase 3 (FLT3) mutation, midostaurin, a kinase inhibitor which also targets FLT3, has also become a standard addition in this regimen [1]. If remission is achieved, consolidation treatment with intermediate-dose cytarabine aims to destroy any remaining AML cells. While no generally accepted definition of maintenance therapy exists, the objective of the maintenance phase following consolidation treatment is to reduce the risk of relapse with minimally toxic therapies, where Aza has shown promise [1, 39]. For frail patients unable to undergo intensive chemotherapy, regimens with lower doses, treatment with Aza, the BCL2 inhibitor venetoclax, or the IDH1 inhibitor ivosidenib remain options to increase the overall survival depending on the underlying cytogenetics [1].

For MDS patients, or if AML stops responding to chemotherapy, the only curative treatment is HCT [1, 35]. Here, the immune cells and bone marrow, including the hematopoietic stem cells of patients, are first destroyed, followed by replacement from a healthy donor. This treatment, while improving, is still associated with high mortality and long-term health issues through infections or graft vs host disease. Thus, the risk of HCT itself has to be evaluated against the risk of the disease [1, 40, 41].

The combination of poor prognoses, harsh treatments, and heterogenicity of the diseases, fuel the need for new drugs. For this, a wide range of novel treatments are under investigation, such as FLX925, a dual FLT3 and CDK4/6 inhibitor for AML treatment, and a liposomal formulation of cytarabine and DNR, CXP-351, for the treatment of high risk MDS [42, 43]. A novel target for treatment against AML is the GTPase Ras-related C3 botulinum toxin substrate 1 (Rac1) [44].

This GTPase, commonly overexpressed in AML, is part of the hematopoietic cell homing to the bone marrow niche situated downstream of the SDF-1 receptor

CXCR4 [45, 46]. With first-generation inhibitors of Rac1 already haven shown promise, we will focus on the second-generation inhibitor EHop-016 in this work [46]. In previous studies, this compound has shown promise as a treatment against breast and lung cancer [47, 48], and under investigation as an potential anti-malarial agent [49].

1.3.1.1 The role of nano-sized drug delivery systems in cancer therapy

Some drugs, while promising *in vitro* can present a number of challenges when applied *in vivo,* such as poor solubility, short circulation times or adverse off-target effects. A solution to these problems can be the use of nano-sized drug delivery systems (NDDSs) to complement the treatment. NDDSs are nanoparticles which aim to transport drugs until their release results in optimal effects. Among the many potential uses, NDDSs can aid through focusing cytotoxic drugs on diseased tissues, act as reservoirs and slowly release drugs to extend time in the therapeutic window or co-deliver multiple compounds for simultaneous release in the desired locations [50].

Figure 4 illustrates three different categories of NDDSs. Liposomes are small spheres consisting of a lipid bilayer, as illustrated in Figure 4A. Here, a hydrophilic core and hydrophobic shell enables the transport of drugs with either solubility [50]. Treatments using this NDDS are already in use, such as VYXEOS®, a liposomal formulation combining the drugs DNR and cytarabine for AML treatment, and both Pfizer/BioNTech and Moderna mRNA COVID-19 vaccines [51, 52]. Compared to liposomes, polymeric NDDSs allow for the gradual release of a drug (Figure 4B). These NDDSs consist of entangled and cross-linked polymers, which entrap drug molecules in cavities formed between strands [53]. The last illustrated NDDS, graphene (Figure 4C), was investigated using our zebrafish model in Paper III. This NDDS is further described below in 1.3.1.1.1.

A major feature of NDDSs is also their high customizability without changing the transported drug. By changing their size, charge or shape, factors like place of accumulation or way of clearance can be modified [54]. In cancer treatment, an effect termed enhanced permeability and retention effect could lead to the accumulation of NDDSs of the right size near tumors through leaky blood vessels [55]. For clearance, size can also play a crucial role. In particles between 10 to 20 nm, clearance happens

rapidly through the kidney, while larger particles are prone to activation of the complement system and resulting phagocytosis by macrophages [54]. Additional customization of NDDSs can be achieved through functionalization. In functionalization, active ligands are attached to the NDDS. If antibodies are connected to NDDSs, these can retain the particles once the desired tissue is encountered, a technique called active targeting [56]. Another modification of NDDSs is the incorporation of polymers such as polyethylene glycol, a polymer that increases NDDS solubility, decrease particle agglomeration, and have been shown to aid in immune system avoidance [57].

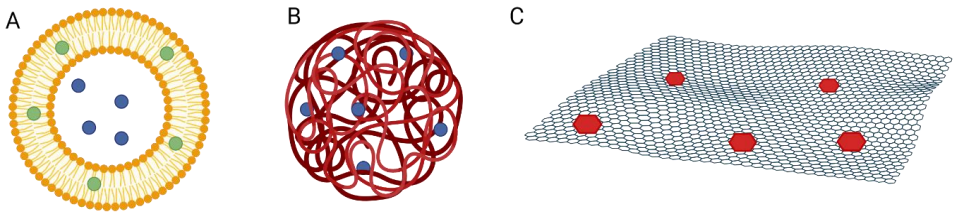

Figure 4: Overview of nano-sized drug delivery systems (NDDSs). NDDSs can improve treatments by controlling the drug release rate and location, protecting drugs from metabolism or clearance, or by transporting otherwise insoluble molecules. Three examples of NDDSs are given. Liposomes in A, with hydrophobic drugs (green) and hydrophilic drugs (blue) in the membrane and core respectively, polymeric nanoparticles in B with a drug (blue) entrapped in the entangled polymer, and graphene in C, with aromatic drugs bonded to the graphene sheet through pi-stacking. The figure was created using BioRender.com.

1.3.1.1.1 Graphene

Graphene is a nanomaterial consisting of a single sheet of carbon atoms (Figure 4C). The bulk form of graphene is graphite, where individual sheets of graphene are stacked on top of each other [58]. While this single atom thick carbon material was previously thought not to exist in a free state, Geim, Novoselov, *et al*. demonstrated the production of graphene by rubbing graphite on a solid surface in 2005, winning a Nobel prize in 2010 [58-60]. In the biomedical field, graphene and its derivates have a range of applications, with examples being their use as biosensors, scaffolds for cell

cultures, and as fluorophores in bioimaging [61]. These materials also show great potential for their use as an NDDS, with reactive groups found on edges and defect sites facilitating functionalization, innate pH dependent drug release and ability to reversibly bind aromatic drugs through pi-stacking [61].

2 Aims

With myeloid malignancies being genetically diverse and usually with poor prognosis and harsh treatment regimens, a wide range of effective treatments is required. To facilitate this research, we aim to further develop and evaluate the zebrafish larvae as a relevant *in vivo* model to test emerging therapies for these diseases.

This overarching goal was further subdivided into three secondary aims, represented by the three presented papers.

- **Improve the quality of data analyses from cell studies in zebrafish larvae.** To gather necessary data for further studies, a large number of confocal measurements of cells in zebrafish larvae is required. Due to the large file size and complex nature of 3D image stacks, analysis is time consuming and cumbersome. The objective of this work was therefore to develop an effective tool to study fluorescent objects like cancer cells in the zebrafish larvae. (Paper I)
- **Validate the analytic tool developed in Paper I for drug efficacy tests in zebrafish larvae.** The zebrafish larva model needs to be evaluated as a screening organism for drug development for myeloid malignancies. Using the software developed in Paper I, we wanted to find if the *in vitro* effect of the novel drug EHop-016 was also present *in vivo* in zebrafish larvae transplanted with fluorescently labelled AML cells. (Paper II)
- **Document the behavior of new potential nanocarriers for cancer drugs *in vivo***. NDDSs are especially dependent on a model organism to determine their effectiveness. Using zebrafish larvae as a model system we will investigate toxic effects of graphene, an emerging NDDS. With macrophages being a major mechanism for clearance of NDDSs, zebrafish with fluorescent macrophages were used to investigate the interactions between larva and NDDS. (Paper III)

3 Methodological considerations

3.1 Cancer cell lines

To investigate treatments for cancer, a model system of this disease is required. In this work, we used cell lines, which are cells initially isolated from patients, but immortalized and cultured over an extended time. These cell lines are extensively used in research across laboratories. This results in a well-characterized model system with standardized methods for culturing, handling, and data analysis. Compared to primary cell cultures, cells isolated from donors and used without long time culturing and distribution, cell lines are easier to maintain and yield more reproducible results, however this at the cost of a more homogenic model being used to investigate a diverse disease such as cancer [62]. Care must also be taken during culturing, as accidental contamination with different cell lines and genetic drift over long periods of culturing can invalidate the model. Cross-contamination with different cell lines in particular has been a major issue in biomedical research [63]. We tried to minimize the risk of both issues through periodically replacing our actively used cell cultures with frozen cell-backups created close to the procurement of the cell lines from commercial suppliers.

3.1.1 MOLM-13

The MOLM-13 cell line was established in 1995 and published in 1997 by Matuso *et al*. [64]. This cell line originates from a 20-year-old male AML patient, who initially was diagnosed with MDS, but later relapsed and developed AML. For our research, a key mutation is the FLT3 internal tandem duplication (FLT3-ITD) found in MOLM-13 [65]. This mutation has been shown to lead to an over-activation of Rac1, the target of the drug EHop-016 in Paper II [66].

MOLM-13 cells have been extensively used for the study of FLT3 inhibitors and as a basis for cell line derived cancer models in mice, which further increases the relevance of these cells [67]. However, no single AML cell line can completely emulate the complexity of this disease. While a myriad of AML cell lines exist, to complete our work on the zebrafish larva model during this project, we settled on the use of MOLM-13 only for AML [67]. Nevertheless, the use of multiple AML cell lines would

have improved our study. A cell line which could have aided in our evaluation of EHop-016 is MV4-11, a line which also features an FLT3-ITD mutation and has also been used in previous zebrafish studies [65, 68].

3.1.2 MDS-L

The MDS-L cell line first originated from a separate cell line for MDS, MDS92. This cell line, published in 1994, was obtained from a 52-year-old male patient [69]. Instead of being a homogenic culture, this cell line is comprised of blastic and myeloid cells at different stages of differentiation. From this cell line, the MDS-L cell line was generated [70]. Notably, this cell line is dependent on addition of IL-3 in the medium for optimal proliferation. Zebrafish are likely missing an orthologue of this cytokine, while in zebrafish the function is most likely compensated for by other factors, the use of a different MDS cell line would have been optimal [71]. For the purpose of validating the presented software in Paper I, this cell line was however suitable.

3.1.3 HUVECs and SW948

Human umbilical vein endothelial cells (HUVECs) and the cell line SW948 were used for initial toxicity cell studies of graphene in Paper III, due to their use in studies of similar materials [72]. These cells are not of myeloid malignancies, with the first being an umbrella term of primary cultures from a type of human endothelial cells commonly used in research and the latter being a colorectal cancer cell line [73, 74].

3.2 *In vitro* assays

Prior to utilizing *in vivo* assays using zebrafish larvae in Paper II and III, we utilized *in vitro* assays. These assays provided an initial insight into our research questions and aided in planning *in vivo* experiments, reducing the total number of zebrafish larva studies needed.

To determine the cytotoxicity of drugs or NDDSs under investigation, viability assays were needed. Viability of cells can be measured in a number of different approaches, in this work, we used enzyme-linked (Figure 7A), DNA-synthesis-linked (Figure 7B), and membrane-linked (Figure 7C) methods. Each of these assays has its own benefits and drawbacks, which are more closely discussed in the following three sub-chapters. In general, these assays aim to measure different cellular processes which can all be

interpreted as cell “viability”. The choice of the most suitable assay is dependent on the research question, but also on practical aspects such as number of samples considering the assay cost of both time and money, and available infrastructure and expertise.

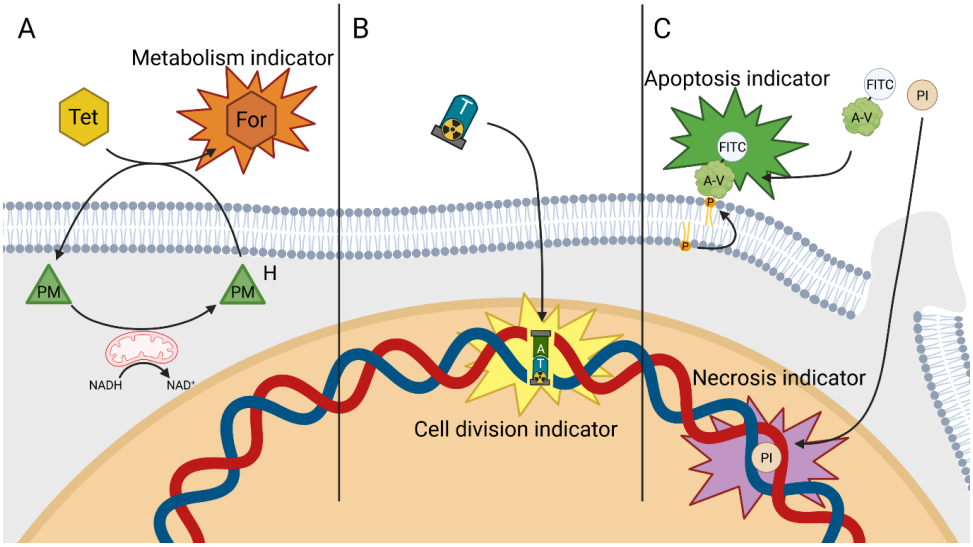

Figure 7: *In vitro* viability assays. In A, the enzyme-activity linked water soluble tetrazolium salt 8 (WST-8) assay is illustrated [75]. In metabolically active cells, dehydrogenases in the mitochondria reduce 1-methoxy phenazinium methylsulfate (PM) through the conversion of NAD(P)H to $NAD(P)^+$. PM, in turn, reduces the supplied tetrazolium salt (Tet) to formazan (For). Using the difference in color between Tet and For, the conversion from one dye to the other can be measured through spectrometry. In B, an essay to measure DNA synthesis, the ^{3}H-thymidine assay is shown [76]. Here, the nucleoside thymidine (T) is radioactively labeled using tritium and supplied to cells. When the cells divide, this is incorporated into their DNA. By measuring the radioactive decay of the incorporated ^{3}H-thymedine, the extent of cell proliferation can be determined. The annexin-V (A-V) and propidium iodide (PI) assay, shown in C, indicates apoptotic or necrotic cells through probing of the cell membrane [77]. In apoptotic cells, a phospholipid, phosphatidylserine (P, orange), that in viable cells is found on the cytosolic side of the cell membrane is flipped to the extracellular side. Here, fluorescently labeled A-V, for instance using fluorescein isothiocyanate (FITC), binds to P. In necrotic cells, when the cell membrane has been compromised, the fluorophore PI can enter the nucleus and bind to DNA. By analyzing whether a cell has been stained by either fluorescent marker, it can be determined if a cell is viable (here, negative for both FITC and PI), apoptotic (here, positive only in FITC), or necrotic (Here, positive for both FITC and PI). The figure was created using BioRender.com

3.2.1 CCK-8 viability assay

The CCK-8 assay performed in Paper III is one of many variants where a water-soluble tetrazolium salt is used to monitor the metabolic activity of a cell population (Figure 5A). In metabolically active cells, this dye is enzymatically converted to a formazan dye through cellular dehydrogenase activity. The resulting formazan dye has a different absorption spectrum compared to tetrazolium salt, enabling the quantification of conversion through absorption spectroscopy. These results can indicate the number of cells within the sample when compared to a control [75]. When using this assay, care must be taken, as the rate of conversion from tetrazolium to formazan can be impacted by cell count, but also metabolic rate of these cells. Additionally, the conversion can be facilitated independently of cell metabolic rate, such as through the drug under investigation or presence of reactive oxygen species.

3.2.2 ^{3}H-thymidine assay

In the ^{3}H-thymidine assay, cell divisions are measured (Figure 5B). This is performed by supplying the cells with an analog of the DNR nucleotide thymidine, which has been rendered radioactive by the incorporation of tritium. When cells divide, this radiolabeled thymidine is incorporated in the cell's DNA. By measuring the radioactivity of the cells following the conclusion of the experiment, the extent of cell proliferation can be measured and compared to a control [76]. While the radioactive nature of this assay has been shown to impact cell division by itself, this effect becomes mainly pronounced following exposure longer than the six-hour incubation periods performed in Paper II [78].

3.2.3 Flow cytometry

Flow cytometry is a high-throughput analysis method used to measure light scattering and fluorescent emissions of single cells. Here, the sample containing cells is fed into a flow cytometer, which passes a single file stream of cells in front of a laser source. The cells scatter the laser in-line with the laser source and at an angle to it, termed forward scatter and side scatter respectively. This scattering is measured by detectors and gives insight into cell size and the complexity of the cytoplasm, i.e. granularity. If fluorophores are present, these fluorophores are excited and emit photons which are detected through a series of filters and detectors. In combination with fluorescent

probes, this is a powerful method for characterizing thousands of cells from one population within a short period of time [79].

In Paper II, we utilized flow cytometry in combination with a staining kit containing propidium iodide (PI), and annexin V coupled to fluorescein isothiocyanate (FITC), to detect apoptotic and necrotic cells following treatments with EHop-016, DNR and combinations thereof. This staining kit marks necrotic cells with PI, a fluorophore which is unable to stain cells with intact cell membranes (Figure 5C). If the cell undergoes necrosis, the cell membrane is compromised, and PI stains the cellular DNA. Annexin V is a protein with the ability to bind to phosphatidylserine (P). P is normally found on the cytosolic face of the plasma membrane. As the cells undergo apoptosis, this phospholipid is transferred to the extracellular side, thereby making it available for binding by annexin V [77]. Using this staining kit, viable cells will be negative for both PI and annexin V-FITC, apoptotic cells only positive for annexin V-FITC, and necrotic cells positive for both fluorescent probes.

In Paper II, we used this staining kit to analyze cells treated with DNR. DNR is problematic when working with fluorescent probes, since DNR itself exhibits fluorescence with a spectrum overlapping with PI. Consequently, cells treated with DNR exhibit a higher background fluorescence in the channel used for PI measurement when compared to cells with lower DNR concentration. This can be addressed by computationally compensating for the increased fluorescence, as was performed in Paper II. However, this method can impact accuracy of the results. A better solution for this issue would have been to utilize a different fluorophore with less fluorescence overlap with DNR.

3.2.4 Synergy analysis

Synergy is the effect of increased efficacy of a treatment consisting of multiple drugs compared to the combined efficacy of each drug by itself. To quantize synergy, a synergy score can be calculated by subtracting a theoretical efficacy of a drug combination from the experimentally determined efficacy of this treatment as shown in Equation 1.

$$\text{Eq1:} \qquad Synergy\ score = E_E - E_T$$

Where E_E is the experimentally determined efficacy of a drug combination in percent and E_T is the theoretical effect of the combination in percent. If this subtraction yields a positive synergy score, the combination behaves synergistically, while a negative score indicates antagonism. Different approaches exist to determine the theoretical score of the drug combination. In Paper II, we chose the Bliss synergy score as a theoretical model to investigate the combination of EHop-016 and DNR [80]. This method is a probabilistic approach, suited for a combination of drugs with different modes of action, where efficacy is the ability of a drug to inhibit a given metric, such as cancer cell proliferation. To calculate the theoretical Bliss efficacy for a combination of two drugs, Equation 2 can be used.

$$\text{Eq2:} \quad E_{Bliss} = 100 * (1 - \left(1 - \frac{E_A}{100}\right) * \left(1 - \frac{E_B}{100}\right))$$

Where E_{Bliss} is the theoretical Bliss efficacy of the combination in percent, and E_A and E_B the efficacy of drug A and B in percent respectively. Here, the concentrations of drug A and B are the same as being used in the combination. Note that this equation works by calculating the probability that a cell is not affected by drug A or B, followed by an inversion to find the estimated efficacy of the combination.

3.2.5 Transwell migration assay

A transwell migration assay was used in Paper II to investigate the impact of EHop-016 on the migration of MOLM-13 cells. Here, cells treated with EHop-016 were placed in the upper compartment of a two-compartment setup, separated with a porous membrane. In the lower compartment, an attractant, either fetal bovine serum (FBS) or SDF-1, is used to incentivize migration of the cells. Following an incubation period, cells in the lower compartment are measured to determine migration rate.

This method allows for a quick and repeatable assay to get an initial indication for the efficacy of drugs impacting migration. A drawback of this method is, however, its simplicity. The system does not reflect the complex microenvironment found *in vivo*, requiring additional experiments to confirm results. Another drawback is the possibility of passive migration to the bottom well through gravity. External

disturbances while conducting the assay can hence lead to a difference in measured migration, impacting the reliability of the results.

3.2.6 Complement activation assay

In Paper III, the rate of complement system activation was measured for graphene samples of different production methods. Here, blood from healthy volunteers was incubated with graphene samples and the reaction stopped using EDTA. Indicators of complement system activation, C3b and C3c (in our assays combined to C3bc), and the terminal complement complex were measured using an enzyme linked immunosorbent assay as described by Bergseth *et al*. in [81]. This assay was approved by the regional committee for medical and health research ethics (REK SØR S-04114)

This assay yielded good initial insights into the immunoreactivity of our graphene samples. However, the covalent marking of the graphene sheets for phagocytosis, opsonization, could not be measured using this method. Thus, in Paper III, these results were complemented by studies using zebrafish with fluorescent macrophages.

3.3 Zebrafish methods

Two types of zebrafish larva studies were performed in this project. Toxicity studies, where adverse effects of a drug were evaluated, and efficacy studies, where the effect of a treatment was evaluated on transplanted human cancer cells. For all zebrafish experiments, we used the transparent casper zebrafish line [17]. This line was originally created through the crossing of two mutants, the nacre zebrafish, lacking melanocytes, and the roy orbison zebrafish, lacking iridophores. The result of this crossing was the casper zebrafish line, lacking both iridophores and melanocytes, which proved ideal for the tracking of fluorescent cells *in vivo* [17]. For Paper III, we genetically modified this casper line to express fluorescent macrophages, as further described in 3.3.3.3.

The characterization of fluorescent cells in the zebrafish larvae was performed using confocal microscopy and played a key role for both types of studies. To process the large amount of data acquired, a software tool was developed to perform the analyses in a semi-independent manner. While by convention, zebrafish up to three dpf are

termed “embryo”, and “larva” following the start of four dpf, for simplicity, the term “larva” is used for both zebrafish embryos and larvae in this work [11]. Treatments were either administered through intravenous (IV) injections into the posterior cardinal vein (PCV, Figure 6F) or simply added into the water surrounding the larvae. For small molecules with good solubility, such as EHop-016, this method is popular for drug testing in this animal model [82]. While this administration route differs from typical administration routes in mammals, in our case, this was preferred to reduce the stress of repeated injection on the larvae, as well as to ensure constant exposure to the drug. The site of injection, as well as other important structures in the zebrafish larva are shown in Figure 6. In this section, the zebrafish larva-based methods employed in our work are described. A critical evaluation of zebrafish larvae as model organisms for myeloid malignancies is given in the Discussion section 5.4.

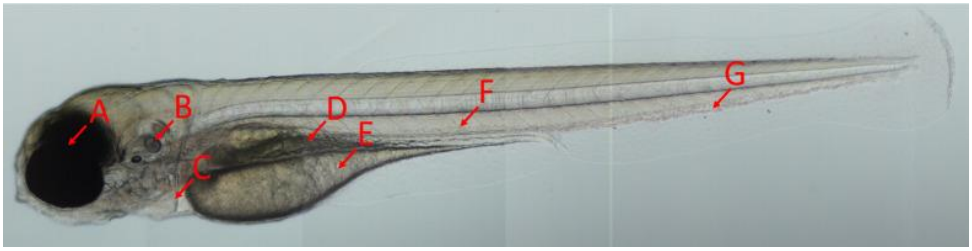

Figure 6: Overview of the zebrafish larva. Here, a casper zebrafish larva at four days post fertilization is shown. Arrows show the locations of the eye (A), otolith (B), heart (C), gut (D), yolk sac (E), the posterior cardinal vein used for intravenous injections (F), and the caudal vein / caudal hematopoietic tissue (G). This figure is from Paper I.

3.3.1 Zebrafish handling

All mature zebrafish were kept at the zebrafish facility at the Department of Bioscience, University of Bergen, and held in accordance with the European Convention for the Protection of Vertebrate Animals used for Experimental and Other Scientific Purposes [83]. Following fertilization, zebrafish eggs and larvae were incubated at 28.5 °C. For experiments including transplantation of human cancer cells, the incubation temperature was raised to 31 °C following transplantation.

3.3.2 Confocal microscopy

Confocal microscopy is an optical microscopy technique where photons originating from areas outside the focal plane are excluded prior to reaching the detector. Combined with fluorescence microscopy, this allows for the creation of optical slices of a sample without the need to prepare sections using a microtome. When multiple optical slices are taken at varying focal planes, the resulting images can be combined to result in a three-dimensional (3D) image [84].

This method played a key role in zebrafish larva experiments performed in all three presented papers, as it allowed the 3D-imaging of fluorescent cells within living larva. A drawback of this technique is the generation of large file sizes and cumbersome image processing required to extract the information on cell position, count, and sizes. We addressed this issue by developing a software tool which is presented in Paper I.

3.3.2.1 Computer assisted image processing

Many of the experiments in this work require the counting and measurement of fluorescent cells in confocal images of zebrafish larvae. To improve the data acquisition from these large data sets, we developed a software tool. This tool is described in detail in Paper I. Summarized, the software utilizes a watershed algorithm to segment cells that are located within the larva [85]. This algorithm can be explained by thinking of the intensity levels of pixels as a separate dimension. If a single row of pixels is considered, this results in a graph as shown in Figure 7. To aid in the intuitive understanding of this algorithm, the intensity level has been flipped, resulting in higher intensity values to be represented lower on the y-axis. The first step is to detect local maxima in the image, and this is done by simply evaluating whether each pixel has the highest intensity value compared to other pixels within a predetermined distance. The watershed algorithm starts from these local maxima, and "fills up" or claims adjacent pixels of gradually lower intensities. If this process results in a merger of two neighboring segmented regions, a border is created between them instead, thereby holding each region separate. The process continues with ever decreasing intensities being included in the segmented regions, or in this example as if the water level was rising, until a predetermined threshold is reached. In

our work, this threshold is the background fluorescence found in the confocal images. The software performs this segmentation process for each acquired image and collects the desired information of each detected cell. Additionally, images from the same larva across different acquisitions are tracked. The output is a dataset of each object found within the images, the position in three dimensions, size, and intensity of this object, as well as in which larva and acquisition the object was detected in.

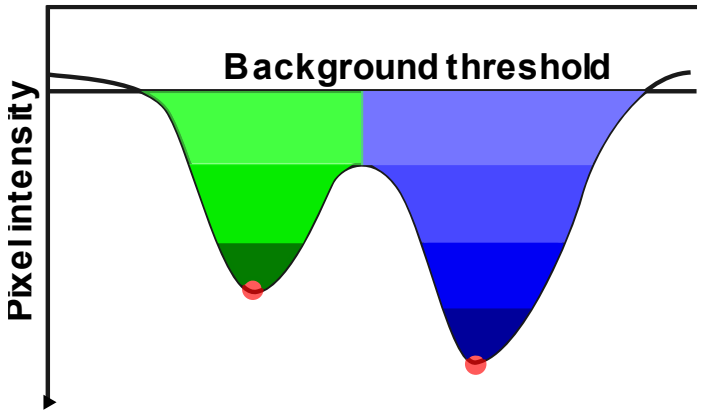

Figure 7: Watershed segmentation algorithm. To illustrate the principle of the watershed algorithm, a one-dimensional slice of an image is shown, with pixel intensities increasing in the downwards direction. Segmentation starts by finding local maxima (red dots). From each local maximum, neighboring pixels of ever decreasing pixel intensity are included as shown by the red and green gradients for each of the two maxima. The segmented areas of two different maxima are not allowed to overlap, resulting in a boundary as seen in the figure. The intensity of included pixels is decreased until the background threshold is reached. The same principle is extended to three dimensions for confocal images.

3.3.3 Toxicity studies

3.3.3.1 LD_{50} and visual abnormalities

To determine the maximum tolerable dose (MTD) we performed LD_{50} studies and observations of visual abnormalities following drug administration. For these studies, administration was always performed from two dpf until reaching five dpf. While most visual abnormalities were easy to present through microscope images, to visualize the blood flow obstructions found in Paper II a different approach was needed. We chose to film sedated larvae and create a still image from the standard deviations of each pixel across each time frame. With the sedated larva at rest in the

clip, blood flow was the only major source of change in pixel intensity, and thereby standard deviation. This image was used as an overlay on a still frame of the original clip, thereby highlighting areas with blood flow and visualizing any obstructions when compared to a control.

3.3.3.2 Measurement of zebrafish heartrate

To measure the heart rate in Paper I, we presented a method based on the fast Fourier transform (FFT) [86]. This was done to improve accuracy and save time in large scale experiments. For this assay, the heart of a larva was filmed for approximately 10 seconds. The resulting clip was processed in the image processing software FIJI [87]. Here, the intensity values of pixels around the heart were averaged for each frame and recorded. The beat of the heart induced fluctuations in these averages with the same frequency as the heartbeat. By performing an FFT on the fluctuating average intensities, the frequency of these fluctuations could be determined. To improve processing speed, this method was implemented in a macro, to batch process all filmed larvae and automatically choosing the point of highest fluctuation in pixel intensities as the heart.

3.3.3.3 Assessment of macrophage-nanoparticle interactions

In paper III, we investigated interactions between macrophages and graphene particles. With agglomerates of the highly absorbent graphene being readily visible, we needed a way to observe macrophages *in vivo*. To facilitate this, we created a transgenic zebrafish line based on the casper line and a commercially available plasmid [17] (Addgene plasmid #58935; http://n2t.net/addgene:58935; RRID:Addgene_58935). This plasmid contains the red-fluorescent protein mCherry downstream of the promotor mpeg1 and was incorporated into the DNA of zebrafish zygotes using the Tol2 transposase system [88] following the protocol outlined in [12]. The mpeg1 promoter is active in zebrafish macrophages and thereby leads to mCherry transcription and translation in these cells [89].

We exposed zebrafish larvae of this line to graphene using IV injections, and tracked the count and distribution of the fluorescent macrophages over the following days using confocal microscopy and the software tool developed in Paper I.

3.3.4 Studies on transplanted cells

3.3.4.1 Treatment efficacy

Treatments of transplanted cancer cells in zebrafish larvae were investigated using the cell lines MDS-L (Paper I) and MOLM-13 (Paper I and II). Transplantation was performed by IV injection into the PCV using micropipettes with a 13 µM inner diameter allowing for the passage of cells. Treatments were administered through either separate IV injections or in-water.

To track the transplanted cancer cells over the course of the experiment, we utilized cell staining with a far-red fluorescent dye, followed by daily confocal imaging of the larvae. Using the software tool presented in Paper I, the cancer cells were segmented from the images, and the resulting data used to evaluate treatment response.

3.3.4.2 Timelapse migration studies

In Paper II, we investigated the effect of eHop-016 on MOLM-13 cell migration to the CHT following IV injection. This was done by pre-treating both larvae and cells with EHop-016 followed by a timelapse immediately after cancer cell transplantation. The accumulation of cells in the larval tail area containing the CHT was studied and compared to an untreated control. Due to technical limitations of the software tool presented in Paper I, and the file type exported by the microscope software, the counting of cells was performed manually for these experiments and hence relied on projections of the 3D image-stack.

3.4 Graphene production and characterization

3.4.1 Production

3.4.1.1 Sonication

Sonication provides a simple method to produce graphene particles [90]. This method was used as one of the production methods investigated in Paper III. Here, commercially available graphite flakes were first dissolved in carboxymethylcellulose salt (CMC) which acted as a stabilizer, followed by sonication to disperse the graphene sheets. To separate un-exfoliated graphite from graphene, the samples were centrifuged following sonication, and the sediments discarded[91].

3.4.1.2 Microfluidization

A method for producing graphene particles via microfluidization was presented by Panagiotis *et al*. in [91]. The production method starts the same as for sonication with the dissolving of graphite flakes in CMC, or the alternate stabilizer sodium deoxycholate (SDC). To exfoliate the graphene sheets, the mixture is further processed in a microfluidizer. A microfluidizer uses a high-pressure pump to force the graphene suspension through an interaction chamber with microchannels, where high shear forces exfoliate the graphite particles to graphene sheets. The process can be repeated for a desired number of cycles until all the graphite has been exfoliated.

3.4.2 Graphene characterization

In Paper III, atomic force microscopy (AFM) and scanning electron microscopy (SEM) were used to characterize particle dimensions, while Raman spectroscopy was used to confirm that the production yielded graphene and not graphite nanoparticles.

AFM is a microscopy technique relying on a few-atom-wide tip instead of light or electrons as a probe for imaging. This tip is mounted on the end of a cantilever, the deflection of which is measured by reflecting a laser of its surface and onto a detector. When the probe is moved across the sample in close proximity, interatomic forces attenuate the deflection of the cantilever. Using this information, the instrument constructs a 3D height map [92]. In AFM, a number of artifacts can occur due to tip geometry and brakes, incorrect measurement settings or samples getting attached to the tip. These artifacts are however readily detectable under careful operation.

The resulting size measurements were confirmed using SEM. In SEM, electrons are used to illuminate the sample in a scanning pattern. For each point of the sample illuminated, a range of resulting electrons and x-rays can be measured through detectors positioned at an angle compared to the incident electron beam. This results in a perceived shading of the sample, with surfaces pointed towards the detector seeming “brighter” and surfaces tilted away “darker” [93].

A drawback of these techniques compared to alternatives such as dynamic light scattering (DLS) is that comparatively few samples are measured. This can impact

the accuracy when determining the size distribution of a graphene sample. Due to the geometry of the graphene sheets, DLS and similar methods are however not usable, leaving AFM and SEM as the method of choice in this work [94].

To measure the quality of our graphene samples, we used Raman spectroscopy. Here, Raman scattering is measured to obtain information about the molecular bonds in a sample. Raman scattering is different from Rayleigh scattering in that the scattered photon has a different energy compared to the incoming photon. The change in photon energy is due to interactions with the molecular vibrations, where the photon energy is either decreased or increased by inducing or absorbing energy from molecular bond vibrations. Due to the different vibrational modes possible and prominent in graphene vs graphite, this method can be used to determine the quality of graphene [95].

4 Summary of results

4.1 Paper I

Paper I, concerns the method development to facilitate data processing from confocal images of zebrafish larvae containing fluorescent objects like transplanted or endogenous cells. In this work, we developed a software tool for the open-source image software ImageJ [96]. The tool was designed to semi-automatically handle large sets of confocal images of fluorescent cells in zebrafish larvae and using a segmentation algorithm isolate and measure individual cells. Measurements performed by this software are cell positions within the image, cell volumes, total cell count, and fluorescent intensities of the cells in all captured channels. While some user input is still required, the software tool improved data analysis from confocal images by reducing the need for manual work, reducing sources of bias during image evaluation, and crucially, by providing a wide range of single-cell measurements, a feat not feasible using a manual approach or other software tools. A more detailed description of the method of operation of this software tool is given in the Method section in 3.3.2.1.

As part of the software validation, zebrafish larvae were transplanted with the human cell lines MOLM-13 and MDS-L, which had been fluorescently labelled. Further, the larvae were subjected to treatment using the drugs DNR or Aza. Using the software tool, we found an initial decrease in the cancer cell population shortly following cell transplantation in both treated and untreated groups before leveling off over the course of the experiment. For the MDS cell line MDS-L, no significant differences between the Aza treated and untreated larvae were found, likely due to the slower acting method of the drug as well as drug resistance of the MDS-L cells. In larvae transplanted with MOLM-13, however, we found a significant decrease of the cancer cell population in larvae treated with DNR when compared to the control. Interestingly, using the cell location information extracted by our software tool, we found indications of a protective effect against DNR for MOLM-13 cells situated in the CHT. This was one of the observations inspiring the experiments involving the drug candidate EHop-016 in Paper II.

In addition to the software tool for image processing of confocal files, we also presented a simple algorithm for measurement of larva heartrate from short video sequences to replace manual counting. This method is presented in 3.3.3.2. The software was used to detect a transient reduction in heartrate following injection of DNR, lasting over a day until recovering to the same level as the control two days after drug injection.

Correction for Paper I:

There is an error in the link providing access to the compiled version of the presented software in the publication. The software can instead be accessed through: doi.org/10.5281/zenodo.7383160.

4.2 Paper II

In Paper II we investigated the use of the Rac1 inhibitor EHop-016 as a treatment against AML. Rac1, a GTPase commonly overexpressed in AML, is involved in the homing of hematopoietic cells to the hematopoietic niche and has been identified as a possible target for AML therapy [45, 46]. In addition to evaluating the effects of EHop-016 on AML-cells, we also investigated a potential synergy with DNR, due to our findings of a potentially shielding effect of the CHT on cancer cells in DNR treated larvae (Paper I).

EHop-016 demonstrated an antiproliferative effect with EC_{50} of 6.1 µM using the ^{3}H-thymidine proliferation assay. Further investigation was conducted using flowcytometry and the annexin V/PI assay, where we found a synergistic effect between EHop-016 and DNR of up to 21% according to the Bliss method for calculating drug interactions. EHop-016 caused a significant reduction of MOLM-13 migration over a porous membrane in an *in vitro* transwell migration assay.

Toxicological studies in zebrafish revealed that the LD_{50} of in-water administrated EHop-016 was between 25 and 50 µM. Furthermore, at 50 µM, toxic effects on the circulatory system were found, with cardiac arrest and obstructions in the caudal artery and caudal vein around the CHT being observed. Considering these toxicologic

results, treatments with 20 μM EHop-016 were used in further studies to allow for additional stress in larvae receiving a combined treatment with DNR.

In zebrafish larvae, EHop-016 reduced the migration of MOLM-13 cells to the CHT over a 12-hour period after cell injection, compared to untreated larvae. The effects on MOLM-13 cells following a day of treatment were also promising. Both EHop-016 and DNR lead to a stagnation in MOLM-13 proliferation, and a significantly lower cancer burden when compared to the control. When measuring the total volume of all cancer cells in the zebrafish larvae, the combination treatment led to a significantly lower total volume compared to the control and either treatment alone.

4.3 Paper III

In this paper, we investigated whether graphene production method affected toxicity and *in vivo* clearance, again using zebrafish larvae as a model system. We compared two approaches of graphene production, sonication and microfluidization. Tests on cell lines showed that sonicated graphene had higher cytotoxicity compared to microfluidized graphene, which was evident when adjusting for concentration or for sheet size. *In vitro* assays of complement system activation also demonstrated an increased immunoreactivity of sonicated graphene. Here, in samples containing sonicated graphene, a ten times higher concentration of complement system activation markers were found when compared to microfluidized material.

All graphene samples were found to have low toxicity in zebrafish larvae after intravenous injections. There were visible accumulations of graphene especially in the CHT area. To investigate the impact of the previously found complement system activation in zebrafish larvae, we utilized transgenic zebrafish larvae with macrophages expressing the fluorescent protein mCherry. We found a decrease in macrophage count in larvae exposed to microfluidized graphene one day following exposures. This, however, returned to levels comparable to the control the following day. Sonicated graphene did not impact the macrophage count until two days following exposure. Here, a significant increased number of macrophages were detected.

Further analyses investigated the distribution of macrophages within the larvae over the course of the experiment. All graphene samples changed macrophage distribution one day post injection compared to control. The following day, the distribution returned to that of the control group. For sonicated graphene, this deviation was an increased macrophage presence in the CHT area compared to the rest of the larvae. Microfluidized graphene led to the opposite effect. Here, macrophage concentration in the CHT area was lower compared to the control, while the PCV and heart area showed an increased presence of macrophages.

5 General discussion

In our work, we aimed to further develop and validate the zebrafish model for the treatment development of myeloid malignancies. This overarching aim was subdivided into three secondary aims, the improvement of data analysis in zebrafish studies, validation of this approach in drug efficacy studies, and the investigation of an NDDS using this model. These aims were achieved through the development of a software aid for image processing, evaluation of the drug EHop-016 for AML treatment, and comparison of two production methods for the NDDS graphene *in vivo*. We will first address each of these points individually, followed by an overarching discussion on the use of zebrafish larvae in the treatment development against myeloid malignancies.

5.1 Software aided image processing

Much of the work presented in this thesis required the extensive use of confocal imaging to track and quantify fluorescent cells within zebrafish larvae. As pointed out by Mikut *et al*., processing of such large datasets quickly becomes a bottleneck in the research process [97]. To overcome this hurdle, we aimed to develop a software tool, improving the data analysis in the following studies. The software tool, presented in Paper I, proved to be useful for the quantification of fluorescent cells in zebrafish larvae, demonstrated in Paper II where we investigated transplanted human AML cells, and in Paper III where the zebrafish larvae's own macrophages were subject to analysis. With its capability of segmenting and measuring thousands of individual cells across multiple larvae and acquisition times in a single experiment, it allowed for a detailed analysis of the cell populations not otherwise feasible. Software for the analysis of fluorescent signals in zebrafish larvae has been presented before [98, 99]. However, these software tools lack the ability to track individual cells and work on two-dimensional images only. In contrast, our software tool improved this process by its capability of processing 3D stacks, without the need for compression to two dimensions, and by its segmentation of single cells, instead of measuring entire areas of fluorescence. Thus, our approach allows for more precise tracking of cells in the 3D environment of the larvae. In combination with the tool's ability to measure

multiple fluorescent signals within each segmented cell, this could also enable future research to accurately determine the cellular uptake of fluorescent probes, such as fluorescently labeled NDDSs. While in its current form the software gave satisfactory data analysis, there are some improvements that could be made, such as automatic larva segmentation and improved resilience to background fluorescence. An overview of suggestions is given in Future perspectives.

5.2 EHop-016 as an anti-AML drug

Our work continued by investigating the use of the Rac1 inhibitor EHop-016 for the treatment of AML. Here, the zebrafish larva, in combination with our software tool, played a vital role in demonstrating the drug's effectiveness *in vivo* through inhibition of cell migration to the hematopoietic niche, as well as cytotoxic effects by itself and in combination with DNR. The zebrafish model also uncovered a toxic effect on the circulatory system in the form of cardiac arrest and blood vessel obstruction at concentrations of 50 µM in-water. Such physiological changes are difficult to detect by *in vitro* studies. While we were not able to pinpoint the exact cause for this toxic effect, it could be linked to the previously reported reduction in blood vessel formation around cancer tumors in mice after EHop-016 treatment [48]. With the larval circulatory system still being under development during our experiments, disruptions in angiogenesis could have a profound impact [11].

We demonstrated the ability of EHop-016 to inhibit migration of MOLM-13 AML cells both over a porous membrane *in vitro*, and to the CHT in zebrafish larvae. With the CHT acting as a hematopoietic niche in zebrafish, and hematopoietic signaling being highly preserved compared to mammals, this finding could predict a similar effect in humans [13]. In our research, we could however not confirm the precise reason for this inhibition, a possibility being a reduction in cell motility, rather than an inhibition of homing towards the cytokine SDF-1, which is expressed in hematopoietic tissues in both mammals and zebrafish [100]. A reduced homing of AML cells to the hematopoietic niche could prove a valuable tool for future treatment. Leukemic stem cells have been found to endure chemotherapy in the bone marrow,

leading to later relapse of the disease [101]. We also observed a similar effect in Paper I, where MOLM-13 cells seemed to persist in the CHT after treatment with DNR.

While the *in vitro* effects of EHop-016 alone were promising, its activity in combination with DNR emphasized that it could have a potential role in future AML treatment. The combined treatment of drugs that inhibits the homing of cancer cells to the hematopoietic niche with other chemotherapy agents have already been investigated, such as the combination of the CXCR4 antagonist BL-8040 and cytarabine [102]. Here, monotherapy of patients with BL-8040 triggered the mobilization of blasts into the peripheral blood, and combined treatment of BL-8040 and high dose cytarabine over five days increased overall survival. Our *in vitro* studies on MOLM-13 cells treated with combinations between EHop-016 and DNR demonstrated a synergistic cytotoxic effect between the drugs. *In vivo*, our results also showed a significantly increased effect of the drug combination compared to either drug in monotherapy, although we did not perform a full synergy study as in the cell experiments due to the comparatively low number of samples.

A potential drawback of EHop-016 is its short half-life of elimination of around 4.5 h in mice [103]. However, a significant inhibition of tumor growth and metastasis of transplanted breast cancer cells has still been reported in a mouse model following EHop-016 administration every other day [48]. In our experiments with zebrafish larvae, we avoided the reported rapid clearance by administrating the drug in water, since the uptake of EHop-016 through the skin was demonstrated in our toxicity results, as well as for other small molecules in previous studies [104]. While EHop-016 clearance in humans has not been investigated, frequent administration could become necessary to achieve an optimal effect. A potential alternative way of increasing circulation time of a drug is the use of NDDSs [105]. With EHop-016 containing aromatic groups, graphene could be a potential NDDS through pi-stacking [106].

5.3 Impact of the graphene production method on toxicity

Our work concluded with an investigation into the promising NDDS graphene. We wanted to know how it impacts cells *in vitro*, as well gather *in vivo* documentation on how it affects key elements in the innate immune system involved in clearance of

NDDSs. Graphene has previously been shown to be a potential NDDS for drugs capable of pi-stacking, with its variety of functional groups found on sheet edges and defect sites enabling a large potential for customization, such as active targeting through antibodies or increased biocompatibility through functionalization with polyethylene glycol [107]. While graphene is readily produced on a small scale through sonication in laboratories, microfluidization has been shown to enable higher yields and a large potential for scalability [90, 91]. For us, an additional point of interest was the reported generation of oxygen rich defects following graphene production using sonication [108]. This could lead to graphene with higher oxygen induced toxicity and increased complement activation [109, 110].

The *in vitro* investigation showed a large difference in toxicity and complement system activation between graphene produced through sonication and microfluidization. For graphene produced through microfluidization, toxic concentrations were not reached, while graphene produced through sonication reached LD_{50} at 70 µg/ml and 100 µg/ml in HUVEC and SW948 cells, respectively. In complement activation studies, sonication resulted in graphene with an approximately 10 times larger activation per μm^2 surface when compared to microfluidization.

In contrast, the toxicity was found to be low for graphene of either production method administered through IV injections in zebrafish larvae. A possible explanation could be the coating of the graphene sheets by zebrafish blood proteins. Such a protein coating has previously been found to reduce cytotoxicity of graphene oxide [111]. Alternatively, an observation for all graphene samples was the formation of visible agglomerates, primarily in the CHT area. These agglomerates could reduce the available surface area for interactions with cells.

Further investigation included zebrafish larvae with fluorescent macrophages. As indicated by the complement activation studies, phagocytosis of graphene agglomerates was observed for both production methods. Using our software tool, we tracked macrophage populations over the course of two days following graphene injection. For the microfluidized graphene samples, we detected a reduction in total

macrophage count, as well as a reduction in macrophage concentration in the CHT area, one day following exposure. While this reduction could indicate an effect on macrophages, another explanation could be a reduction of fluorescent signal due to absorption and quenching by graphene following phagocytosis [112]. Sonicated graphene exhibited an opposite effect. One day following exposure, the macrophage distribution exhibited a shift towards the CHT, without decreasing the total number of observed macrophages compared to the control groups. Two days following exposure, macrophage distributions returned to a state similar to the control groups, but with macrophage counts significantly increased. We believe this to indicate firstly a response of the macrophages to migrate towards areas with high graphene concentrations, followed by an increase in macrophage production.

The findings following exposure to sonicated graphene contradict the earlier mentioned graphene-induced masking of the fluorescent signal. An explanation for this could be that an increased macrophage count in the larvae is compensating for macrophages not detected due to masking, or an increased macrophage presence in the CHT distributing the material more evenly between these cells and hence keep the fluorescent signal detectable. Alternatively, graphene-induced masking of the macrophages is a less pronounced effect, and the transient reduction in macrophage count following exposure to microfluidized graphene due to cytotoxic effects.

In this paper, the use of zebrafish larvae greatly increased our insight into the behavior of the graphene materials. While initial complement system activation studies indicated an elevated immunoreactivity, the effects of these findings could be further investigated in the larva model. Additionally, if the observed accumulation of graphene in the CHT translates to accumulation in the bone marrow for humans, this could be exploited for targeted delivery of drugs to this tissue. In general, the main benefit of this model for NDDS development is the ability to fine-tune aspects such as avoidance of the immune system, targeting of desired tissues, and toxicity. This can be completed prior to animal studies in mammals, reducing the time required for development and reducing the number of animal experiments.

5.4 Zebrafish larvae as model in myeloid malignancy drug development

In our research, the zebrafish larva proved to be an efficient and versatile tool to investigate several important aspects in drug discovery. Using this model, we were able to conduct toxicity and drug efficacy investigations within the brief time span of five days from zebrafish egg fertilization to experiment conclusion. Utilizing the transparency of the casper strain and fluorescent microscopy, we were also able to observe single cells *in situ*, a feat not possible in model animals such as mice.

The use of our software greatly improved the data acquisition from zebrafish larvae. This was not only evident in our cell tracking approach, but also through other means such as the heart rate detecting algorithm presented in Paper I, with both tools being utilized in other studies currently ongoing in our research group. If assisted by for instance machine learning, tracking of fluorescent cells could be further improved, and the segmentation and characterization of larval organs could lead to even more detailed studies of toxicity from data acquisition methods as simple as microscopy timelapse.

The ease of genetic manipulation is also a great source of versatility for this model system with the ability to establish new zebrafish lines over the course of a few months [113]. While we only utilized zebrafish with fluorescent macrophages (Paper III), an additional benefit for our research could have been a zebrafish line with a fluorescent marker coupled with the fli1 promoter, which is expressed in endothelial cells [114]. Using this method, migration of the intravenously injected cancer cells through the endothelium and into the CHT could have been observed using a time lapse. This would also be helpful to precisely detect the circulation time of fluorescently labelled NDDS.

An additional use of the genetic manipulation of zebrafish is the production of zebrafish lines with pre-programmed tumor development. This can be achieved by increasing the likelihood of cancer development through selective overexpression or downregulation of tumor promoters or repressor genes, but also by coupling the activation of cancer promoting genes to external factors, such as the activation of the

heat shock gene [115, 116]. For research in larvae, these approaches are however less suitable due to the time needed for the cancer to develop. In our work we focused on the use of cancer transplantation instead. This allowed us to investigate different cancer types without the need for separate zebrafish lines, and also facilitated the study of cancer models within the short five-day period from fertilization to euthanasia.

The use of zebrafish embryos and larvae is encouraged to reduce the need for *in vivo* experiments in more developed animals [117]. This is part of the three Rs in animal research: Replacement, Reduction and Refinement. Here, these experiments aid in replacement, through the usage of lower-order larvae instead of fully gown rodents as described by the European Animal Research Association [118]. While zebrafish larvae are not a complete replacement for pre-clinical trials in for instance small mammals, these investigations also aid in reduction. By thoroughly characterizing the effects under investigation in zebrafish larvae, estimates of effect sizes can be obtained, and subsequent power analyses give the lowest number of subjects required for sufficient statistical power. Finally, animal experiments can be refined through the detection of unexpected toxic effects, such as the circulatory toxicity found in Paper II. Using this information, experiments can be designed to mitigate these issues, or determine humane endpoints adjusted to spare research animals from unnecessary suffering.

With the benefits of this model in mind, care should still be taken when working with zebrafish larvae. While zebrafish up to five dpf are not included in the European convention for animal research [14], and approval for experiments is not needed, research should still be conducted ethically during this stage of development. In our work, we reduced the stress on larvae through sedation prior to procedures like imaging, injection, and removal of the chorion. Additionally, larvae unsuited for further experimentation, for example due to developmental errors or mistakes during handling, were immediately euthanized.

Within *in vitro* studies, another field is emerging that competes with the zebrafish larva model as a tool to bridge the gap between traditional cell studies and studies in higher-order animals, the field of 3D cell models [5]. In contrast to traditional two-

dimensional cell models, with cells either floating individually in suspension or being attached to the bottom of a container, 3D cell models try to better emulate the microenvironment found in organisms. 3D cell models come in various forms, such as spheroids, collections of cells arranged in small spheres to mimic the environment in tissues, scaffolding, where cells are cultured in pre-made extracellular matrix scaffolds, and microfluidic platforms, complex tissue-organ constructs which allow for the vascularization of the model and study of metastatic behavior. These models greatly increase the complexity compared to 2D cell studies while being more affordable and ethical than animal research in mice [5]. Compared to the zebrafish larva model, these systems have an advantage by being able to exclusively use human cells, requiring less infrastructure, and having fewer ethical concerns, even considering the early developmental stages of larvae prior to five dpf. However, these models are not yet able to emulate the complexity of an entire organism. Another drawback are also increasing cost with increasing complexity, with a single microfluidic platform from a supplier such as SynVivo® costing over $100 [119]. These drawbacks still ensure a place for the zebrafish larva model in drug development.

In retrospect, while our work showed promising results, some improvements could increase the output of our research. The first target of improvement lies in the further development of the zebrafish model to the myeloid malignancies investigated. A large reduction in cancer burden was detected in all experiments following transplantation. In animal models such as mice, a latency period is also observed following transplantation before the cancer starts proliferating [120]. A longer experiment period could have minimized this effect by allowing the cancer to acclimatize prior to treatment. This would however in turn require authorization from the Norwegian Food Safety Authority, the Norwegian department responsible for animal research, since the duration of the experiments would exceed five days post fertilization. Another approach to optimize the conditions for transplanted cells are humanized zebrafish larvae. An example is the zebrafish strain presented by Rajan *et al*., which produces the human cytokines SDF-1 and colony stimulating factor 2 [18]. These larvae are reported to increase migration and survivability of transplanted hematopoietic cells. The targeting of the signal axis between zebrafish SDF-1 and its

receptor CXCR4 has however been demonstrated in zebrafish larvae without the use of humanized lines [121]. We also successfully demonstrated the reduced accumulation of AML cells in the zebrafish hematopoietic niche following Rac1 inhibition in Paper II, however, using larvae expressing human versions of these cytokines could lead to more pronounced results. The interleukin IL-3 is not expressed in the zebrafish line presented by Rajan *et al.* A zebrafish line expressing human IL-3 could also be useful for further experiments using MDS-L cells, which requires IL-3 supplement for optimal proliferation *in vitro* [18, 70].

Additionally, the staining process used to mark cancer cells had to be performed close to the time of injection, due to the eventual fading of fluorescence as the cells proliferate. The staining procedure could add additional stress on the cells, leaving them in a more vulnerable state prior to transplantation and treatment. While the control groups were subjected to the same stress, hence preserving comparability between the groups, we tried to avoid this issue through the use of genetically modified MOLM-13 cells, expressing the green fluorescent protein. This did however yield poor signal-to-noise ratios in confocal microscopy images and was not further pursued. The genetic manipulation of cell lines could also impact their response to treatments, and thus reduce the reliability of results.

Finally, the assessment of toxicity through the study of visual abnormalities can give valuable insights, however, toxic effects on tissues can be hard to detect, especially within the three-day window from exposure to euthanasia. For more an accurate determination of toxic effects, larvae with fluorescently labeled reporter genes could have been utilized. This, in turn, is limited by the range of toxic effects being detectable by each reporter gene and would require a large number of gene modified zebrafish lines to fully study a drugs toxicity.

6 Concluding remarks

Our aim was to further develop the zebrafish larva as a tool for myeloid malignancy research and evaluate its usefulness in treatment development. We demonstrated the versatility and efficiency of this model in research on novel treatment options needed for these diseases. The power of the zebrafish larvae in cancer research lies especially in the combined approach of whole larva imaging and computer assisted data processing. Coupled with the wide range of fluorescent markers and probes available for cancer cells and zebrafish larvae, this system can be quickly adapted to answer many research questions related to cancer or other research where fluorescent probes can be used.

Our findings on the effects of EHop-016 and DNR highlighted this system's advantages. The protective effect of the hematopoietic niche on cancer cells as well as the adverse effects of EHop-016 on the circulatory system could not been detected by *in vitro* experiments. Furthermore, for the proper evaluation and documentation of for instance biocompatibility of NDDSs, the complexity of *in vitro* assays is insufficient. While some toxic effects might become evident *in vitro*, aspects like biodistribution, passive or active targeting, or circulation time require the complexity of an organism for study.

7 Future perspectives

The software presented in Paper I was found to be a valuable tool during this work. Nevertheless, there are possibilities for improving this software. While the segmentation algorithm used was able to segment single cells, it struggled with low signal-to-noise ratios and irregular background fluorescence. The implementation of a more sophisticated segmentation algorithm could make this tool more resilient to these factors and versatile for different applications. Methods such as the machine learning approach of region-based convolutional neural networks could hold promise to alleviate this issue, although the large image size could become an obstacle with present limitations in computational power. Additionally, changes in application or instrumentation could require re-training of the network, and hence the creation of new training data sets. Other improvements such as automatic detection and segmentation of the larvae in confocal images and automatic background detection could further reduce the need for user input, to the point were setting up the experiment in the software is the only step needed. Lastly, more untapped information is stored in the confocal files, such as larvae size and morphology. Acquisition of these factors could also be implemented in the software, thereby maximizing the data obtained from each larva.

The drug EHop-016 showed potential as a complementary treatment to DNR in Paper II. Future research should explore this compound in combination with other drugs than DNR to find if an even better drug synergy can be achieved. Additionally, the experiments conducted were limited to short-term exposure to the treatments. New experiments focusing on longer treatment times could give additional insight in the synergistic effects between EHop-016 and DNR or other drugs. While the zebrafish larva model used in this paper did yield good results, the research could benefit from more humanized models such as previously mentioned.

Paper III demonstrated little toxicity of graphene in zebrafish larvae, however, macrophage distributions and counts were impacted following exposure. Future investigation should focus on determining whether a reduction in fluorescent signal or cytotoxicity led to the observed results for microfluidized graphene and investigate

the reason behind macrophage migration and increased count in larvae exposed to sonicated graphene. For this, fluorescently labeled graphene sheets could be utilized. Since the software developed in Paper I supports the measurement of multiple fluorescent channels, co-location of graphene and macrophages could be easily measured.

8 References

(1) Dohner, H.; Wei, A. H.; Appelbaum, F. R.; Craddock, C.; DiNardo, C. D.; Dombret, H.; Ebert, B. L.; Fenaux, P.; Godley, L. A.; Hasserjian, R. P.; et al. Diagnosis and management of AML in adults: 2022 recommendations from an international expert panel on behalf of the ELN. *Blood* **2022**, *140* (12), 1345-1377. DOI: 10.1182/blood.2022016867

(2) Bazinet, A.; Bravo, G. M. New Approaches to Myelodysplastic Syndrome Treatment. *Current Treatment Options in Oncology* **2022**, *23* (5), 668-687. DOI: 10.1007/s11864-022-00965-1

(3) Lichtman, M. A. A historical perspective on the development of the cytarabine (7days) and daunorubicin (3days) treatment regimen for acute myelogenous leukemia: 2013 the 40th anniversary of 7+3. *Blood Cells Mol Dis* **2013**, *50* (2), 119-130. DOI: 10.1016/j.bcmd.2012.10.005

(4) Hughes, J. P.; Rees, S.; Kalindjian, S. B.; Philpott, K. L. Principles of early drug discovery. *British Journal of Pharmacology* **2011**, *162* (6), 1239-1249. DOI: 10.1111/j.1476-5381.2010.01127.x

(5) Antunes, N.; Kundu, B.; Kundu, S. C.; Reis, R. L.; Correlo, V. In Vitro Cancer Models: A Closer Look at Limitations on Translation. *Bioengineering (Basel)* **2022**, *9* (4). DOI: 10.3390/bioengineering9040166

(6) Kiani, A. K.; Pheby, D.; Henehan, G.; Brown, R.; Sieving, P.; Sykora, P.; Marks, R.; Falsini, B.; Capodicasa, N.; Miertus, S.; et al. Ethical considerations regarding animal experimentation. *J Prev Med Hyg* **2022**, *63* (2 Suppl 3), E255-E266. DOI: 10.15167/2421-4248/jpmh2022.63.2S3.2768

(7) Patton, E. E.; Zon, L. I.; Langenau, D. M. Zebrafish disease models in drug discovery: from preclinical modelling to clinical trials. *Nat Rev Drug Discov* **2021**, *20* (8), 611-628. DOI: 10.1038/s41573-021-00210-8

(8) Sharpe, S. *Zebra Danios: Among the Easiest Fish to Keep in Aquariums*. The Spruce Pets, https://www.thesprucepets.com/zebra-danio-1378473 (accessed October 26, 2023).

(9) Simonsen, L. *A female zebrafish, Danio rerio*. Public Domain, https://commons.wikimedia.org/w/index.php?title=File:Danio_rerio_port.jpg&oldid=468896147 (accessed October 26, 2023).

(10) Letunic, I.; Bork, P. Interactive Tree Of Life (iTOL) v5: an online tool for phylogenetic tree display and annotation. *Nucleic Acids Research* **2021**, *49* (W1), W293-W296. DOI: 10.1093/nar/gkab301

(11) Kimmel, C. B.; Ballard, W. W.; Kimmel, S. R.; Ullmann, B.; Schilling, T. F. Stages of embryonic development of the zebrafish. *Dev Dyn* **1995**, *203* (3), 253-310. DOI: 10.1002/aja.1002030302

(12) Suster, M. L.; Kikuta, H.; Urasaki, A.; Asakawa, K.; Kawakami, K. Transgenesis in Zebrafish with the Tol2 Transposon System. In *Transgenesis Techniques*, Methods in Molecular Biology, 2009; pp 41-63. ISBN: 978-1-60327-018-2.

(13) Gore, A. V.; Pillay, L. M.; Venero Galanternik, M.; Weinstein, B. M. The zebrafish: A fintastic model for hematopoietic development and disease. *Wiley Interdiscip Rev Dev Biol* **2018**, *7* (3), e312. DOI: 10.1002/wdev.312

(14) *Commission Implementing Decision (EU) 2020/569*; The European Commission, Official Journal of the European Union, http://data.europa.eu/eli/dec_impl/2020/569/oj.
(15) *Directive 2010/63/EU*; The European Parliament and The European Council, Official Journal of the European Union, http://data.europa.eu/eli/dir/2010/63/2019-06-26.
(16) Hickman, D. L.; Johnson, J.; Vemulapalli, T. H.; Crisler, J. R.; Shepherd, R. Commonly Used Animal Models. In *Principles of Animal Research*, 2017; pp 117-175. ISBN: 9780128021514.
(17) White, R. M.; Sessa, A.; Burke, C.; Bowman, T.; LeBlanc, J.; Ceol, C.; Bourque, C.; Dovey, M.; Goessling, W.; Burns, C. E.; Zon, L. I. Transparent adult zebrafish as a tool for in vivo transplantation analysis. *Cell Stem Cell* **2008**, *2* (2), 183-189. DOI: 10.1016/j.stem.2007.11.002
(18) Rajan, V.; Melong, N.; Hing Wong, W.; King, B.; Tong, S. R.; Mahajan, N.; Gaston, D.; Lund, T.; Rittenberg, D.; Dellaire, G.; et al. Humanized zebrafish enhance human hematopoietic stem cell survival and promote acute myeloid leukemia clonal diversity. *Haematologica* **2020**, *105* (10), 2391-2399. DOI: 10.3324/haematol.2019.223040
(19) Miao, K. Z.; Kim, G. Y.; Meara, G. K.; Qin, X.; Feng, H. Tipping the Scales With Zebrafish to Understand Adaptive Tumor Immunity. *Front Cell Dev Biol* **2021**, *9*, 660969. DOI: 10.3389/fcell.2021.660969
(20) *What Is Cancer?* American Cancer Society, https://www.cancer.org/cancer/understanding-cancer/what-is-cancer.html (accessed 26.October.2023).
(21) Weinberg, R. A. The biology of cancer. Second edition. ed.; Garland Science, 2014; pp 331-332. ISBN: 9780815342199.
(22) Weinberg, R. A. The biology of cancer. Second edition. ed.; Garland Science, 2014; pp 723-724. ISBN: 9780815342199.
(23) Travlos, G. S. Normal Structure, Function, and Histology of the Bone Marrow. *Toxicologic Pathology* **2016**, *34* (5), 548-565. DOI: 10.1080/01926230600939856
(24) Zhang, Y.; Gao, S.; Xia, J.; Liu, F. Hematopoietic Hierarchy – An Updated Roadmap. *Trends in Cell Biology* **2018**, *28* (12), 976-986. DOI: 10.1016/j.tcb.2018.06.001
(25) Mangi, M. H.; Newland, A. C. Interleukin-3: Promises and Perspectives. *Hematology* **1998**, *3* (1), 55-66. DOI: 10.1080/10245332.1998.11752123
(26) Lau, T. T.; Wang, D. A. Stromal cell-derived factor-1 (SDF-1): homing factor for engineered regenerative medicine. *Expert Opin Biol Ther* **2011**, *11* (2), 189-197. DOI: 10.1517/14712598.2011.546338
(27) Chennamadhavuni, A.; Lyengar, V.; Mukkamalla, S. K. R.; Shimanovsky, A. Leukemia. In *StatPearls*; 2023; PMID: 32809325.
(28) Arber, D. A.; Orazi, A.; Hasserjian, R. P.; Borowitz, M. J.; Calvo, K. R.; Kvasnicka, H. M.; Wang, S. A.; Bagg, A.; Barbui, T.; Branford, S.; et al. International Consensus Classification of Myeloid Neoplasms and Acute Leukemias: integrating morphologic, clinical, and genomic data. *Blood* **2022**, *140* (11), 1200-1228. DOI: 10.1182/blood.2022015850

(29) Alaggio, R.; Amador, C.; Anagnostopoulos, I.; Attygalle, A. D.; Araujo, I. B. O.; Berti, E.; Bhagat, G.; Borges, A. M.; Boyer, D.; Calaminici, M.; et al. The 5th edition of the World Health Organization Classification of Haematolymphoid Tumours: Lymphoid Neoplasms. *Leukemia* **2022**, *36* (7), 1720-1748. DOI: 10.1038/s41375-022-01620-2
(30) Albitar, M.; Manshouri, T.; Shen, Y.; Liu, D.; Beran, M.; Kantarjian, H. M.; Rogers, A.; Jilani, I.; Lin, C. W.; Pierce, S.; et al. Myelodysplastic syndrome is not merely "preleukemia". *Blood* **2002**, *100* (3), 791-798. DOI: 10.1182/blood.v100.3.791
(31) *Blood Cancer Statistics*. Leukemia & Lymphoma Society, https://www.lls.org/facts-and-statistics/facts-and-statistics-overview (accessed 26.October 2023).
(32) *Key Statistics for Acute Myeloid Leukemia (AML)*. American Cancer Society, https://www.cancer.org/cancer/acute-myeloid-leukemia/about/key-statistics.html (accessed 26.October.2023).
(33) *Akutt myelogen leukemi (AML)*. NHI, https://nhi.no/sykdommer/barn/kreftsykdommer/akutt-myelogen-leukemi-oversikt/?page=all (accessed 26.October.2023).
(34) Pelcovits, A.; Niroula, R. Acute Myeloid Leukemia: A Review. *R I Med J (2013)* **2020**, *103* (3), 38-40.
(35) Dotson, J. L.; Lebowicz, Y. Myelodysplastic Syndrome. In *StatPearls*; 2023; PMID: 30480932.
(36) *Key Statistics for Myelodysplastic Syndromes*. American Cancer Society, https://www.cancer.org/cancer/types/myelodysplastic-syndrome/about/key-statistics.html (accessed 26.October.2023).
(37) *MDS*. Helsedirektoratet, https://www.helsedirektoratet.no/retningslinjer/maligne-blodsykdommer-handlingsprogram/myelodysplastisk-syndrom-mds-og-kronisk-myelo-monocyttleukemi-kmml/mds (accessed 26. October 2023).
(38) List, A.; Dewald, G.; Bennett, J.; Giagounidis, A.; Raza, A.; Feldman, E.; Powell, B.; Greenberg, P.; Thomas, D.; Stone, R.; et al. Lenalidomide in the Myelodysplastic Syndrome with Chromosome 5q Deletion. *New England Journal of Medicine* **2006**, *355* (14), 1456-1465. DOI: 10.1056/NEJMoa061292
(39) *Typical Treatment of Acute Myeloid Leukemia (Except APL)*. American Cancer Society, https://www.cancer.org/cancer/types/acute-myeloid-leukemia/treating/typical-treatment-of-aml.html (accessed 25.October.2023).
(40) Balassa, K.; Danby, R.; Rocha, V. Haematopoietic stem cell transplants: principles and indications. *Br J Hosp Med (Lond)* **2019**, *80* (1), 33-39. DOI: 10.12968/hmed.2019.80.1.33
(41) Malcovati, L.; Hellstrom-Lindberg, E.; Bowen, D.; Ades, L.; Cermak, J.; Del Canizo, C.; Della Porta, M. G.; Fenaux, P.; Gattermann, N.; Germing, U.; et al. Diagnosis and treatment of primary myelodysplastic syndromes in adults: recommendations from the European LeukemiaNet. *Blood* **2013**, *122* (17), 2943-2964. DOI: 10.1182/blood-2013-03-492884

(42) Daver, N.; Pollyea, D. A.; Rizzieri, D. A.; Palmer, J.; Rampal, R. K.; Dinner, S.; Bixby, D. L.; Percival, M.-E. M.; Kovacsovics, T.; Begna, K. H.; et al. A Phase I Study of FLX925, a Dual FLT3 and CDK4/6 Inhibitor in Patients with Relapsed or Refractory Acute Myeloid Leukemia (AML). *Blood* **2017**, *130* (Supplement 1), 1343-1343. DOI: 10.1182/blood.V130.Suppl_1.1343.1343 (acccessed 10/30/2023).
(43) Peterlin, P.; Le Bris, Y.; Turlure, P.; Chevallier, P.; Ménard, A.; Gourin, M.-P.; Dumas, P.-Y.; Thepot, S.; Berceanu, A.; Park, S.; et al. CPX-351 in higher risk myelodysplastic syndrome and chronic myelomonocytic leukaemia: a multicentre, single-arm, phase 2 study. *The Lancet Haematology* **2023**, *10* (7), e521-e529. DOI: 10.1016/s2352-3026(23)00090-x
(44) Garitano-Trojaola, A.; Sancho, A.; Gotz, R.; Eiring, P.; Walz, S.; Jetani, H.; Gil-Pulido, J.; Da Via, M. C.; Teufel, E.; Rhodes, N.; et al. Actin cytoskeleton deregulation confers midostaurin resistance in FLT3-mutant acute myeloid leukemia. *Commun Biol* **2021**, *4* (1), 799. DOI: 10.1038/s42003-021-02215-w
(45) Wang, J.; Rao, Q.; Wang, M.; Wei, H.; Xing, H.; Liu, H.; Wang, Y.; Tang, K.; Peng, L.; Tian, Z.; Wang, J. Overexpression of Rac1 in leukemia patients and its role in leukemia cell migration and growth. *Biochem Biophys Res Commun* **2009**, *386* (4), 769-774. DOI: 10.1016/j.bbrc.2009.06.125
(46) Cancelas, J. A.; Jansen, M.; Williams, D. A. The role of chemokine activation of Rac GTPases in hematopoietic stem cell marrow homing, retention, and peripheral mobilization. *Exp Hematol* **2006**, *34* (8), 976-985. DOI: 10.1016/j.exphem.2006.03.016
(47) Yang, J.; Qiu, Q.; Qian, X.; Yi, J.; Jiao, Y.; Yu, M.; Li, X.; Li, J.; Mi, C.; Zhang, J.; et al. Long noncoding RNA LCAT1 functions as a ceRNA to regulate RAC1 function by sponging miR-4715-5p in lung cancer. *Mol Cancer* **2019**, *18* (1), 171. DOI: 10.1186/s12943-019-1107-y
(48) Castillo-Pichardo, L.; Humphries-Bickley, T.; De La Parra, C.; Forestier-Roman, I.; Martinez-Ferrer, M.; Hernandez, E.; Vlaar, C.; Ferrer-Acosta, Y.; Washington, A. V.; Cubano, L. A.; et al. The Rac Inhibitor EHop-016 Inhibits Mammary Tumor Growth and Metastasis in a Nude Mouse Model. *Translational Oncology* **2014**, *7* (5), 546-555. DOI: 10.1016/j.tranon.2014.07.004
(49) Parapini, S.; Paone, S.; Erba, E.; Cavicchini, L.; Pourshaban, M.; Celani, F.; Contini, A.; D'Alessandro, S.; Olivieri, A. In Vitro Antimalarial Activity of Inhibitors of the Human GTPase Rac1. *Antimicrob Agents Chemother* **2022**, *66* (1), e0149821. DOI: 10.1128/AAC.01498-21
(50) Tiwari, G.; Tiwari, R.; Sriwastawa, B.; Bhati, L.; Pandey, S.; Pandey, P.; Bannerjee, S. K. Drug delivery systems: An updated review. *Int J Pharm Investig* **2012**, *2* (1), 2-11. DOI: 10.4103/2230-973X.96920
(51) Krauss, A. C.; Gao, X.; Li, L.; Manning, M. L.; Patel, P.; Fu, W.; Janoria, K. G.; Gieser, G.; Bateman, D. A.; Przepiorka, D.; et al. FDA Approval Summary: (Daunorubicin and Cytarabine) Liposome for Injection for the Treatment of Adults with High-Risk Acute Myeloid Leukemia. *Clin Cancer Res* **2019**, *25* (9), 2685-2690. DOI: 10.1158/1078-0432.CCR-18-2990

(52) Gregoriadis, G. Liposomes and mRNA: Two technologies together create a COVID-19 vaccine. *Medicine in Drug Discovery* **2021**, *12*. DOI: 10.1016/j.medidd.2021.100104
(53) Avramović, N.; Mandić, B.; Savić-Radojević, A.; Simić, T. Polymeric Nanocarriers of Drug Delivery Systems in Cancer Therapy. *Pharmaceutics* **2020**, *12* (4). DOI: 10.3390/pharmaceutics12040298
(54) Di, J.; Gao, X.; Du, Y.; Zhang, H.; Gao, J.; Zheng, A. Size, shape, charge and "stealthy" surface: Carrier properties affect the drug circulation time in vivo. *Asian Journal of Pharmaceutical Sciences* **2021**, *16* (4), 444-458. DOI: 10.1016/j.ajps.2020.07.005
(55) Sharifi, M.; Cho, W. C.; Ansariesfahani, A.; Tarharoudi, R.; Malekisarvar, H.; Sari, S.; Bloukh, S. H.; Edis, Z.; Amin, M.; Gleghorn, J. P.; et al. An Updated Review on EPR-Based Solid Tumor Targeting Nanocarriers for Cancer Treatment. *Cancers (Basel)* **2022**, *14* (12). DOI: 10.3390/cancers14122868
(56) Salahpour Anarjan, F. Active targeting drug delivery nanocarriers: Ligands. *Nano-Structures & Nano-Objects* **2019**, *19*. DOI: 10.1016/j.nanoso.2019.100370
(57) Suk, J. S.; Xu, Q.; Kim, N.; Hanes, J.; Ensign, L. M. PEGylation as a strategy for improving nanoparticle-based drug and gene delivery. *Advanced Drug Delivery Reviews* **2016**, *99*, 28-51. DOI: 10.1016/j.addr.2015.09.012
(58) Novoselov, K. S.; Geim, A. K.; Morozov, S. V.; Jiang, D.; Katsnelson, M. I.; Grigorieva, I. V.; Dubonos, S. V.; Firsov, A. A. Two-dimensional gas of massless Dirac fermions in graphene. *Nature* **2005**, *438* (7065), 197-200. DOI: 10.1038/nature04233
(59) Novoselov, K. S.; Jiang, D.; Schedin, F.; Booth, T. J.; Khotkevich, V. V.; Morozov, S. V.; Geim, A. K. Two-dimensional atomic crystals. *Proc Natl Acad Sci U S A* **2005**, *102* (30), 10451-10453. DOI: 10.1073/pnas.0502848102
(60) Gerstner, E. Nobel Prize 2010: Andre Geim & Konstantin Novoselov. *Nature Physics* **2010**, *6* (11), 836-836. DOI: 10.1038/nphys1836
(61) Shen, H.; Zhang, L.; Liu, M.; Zhang, Z. Biomedical Applications of Graphene. *Theranostics* **2012**, *2* (3), 283-294. DOI: 10.7150/thno.3642
(62) Kaur, G.; Dufour, J. M. Cell lines: Valuable tools or useless artifacts. *Spermatogenesis* **2012**, *2* (1), 1-5. DOI: 10.4161/spmg.19885
(63) Capes-Davis, A.; Theodosopoulos, G.; Atkin, I.; Drexler, H. G.; Kohara, A.; MacLeod, R. A.; Masters, J. R.; Nakamura, Y.; Reid, Y. A.; Reddel, R. R.; Freshney, R. I. Check your cultures! A list of cross-contaminated or misidentified cell lines. *Int J Cancer* **2010**, *127* (1), 1-8. DOI: 10.1002/ijc.25242
(64) Matsuo, Y.; MacLeod, R. A.; Uphoff, C. C.; Drexler, H. G.; Nishizaki, C.; Katayama, Y.; Kimura, G.; Fujii, N.; Omoto, E.; Harada, M.; Orita, K. Two acute monocytic leukemia (AML-M5a) cell lines (MOLM-13 and MOLM-14) with interclonal phenotypic heterogeneity showing MLL-AF9 fusion resulting from an occult chromosome insertion, ins(11;9)(q23;p22p23). *Leukemia* **1997**, *11* (9), 1469-1477. DOI: 10.1038/sj.leu.2400768

(65) Quentmeier, H.; Reinhardt, J.; Zaborski, M.; Drexler, H. G. FLT3 mutations in acute myeloid leukemia cell lines. *Leukemia* **2003**, *17* (1), 120-124. DOI: 10.1038/sj.leu.2402740
(66) Wu, M.; Li, L.; Hamaker, M.; Small, D.; Duffield, A. S. FLT3-ITD cooperates with Rac1 to modulate the sensitivity of leukemic cells to chemotherapeutic agents via regulation of DNA repair pathways. *Haematologica* **2019**, *104* (12), 2418-2428. DOI: 10.3324/haematol.2018.208843
(67) Skopek, R.; Palusinska, M.; Kaczor-Keller, K.; Pingwara, R.; Papierniak-Wygladala, A.; Schenk, T.; Lewicki, S.; Zelent, A.; Szymanski, L. Choosing the Right Cell Line for Acute Myeloid Leukemia (AML) Research. *Int J Mol Sci* **2023**, *24* (6). DOI: 10.3390/ijms24065377
(68) Somasagara, R. R.; Huang, X.; Xu, C.; Haider, J.; Serody, J. S.; Armistead, P. M.; Leung, T. Targeted therapy of human leukemia xenografts in immunodeficient zebrafish. *Scientific Reports* **2021**, *11* (1). DOI: 10.1038/s41598-021-85141-5
(69) Tohyama, K.; Tsutani, H.; Ueda, T.; Nakamura, T.; Yoshida, Y. Establishment and characterization of a novel myeloid cell line from the bone marrow of a patient with the myelodysplastic syndrome. *Br J Haematol* **1994**, *87* (2), 235-242. DOI: 10.1111/j.1365-2141.1994.tb04904.x
(70) Nakamura, S.; Ohnishi, K.; Yoshida, H.; Shinjo, K.; Takeshita, A.; Tohyama, K.; Ohno, R.; Koide, Y. Retrovirus-mediated gene transfer of granulocyte colony-stimulating factor receptor (G-CSFR) cDNA into MDS cells and induction of their differentiation by G-CSF. *Cytokines Cell Mol Ther* **2000**, *6* (2), 61-70. DOI: 10.1080/13684730050515787
(71) Oltova, J.; Svoboda, O.; Bartunek, P. Hematopoietic Cytokine Gene Duplication in Zebrafish Erythroid and Myeloid Lineages. *Frontiers in Cell and Developmental Biology* **2018**, *6*. DOI: 10.3389/fcell.2018.00174
(72) Carey, T.; Alhourani, A.; Tian, R.; Seyedin, S.; Arbab, A.; Maughan, J.; Šiller, L.; Horvath, D.; Kelly, A.; Kaur, H.; et al. Cyclic production of biocompatible few-layer graphene ink with in-line shear-mixing for inkjet-printed electrodes and Li-ion energy storage. *npj 2D Materials and Applications* **2022**, *6* (1). DOI: 10.1038/s41699-021-00279-0
(73) Leibovitz, A.; Stinson, J. C.; McCombs, W. B., 3rd; McCoy, C. E.; Mazur, K. C.; Mabry, N. D. Classification of human colorectal adenocarcinoma cell lines. *Cancer Res* **1976**, *36* (12), 4562-4569.
(74) Siow, R. C. Culture of human endothelial cells from umbilical veins. *Methods Mol Biol* **2012**, *806*, 265-274. DOI: 10.1007/978-1-61779-367-7_18
(75) *Cell Counting Kit-8*. Dojindo, https://www.dojindo.com/EUROPE/products/CK04/ (accessed 25. October 2023).
(76) *Thymidine Incorporation Assay*. Thermo Fisher Scientific, https://www.thermofisher.com/no/en/home/references/protocols/cell-and-tissue-analysis/cell-profilteration-assay-protocols/angiogenesis-protocols/thymidine-incorporation-assay.html (accessed October 26, 2023).
(77) Crowley, L. C.; Marfell, B. J.; Scott, A. P.; Waterhouse, N. J. Quantitation of Apoptosis and Necrosis by Annexin V Binding, Propidium Iodide Uptake, and

Flow Cytometry. *Cold Spring Harb Protoc* **2016**, *2016* (11). DOI: 10.1101/pdb.prot087288
(78) Hu, V. W.; Black, G. E.; Torres-Duarte, A.; Abramson, F. P. 3H-thymidine is a defective tool with which to measure rates of DNA synthesis. *FASEB J* **2002**, *16* (11), 1456-1457. DOI: 10.1096/fj.02-0142fje
(79) Givan, A. L. Flow cytometry: an introduction. *Methods Mol Biol* **2011**, *699*, 1-29. DOI: 10.1007/978-1-61737-950-5_1
(80) Bliss, C. I. The calculation of microbial assays. *Bacteriol Rev* **1956**, *20* (4), 243-258. DOI: 10.1128/br.20.4.243-258.1956
(81) Bergseth, G.; Ludviksen, J. K.; Kirschfink, M.; Giclas, P. C.; Nilsson, B.; Mollnes, T. E. An international serum standard for application in assays to detect human complement activation products. *Mol Immunol* **2013**, *56* (3), 232-239. DOI: 10.1016/j.molimm.2013.05.221
(82) Cassar, S.; Adatto, I.; Freeman, J. L.; Gamse, J. T.; Iturria, I.; Lawrence, C.; Muriana, A.; Peterson, R. T.; Van Cruchten, S.; Zon, L. I. Use of Zebrafish in Drug Discovery Toxicology. *Chem Res Toxicol* **2020**, *33* (1), 95-118. DOI: 10.1021/acs.chemrestox.9b00335
(83) *European Convention for the protection of vertebrate animals used for experimental and other scientific purposes*; Official Journal, http://data.europa.eu/eli/convention/1999/575/oj.
(84) Elliott, A. D. Confocal Microscopy: Principles and Modern Practices. *Curr Protoc Cytom* **2020**, *92* (1), e68. DOI: 10.1002/cpcy.68
(85) Ollion, J.; Cochennec, J.; Loll, F.; Escude, C.; Boudier, T. TANGO: a generic tool for high-throughput 3D image analysis for studying nuclear organization. *Bioinformatics* **2013**, *29* (14), 1840-1841. DOI: 10.1093/bioinformatics/btt276
(86) Brigham, E. O.; Morrow, R. E. The fast Fourier transform. *IEEE Spectrum* **1967**, *4* (12), 63-70. DOI: 10.1109/mspec.1967.5217220
(87) Schindelin, J.; Arganda-Carreras, I.; Frise, E.; Kaynig, V.; Longair, M.; Pietzsch, T.; Preibisch, S.; Rueden, C.; Saalfeld, S.; Schmid, B.; et al. Fiji: an open-source platform for biological-image analysis. *Nature Methods* **2012**, *9* (7), 676-682. DOI: 10.1038/nmeth.2019
(88) Kawakami, K. Tol2: a versatile gene transfer vector in vertebrates. *Genome Biology* **2007**, *8* (Suppl 1). DOI: 10.1186/gb-2007-8-s1-s7
(89) Ellett, F.; Pase, L.; Hayman, J. W.; Andrianopoulos, A.; Lieschke, G. J. mpeg1 promoter transgenes direct macrophage-lineage expression in zebrafish. *Blood* **2011**, *117* (4), e49-e56. DOI: 10.1182/blood-2010-10-314120
(90) Hernandez, Y.; Nicolosi, V.; Lotya, M.; Blighe, F. M.; Sun, Z.; De, S.; McGovern, I. T.; Holland, B.; Byrne, M.; Gun'Ko, Y. K.; et al. High-yield production of graphene by liquid-phase exfoliation of graphite. *Nature Nanotechnology* **2008**, *3* (9), 563-568. DOI: 10.1038/nnano.2008.215
(91) Karagiannidis, P. G.; Hodge, S. A.; Lombardi, L.; Tomarchio, F.; Decorde, N.; Milana, S.; Goykhman, I.; Su, Y.; Mesite, S. V.; Johnstone, D. N.; et al. Microfluidization of Graphite and Formulation of Graphene-Based Conductive Inks. *ACS Nano* **2017**, *11* (3), 2742-2755. DOI: 10.1021/acsnano.6b07735

(92) Trache, A.; Meininger, G. A. Atomic force microscopy (AFM). *Curr Protoc Microbiol* **2008**, *Chapter 2*, Unit 2C 2. DOI: 10.1002/9780471729259.mc02c02s8
(93) Fischer, E. R.; Hansen, B. T.; Nair, V.; Hoyt, F. H.; Dorward, D. W. Scanning electron microscopy. *Curr Protoc Microbiol* **2012**, *Chapter 2*, Unit 2B 2. DOI: 10.1002/9780471729259.mc02b02s25
(94) Stetefeld, J.; McKenna, S. A.; Patel, T. R. Dynamic light scattering: a practical guide and applications in biomedical sciences. *Biophysical Reviews* **2016**, *8* (4), 409-427. DOI: 10.1007/s12551-016-0218-6
(95) Ferrari, A. C.; Basko, D. M. Raman spectroscopy as a versatile tool for studying the properties of graphene. *Nature Nanotechnology* **2013**, *8* (4), 235-246. DOI: 10.1038/nnano.2013.46
(96) Schneider, C. A.; Rasband, W. S.; Eliceiri, K. W. NIH Image to ImageJ: 25 years of image analysis. *Nature Methods* **2012**, *9* (7), 671-675. DOI: 10.1038/nmeth.2089
(97) Mikut, R.; Dickmeis, T.; Driever, W.; Geurts, P.; Hamprecht, F. A.; Kausler, B. X.; Ledesma-Carbayo, M. J.; Marée, R.; Mikula, K.; Pantazis, P.; et al. Automated Processing of Zebrafish Imaging Data: A Survey. *Zebrafish* **2013**, *10* (3), 401-421. DOI: 10.1089/zeb.2013.0886
(98) Yamamoto, D.; Sato, D.; Nakayama, H.; Nakagawa, Y.; Shimada, Y. ZF-Mapper: Simple and Complete Freeware for Fluorescence Quantification in Zebrafish Images. *Zebrafish* **2019**, *16* (3). DOI: 10.1089/zeb.2018.1683
(99) Carreira, M. J.; Vila-Blanco, N.; Cabezas-Sainz, P.; Sánchez, L. ZFTool: A Software for Automatic Quantification of Cancer Cell Mass Evolution in Zebrafish. *Applied Sciences* **2021**, *11* (16). DOI: 10.3390/app11167721
(100) Glass, T. J.; Lund, T. C.; Patrinostro, X.; Tolar, J.; Bowman, T. V.; Zon, L. I.; Blazar, B. R. Stromal cell-derived factor-1 and hematopoietic cell homing in an adult zebrafish model of hematopoietic cell transplantation. *Blood* **2011**, *118* (3), 766-774. DOI: 10.1182/blood-2011-01-328476
(101) Wang, J. Y.; Yu, P.; Chen, S.; Xing, H.; Chen, Y.; Wang, M.; Tang, K.; Tian, Z.; Rao, Q.; Wang, J. Activation of Rac1 GTPase promotes leukemia cell chemotherapy resistance, quiescence and niche interaction. *Mol Oncol* **2013**, *7* (5), 907-916. DOI: 10.1016/j.molonc.2013.05.001
(102) Borthakur, G.; Ofran, Y.; Tallman, M. S.; Foran, J.; Uy, G. L.; DiPersio, J. F.; Showel, M. M.; Shimoni, A.; Nagler, A.; Rowe, J. M.; et al. BL-8040 CXCR4 antagonist is safe and demonstrates antileukemic activity in combination with cytarabine for the treatment of relapsed/refractory acute myelogenous leukemia: An open-label safety and efficacy phase 2a study. *Cancer* **2021**, *127* (8), 1246-1259. DOI: 10.1002/cncr.33338
(103) Humphries-Bickley, T.; Castillo-Pichardo, L.; Corujo-Carro, F.; Duconge, J.; Hernandez-O'Farrill, E.; Vlaar, C.; Rodriguez-Orengo, J. F.; Cubano, L.; Dharmawardhane, S. Pharmacokinetics of Rac inhibitor EHop-016 in mice by ultra-performance liquid chromatography tandem mass spectrometry. *J Chromatogr B Analyt Technol Biomed Life Sci* **2015**, *981-982*, 19-26. DOI: 10.1016/j.jchromb.2014.12.021

(104) Tamplin, O. J.; White, R. M.; Jing, L.; Kaufman, C. K.; Lacadie, S. A.; Li, P.; Taylor, A. M.; Zon, L. I. Small molecule screening in zebrafish: swimming in potential drug therapies. *Wiley Interdiscip Rev Dev Biol* **2012**, *1* (3), 459-468. DOI: 10.1002/wdev.37
(105) Cai, S. S.; Li, T.; Akinade, T.; Zhu, Y.; Leong, K. W. Drug delivery carriers with therapeutic functions. *Adv Drug Deliv Rev* **2021**, *176*, 113884. DOI: 10.1016/j.addr.2021.113884
(106) Zhuang, W. R.; Wang, Y.; Cui, P. F.; Xing, L.; Lee, J.; Kim, D.; Jiang, H. L.; Oh, Y. K. Applications of pi-pi stacking interactions in the design of drug-delivery systems. *J Control Release* **2019**, *294*, 311-326. DOI: 10.1016/j.jconrel.2018.12.014
(107) Sattari, S.; Adeli, M.; Beyranvand, S.; Nemati, M. Functionalized Graphene Platforms for Anticancer Drug Delivery. *Int J Nanomedicine* **2021**, *16*, 5955-5980. DOI: 10.2147/IJN.S249712
(108) Skaltsas, T.; Ke, X.; Bittencourt, C.; Tagmatarchis, N. Ultrasonication Induces Oxygenated Species and Defects onto Exfoliated Graphene. *The Journal of Physical Chemistry C* **2013**, *117* (44), 23272-23278. DOI: 10.1021/jp4057048
(109) Gurunathan, S.; Arsalan Iqbal, M.; Qasim, M.; Park, C. H.; Yoo, H.; Hwang, J. H.; Uhm, S. J.; Song, H.; Park, C.; Do, J. T.; et al. Evaluation of Graphene Oxide Induced Cellular Toxicity and Transcriptome Analysis in Human Embryonic Kidney Cells. *Nanomaterials (Basel)* **2019**, *9* (7). DOI: 10.3390/nano9070969
(110) Wibroe, P. P.; Petersen, S. V.; Bovet, N.; Laursen, B. W.; Moghimi, S. M. Soluble and immobilized graphene oxide activates complement system differently dependent on surface oxidation state. *Biomaterials* **2016**, *78*, 20-26. DOI: 10.1016/j.biomaterials.2015.11.028
(111) Chong, Y.; Ge, C.; Yang, Z.; Garate, J. A.; Gu, Z.; Weber, J. K.; Liu, J.; Zhou, R. Reduced Cytotoxicity of Graphene Nanosheets Mediated by Blood-Protein Coating. *ACS Nano* **2015**, *9* (6), 5713-5724. DOI: 10.1021/nn5066606
(112) Kasry, A.; Ardakani, A. A.; Tulevski, G. S.; Menges, B.; Copel, M.; Vyklicky, L. Highly Efficient Fluorescence Quenching with Graphene. *The Journal of Physical Chemistry C* **2012**, *116* (4), 2858-2862. DOI: 10.1021/jp207972f
(113) Singleman, C.; Holtzman, N. G. Growth and Maturation in the Zebrafish,Danio Rerio: A Staging Tool for Teaching and Research. *Zebrafish* **2014**, *11* (4), 396-406. DOI: 10.1089/zeb.2014.0976
(114) Lawson, N. D.; Weinstein, B. M. In Vivo Imaging of Embryonic Vascular Development Using Transgenic Zebrafish. *Developmental Biology* **2002**, *248* (2), 307-318. DOI: 10.1006/dbio.2002.0711
(115) Shoji, W.; Sato-Maeda, M. Application of heat shock promoter in transgenic zebrafish. *Dev Growth Differ* **2008**, *50* (6), 401-406. DOI: 10.1111/j.1440-169X.2008.01038.x
(116) Hason, M.; Bartunek, P. Zebrafish Models of Cancer-New Insights on Modeling Human Cancer in a Non-Mammalian Vertebrate. *Genes (Basel)* **2019**, *10* (11). DOI: 10.3390/genes10110935

(117) Bauer, B.; Mally, A.; Liedtke, D. Zebrafish Embryos and Larvae as Alternative Animal Models for Toxicity Testing. *Int J Mol Sci* **2021**, *22* (24). DOI: 10.3390/ijms222413417
(118) *The 3Rs in animal research*. European Animal Research Association, https://www.eara.eu/the-3rs-in-animal-research (accessed 26.October.2023).
(119) *SynTumor 3D Cancer Model – Recreating The Tumor Microenvironment*. SynVivo®, https://www.synvivobio.com/syntumor/ (accessed 26. October 2023).
(120) Siolas, D.; Hannon, G. J. Patient-Derived Tumor Xenografts: Transforming Clinical Samples into Mouse Models. *Cancer Research* **2013**, *73* (17), 5315-5319. DOI: 10.1158/0008-5472.Can-13-1069
(121) Tulotta, C.; Stefanescu, C.; Beletkaia, E.; Bussmann, J.; Tarbashevich, K.; Schmidt, T.; Snaar-Jagalska, B. E. Inhibition of signaling between human CXCR4 and zebrafish ligands by the small molecule IT1t impairs the formation of triple-negative breast cancer early metastases in a zebrafish xenograft model. *Dis Model Mech* **2016**, *9* (2), 141-153. DOI: 10.1242/dmm.023275

© 2022. Published by The Company of Biologists Ltd | Biology Open (2022) 11, bio059530. doi:10.1242/bio.059530

METHODS & TECHNIQUES

A new software tool for computer assisted *in vivo* high-content analysis of transplanted fluorescent cells in intact zebrafish larvae

Jan-Lukas Førde[1,2], Ingeborg Nerbø Reiten[1], Kari Espolin Fladmark[3], Astrid Olsnes Kittang[1,5] and Lars Herfindal[1,*]

ABSTRACT

Acute myeloid leukemia and myelodysplastic syndromes are cancers of the bone marrow with poor prognosis in frail and older patients. To investigate cancer pathophysiology and therapies, confocal imaging of fluorescent cancer cells and their response to treatments in zebrafish larvae yields valuable information. While zebrafish larvae are well suited for confocal imaging, the lack of efficient processing of large datasets remains a severe bottleneck. To alleviate this problem, we present a software tool that segments cells from confocal images and track characteristics such as volume, location in the larva and fluorescent intensity on a single-cell basis. Using this software tool, we were able to characterise the responses of the cancer cell lines Molm-13 and MDS-L to established treatments. By utilizing the computer-assisted processing of confocal images as presented here, more information can be obtained while being less time-consuming and reducing the demand of manual data handling, when compared to a manual approach, thereby accelerating the pursuit of novel anti-cancer treatments. The presented software tool is available as an ImageJ java-plugin at https://zenodo.org/10.5281/zenodo.7383160 and the source code at https://github.com/Jfo004/ConfocalCellSegmentation.

KEY WORDS: Acute myeloid leukaemia, Myelodysplastic syndrome, Confocal imaging, Cell segmentation, Automatic image processing, Zebrafish

INTRODUCTION

Cancer remains a major cause of death in both industrialised and developed countries, despite intensive research. This can partly be explained by the complexity and heterogeneity of the disease, but also due to lack of good models for drug screening. This is particularly valid for the myeloid malignancies acute myeloid leukaemia (AML) and myelodysplastic syndromes (MDS). While alternative treatments such as hematopoietic stem cell transplantation (HSCT) and immunotherapies like CAR-t-cell therapy exist, most patients rely on chemotherapy at some time during the treatment. A challenge in the treatment of MDS and AML as well as many other cancers is that elderly or patients with poor general condition are unsuited for curative treatments like HSCT and have to resort to chemotherapy (Liu, 2021; Saygin and Carraway, 2021). Moreover, these patients also have low tolerance for intensive chemotherapy. For AML, the median survival is 5 to 10 months in elderly and frail patients, and for high-risk MDS patients, the only remaining treatment is hypomethylating agents like azacitidine (Aza), which gives an increased median survival of 10 months compared to supportive care (Döhner et al., 2015; Fenaux et al., 2009). While some new treatments are in clinical trials or have been approved in the last decade, such as Enasidenib for AML and MDS patients with IDH_2 mutation, a demand for novel treatments persist (Cazzola, 2020). Taken into consideration the heterogeneity of AML and MDS, and cancer in general, there is a need for more tailored therapies. However, to facilitate rapid drug development, there is a dire need for relevant models that allow for testing of for instance a novel drug candidate on a large number of various cancer cells representing the different sub-classes of the disease. At present, this is not feasible using rodent models due to price and ethical considerations, and *in vitro* models are not able to fully recreate the complex microenvironment that the cancer cells reside in.

Zebrafish have become an intriguing tool for the development of anti-cancer therapies. The species shares around 70% of the human genes and has orthologues for approximately 80% of proteins linked to human diseases (Molina et al., 2021). Compared to mammalian disease models like mice, zebrafish possess several benefits such as high fecundity rate, low maintenance cost and ease of genetic manipulation. Zebrafish are also translucent during the early stages of development or even throughout adulthood in the genetically modified zebrafish line Casper, which enables the use of optical microscopy techniques on living subjects (White et al., 2008). Especially well-suited for drug screening are zebrafish during the embryonal and larval period, due to their aforementioned optical transparency, small size, and absence of an adaptive immune system until 4 to 6 weeks post-fertilization, while still having important and relevant anatomical structures and physiological processes (Molina et al., 2021; Sullivan et al., 2017).

In cancer research, observing the response of cancer cells to treatments, as well as interactions between the cancer and host, is highly valuable. By injecting fluorescently labelled cancer cells in zebrafish embryo and larvae, these interactions can be observed using confocal microscopy. While zebrafish embryos and larvae are well suited for microscopy, processing of the acquired data remains a significant bottleneck (Mikut et al., 2013). Automated processing methods can enable larger scale high-content screenings using confocal microscopy where the manual data processing and analysis limits the amount of information that can be mined. Some solutions of this problem are already devised (Carreira et al., 2021; Yamamoto et al., 2019); however, these solutions are optimised to work on 2D

[1]Centre for Pharmacy, Department of Clinical Science, University of Bergen, 5021 Bergen, Norway. [2]Department of Internal Medicine, Haukeland University Hospital, 5021 Bergen, Norway. [3]Department of Biological Sciences, University of Bergen, 5006 Bergen, Norway. [4]Division for Haematology, Department of Medicine, Haukeland University Hospital, 5021 Bergen, Norway. [5]Department of Clinical Science, University of Bergen, 5021 Bergen, Norway.

*Author for correspondence (lars.herfindal@uib.no)

L.H., 0000-0003-0353-3614

Received 11 July 2022; Accepted 2 November 2022

Biology Open (2022) 11, bio059530. doi:10.1242/bio.059530

microscope images. This approach struggles to identify individual cells if these are overlapping in the image plane, hence it identifies fluorescent areas instead of individual cells. This causes some shortfalls, for instance inaccurate determination of cancer cell locations and colocalization with other fluorescent elements of interests due to the lack of one spatial coordinate. Additionally, agglomerations of fluorescent cell fragments or debris may be mistaken for cells since only the total fluorescent area is considered instead of the size of individual objects.

The aim of the present work was to develop a software that can improve the field of automatic image analysis for zebrafish cancer models compared to previously published tools (Carreira et al., 2021; Yamamoto et al., 2019). Our approach processes 3D confocal images and segments individual cells, which enables high-content image analysis for zebrafish larvae models of myeloid malignancies, as well as other cancers. The software tool was evaluated by investigating the proliferation of AML and MDS cells in zebrafish embryo and larvae, and their response to the drugs daunorubicin (DNR) and Aza determined. We illustrate the use of single cell detection to extract additional information from confocal images, such as cell volume distributions and *in vivo* cell density maps. To evaluate the potential cardiotoxic effects of the administered treatments, we utilised a simple algorithm to automatically detect the larva heart rates from 10-s microscope videos.

RESULTS AND DISCUSSION

Cell segmentation

A large amount of data are contained in images obtained by confocal microscopy. However, this information can quickly be lost during data processing due to the feature extraction from 3D confocal images being very time consuming and highly cumbersome. To alleviate this problem, we developed a software tool that automatically segments cells and further extracts relevant information from the acquired images. Here, we injected zebrafish larvae with fluorescently labelled leukaemia cells at 2 days post-fertilization (dpf) and imaged daily using confocal microscopy until 5 dpf. While Kimmel et al. defined the transition between the embryonic and larval stages to occur at after the protruding-mouth stage at 72 h post-fertilization, for convenience and to avoid confusion, we use the term zebrafish larva for all stages from the day of injection at 2 dpf (Kimmel et al., 1995).

An overview of the segmentation process is given in Fig. 1A. The process starts by flattening the confocal stack to a 2D representation using a user selected projection method for the fluorescent channel, such as a max-projection, and stack sharpening for the brightfield channel. This is followed by the selection of larval boundaries for alignment as well as background removal. Following larval segmentation, the user can adjust background levels as well as masking sources of autofluorescence to enable the segmentation of fluorescent objects within the larva. While the 2D representation of the confocal stack is used during background adjustment, for cell segmentation the entire 3D stack is used. Alternatives to manual background removal can be achieved using techniques such as the iterative threshold approach used by Carreira et al. (2021). However, such approach did not yield satisfactory results in our data due to excessive removal of weakly fluorescent cancer cells or inclusion of regions with high autofluorescence. Alternatives to intensity-threshold based methods like fluorescence lifetime imaging could be applied for background removal. Where such a technique is not available, computational methods can be utilised. Automatic removal of background fluorescence could be performed using machine learning or by including additional factors, such as location within the image, comparison of multiple image channels and/or edge detection within the segmentation algorithm, however, development of these methods is beyond the scope of the work presented here.

Fig. 1B shows a typical confocal image following stack flattening and larva segmentation. While the area outside the larva is visible in this image, during cell segmentation, only fluorescent objects within the larvae are included. The larva depicted was injected with Molm-13 cells stained with the fluorescent marker CellTracker™ Deep Red Dye at 2 dpf and imaged using confocal microscopy the following day. Common areas of auto fluorescence include the gut, yolk sack and iridophores as marked by black arrows in Fig. 1B. These areas can however readily be masked during the cell segmentation process. Fluorescent objects above the user-set background level are segmented using a watershed algorithm. This

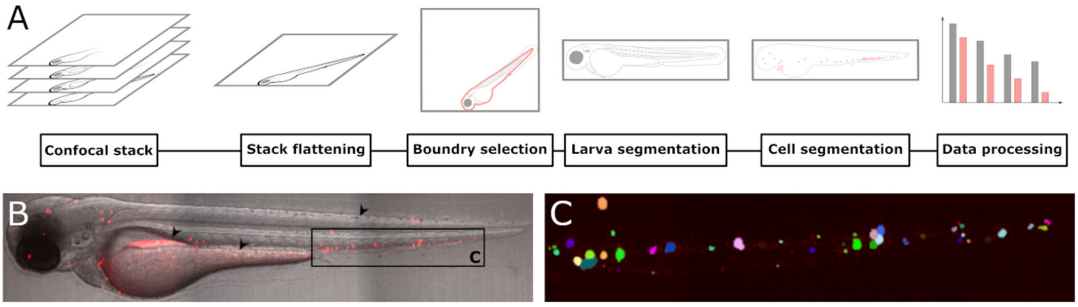

Fig. 1. Processing of confocal images derived from zebrafish larvae intravenously injected with fluorescent cells. The workflow for segmenting cells from confocal images is illustrated in A. Acquired confocal images are first flattened to a 2D representation to enable easy visual analysis. Following flattening, the larval boundaries are selected by the user to determine the location and orientation of the larva. Using this information, the larvae are segmented and realigned to a standardised orientation. Background levels are determined by the user and all objects located within the larva are segmented using a watershed algorithm. Next, the data can be exported for further analysis. An example of the cell segmentation is given in B and C. A zebrafish larva was injected with 4 nL of a 10 10^6 cells·ml^{-1} CellTracker™ Deep Red-stained cancer cell suspension into the posterior cardinal vein at 2 dpf. A 2D representation of a confocal image acquired the day after cell injection is shown in B. Common sources of autofluorescence that need to be masked prior to segmentation are the gut, yolk sack and iridophores as indicated by black arrows. Cell segmentation of the tail region (indicated by the black rectangle in B) is displayed in C. To illustrate the segmentation, each segmented object detected is represented by a unique colour.

Biology Open (2022) 11, bio059530. doi:10.1242/bio.059530

results in the segmentation of single objects even if multiple objects are in contact, as long as a border between the objects is detectable in the fluorescent channel. To illustrate this, Fig. 1C shows the segmentation of single objects within the framed area marked with 'C' in Fig. 1B. Each object is given a unique colour to illustrate successful segmentation.

The cell segmentation performed by our tool also enables collection of additional data for individual cells such as fluorescent intensity in all acquired channels, volume, and precise location within the zebrafish larva. If the images are flattened before analysis, which is the case for many other analysis tools, information is lost, and quantitative and qualitative analysis of single cells is limited. For instance, information of fluorescent intensity could be used to monitor proliferation of the cancer cells, since the fluorophore concentration in cells is halved for every division. This enables the distinction between treatments that kill cancer cells and those that lead to senescence, as the latter would retain a higher fluorescent intensity compared to dividing cells. An illustration of plots comparing cell volumes to the average fluorescence of cells is given in Fig. S1 for Molm-13 cells in untreated and DNR-treated zebrafish larvae. These plots demonstrate that cell fluorescence decrease over time, correlating with cell division, and further that cell size decreases in DNR-treated larvae. The latter suggests the presence of apoptotic cells. Additionally, since the boundaries and positions of cells are known, cut-outs containing single cells can be extracted from the original confocal image and further analysed in a manner similar to imaging flow cytometry.

Identification of viable cancer cells based on volume distributions

When imaging fluorescently labelled cells in zebrafish larvae, not every fluorescent object may represent a cell. Apoptotic bodies or cell fragments can still retain the fluorescent stain and be misidentified as viable cells even after being phagocytosed by macrophages. A method for separating these objects from viable cells can be achieved by using volume information to distinguish larger cells from smaller fragments.

To determine the lower threshold volume for viable cells, a volume distribution was created using the segmented objects of all injected larvae at the day of cell injection. As a comparison to cells in zebrafish larvae, cells stained with CellTracker™ Deep Red were kept in medium and imaged using confocal microscopy. The resulting volume distributions are shown in Fig. 2. Based on these volume distribution plots, the volume thresholds for viable cells were determined to be above $\approx$1000 μm^3 for both Molm-13 and MDS-L. This volume responds to an equivalent spherical diameter of above 12 µm. The measured size can however be impacted by scattering in the z-plane when acquiring confocal images. This will cause objects to appear stretched along the z-axis and can impact accurate measurement of volumes. However, all measured objects are affected in a similar manner, and their relative differences are still readily detectable. Compared to Molm-13, the size distribution of MDS-L exhibited two populations at the day of injection (Fig. 2D). This population, consisting of objects with smaller volume as shown in white, could represent fragments from apoptotic cells. Such fragments will rapidly be phagocytosed by macrophages, and the small fluorescent objects seen in Fig. S2 could therefore be both free apoptotic bodies, as well engulfed material inside macrophages. It is apparent that Mom-13 cells tolerate the handling prior to injection better than the MDS-L judged by the relatively large amount of sub-cellular fluorescent particles present in the MDS-L-injected larvae (Fig. 2D).

Distribution of injected Molm-13 and MDS-L cell lines in zebrafish larvae

The precise position of each detected object with a volume above the predetermined threshold of 1000 μm^3 was recorded during cell segmentation. Using this data, density maps of injected Molm-13 or MDS-L cells in zebrafish larvae were constructed as seen in Figs 3 and 4, respectively, with Fig. S4 illustrating variations in the distribution between the larvae. It is important to note that each of the density maps in Figs 3 and 4 are normalised to the highest value within that map, and not to the other treatments. This makes each distribution clearer; however, changes in cell counts between density maps are not visualised

At the day of injection, a high cell density can also be seen around the injection site in the posterior cardinal vein in Molm-13 (Fig. 3A,E), and in the heart region for MDS-L (Fig. 4A,E). From 1 day post injection (dpi) until the end of the experiments (3 dpi), both cell lines accumulated in the ventral tail region around the caudal vein. This region houses the caudal haematopoietic tissue (CHT) from 2 to 5 dpf (Gore et al., 2018). A possible explanation for this accumulation could be a selective exit from the bloodstream by the cancer cells at a haematopoietic niche due to cytokines which also attract human leukaemia cells, whose natural environment is the bone marrow.

The Molm-13 cell distributions obtained from larvae treated with DNR (Fig. 3E-H) show a lower cell density around the posterior cardinal vein compared to the untreated transplanted control, while the population in the CHT remains strong. The reduction of cancer cells around the posterior cardinal vein can be a result of the injection site of DNR being in the same area; however, the high injection velocity of the drug, as well as a functioning circulatory system likely result in a rapid and even distribution of the drug in the blood. Thus, a more likely explanation is that the AML cells are more protected from DNR when residing in the haematopoietic niche in the CHT.

In larvae injected with MDS-L, the regions outside the CHT were found to have a higher cell density in control larvae without injection compared to larvae treated with Aza (Fig. 4A-D and E-H, respectively). A notable outlier can be observed in Fig. 4H, where a high cell density can be found around the posterior cardinal vein in Aza-treated larvae when compared to control larvae (Fig. 4D). The MDS-L cells are therapy resistant, and the new population around the posterior cardinal vein could be the formation of a new colony outside the CHT, presumably in the kidney, which takes over as the main haematopoietic tissue at around 4-5 dpf (Paik and Zon, 2010).

Quantification of tumour burden in zebrafish larvae

As well as determining the positions of segmented cells, the software tool also measures cell count and volumes. Using this information, the temporal development of tumour burden was compared in larvae transplanted with Molm-13 or MDS-L. The larvae were then given anti-cancer treatment, blank injections, or no treatment (Fig. 5). We observed a decline in tumour burden in untreated larvae throughout the 3-day observation period. This can be due to the stress the cells are subjected to from handling before and during the injection, as well as the temperature change from 37°C in the incubator to 31°C in the zebrafish. The decrease in cell numbers was highest during the first 24 h, and less dramatic at 2 and 3 dpi for Molm-13 (Fig. 5A,B) with mitotic activity being evident as illustrated in Fig. S2. This indicates that the cancer cells have adapted to the new microenvironment. Such an initial decline in engrafted cells is also seen in mammalian cancer models such as mice, where patient derived xenografts in immunosuppressed mice

Biology Open (2022) 11, bio059530. doi:10.1242/bio.059530

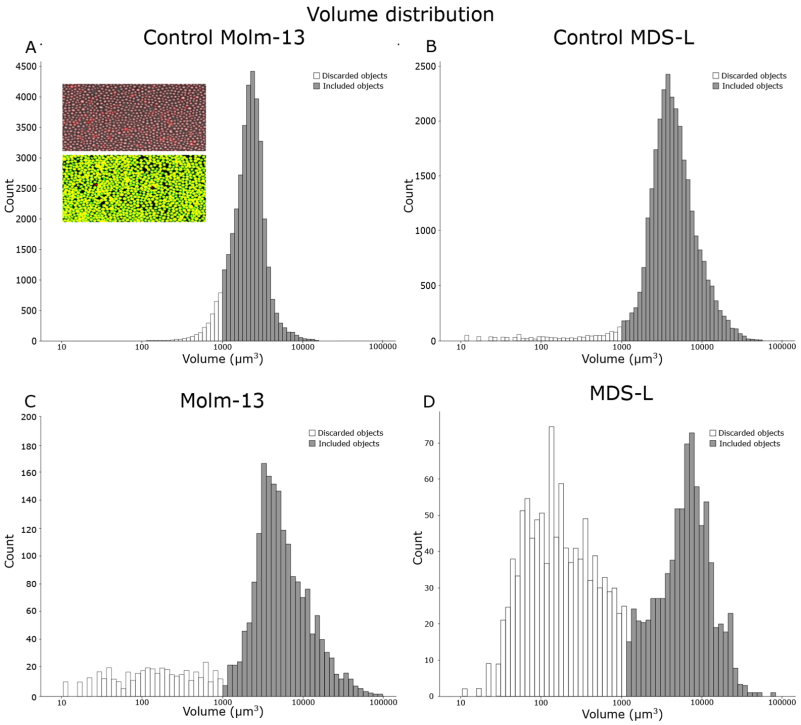

Fig. 2. *In vitro* and *in vivo* measurement of cancer cell volume distributions based on confocal images. Cultured Molm-13 AML and MDS-L cells were stained with CellTracker™ Deep Red and imaged by confocal microscopy (A and B, respectively). An illustration of the segmentation process is shown as inset in A, with the composite fluorescence and brightfield image shown at the top and the resulting segmentation below (composite image of red fluorescence and segmented overlay in green). The plots illustrate the volume distribution with objects below the volume threshold of 1000 µm^3 shown in white and above in grey. For volume distributions of cancer cells in zebrafish larvae, 4 nL of 10 10^6 cells·ml^{-1} CellTracker™ Deep Red-stained cancer cell suspensions were injected into the posterior cardinal vein of 18 zebrafish larvae at 2 dpf. Following cell injection, the larvae were imaged by confocal microscopy, and the images processed as the control samples in A and B. Volume distributions for the cell lines Molm-13 and MDS-L in zebrafish larvae are given in C and D, respectively. Using the volume distribution from A and B, a lower volume cut-off for viable cells was determined. The cell populations above and below this threshold are shown in grey and white, respectively. The plots are combined numbers from 3 images in A and B, and 9 larvae for each group in C and D. An illustration of the inter-larvae variation is given in Fig. S3.

have an initial latency period followed by proliferation (Siolas and Hannon, 2013).

The combined volumes of up to 16 Molm-13 injected larvae given different treatment, without and with volume gating are shown in Fig. 5A and B, respectively. As seen in Fig. 5B, larvae treated with DNR (red) displayed a significantly lower tumour burden compared to untreated larvae (grey) throughout the observation period. Injection with Milli-Q® water (green) did not lead to a significant decrease in tumour burden. Since the fluorescence is also visible in apoptotic cells, it is important to exclude small cell fragments to be able to quantify the amount of living cells. An impact on the volume distribution of Molm-13 cells due to the DNR treatment can also be seen as shown along the y-axis of Fig. S1. The combined cell volumes of MDS-L cells without and with volume gating are shown in Fig. 5C and D, respectively. In contrast to Molm-13 cells treated with DNR, no significant difference in total tumour burden can be seen in MDS-L cells treated with Aza. This can be attributed to the slow mechanism of action for hypomethylating drugs as observed in *in vitro* studies, but also that the MDS-L cell line is therapy resistant, and not likely to respond to this drug.

Monitoring cardiotoxic effect from the anti-cancer drugs Daunorubicin and Azacitidine

The use of zebrafish larva as a model for cardiotoxic drugs has been demonstrated in several studies (Maciag et al., 2022; Zhu et al., 2014). Usually, the cardiotoxic effects are monitored by manually counting the heart rate. In addition to being time-consuming, this can also lead to biased results if not performed blindly. However, by using a software to count the heart rate of zebrafish larvae, both these issues are eliminated. The macro used for these measurements uses intensity fluctuations in the acquired microscope videos due to the larva's heartbeat. A detailed description of this is given in the Materials and Methods section.

Previous studies have shown that anthracyclines reduce heart rate in zebrafish larvae (Han et al., 2015), and we wanted to test whether we could observe this effect using our macro for calculating heart rate. A reduction in heart rate for DNR-treated larvae occurred only at 1 dpi, but not at 2 and 3 dpi (Fig. 6D). This could be because of elimination of DNR by metabolism or excretion. Also, zebrafish are known to be able to regenerate tissue, and heart regeneration has been observed in adult fish (Poss et al., 2002).

Biology Open (2022) 11, bio059530. doi:10.1242/bio.059530

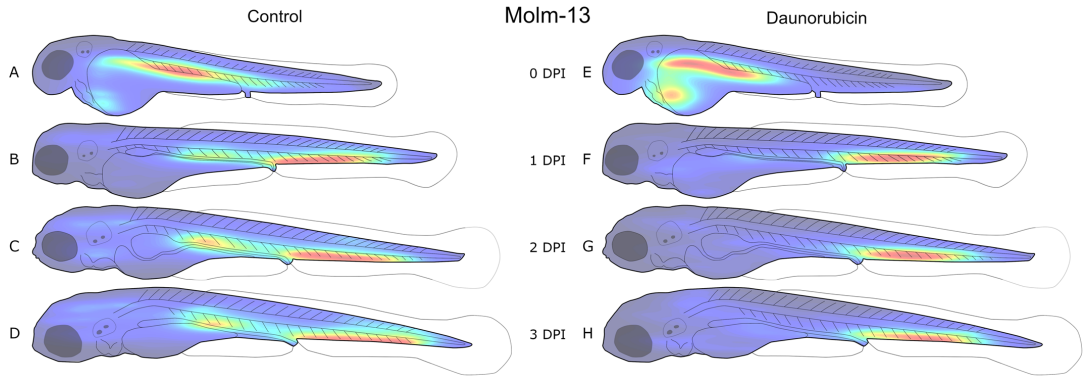

Fig. 3. Distribution of Molm-13 cells in zebrafish larvae after intravenous injection with daunorubicin. 4 nL of a 10 10^6 cells·ml^{-1} CellTracker™ Deep Red-stained Molm-13 cell suspension was injected into 18 zebrafish larvae at 2 dpf, and either left untreated (A-D, *n*=9) or treated with a 4 nL injection of 1 mM daunorubicin (E-H, *n*=9). Each larva was imaged daily using confocal microscopy, and the images analysed using our ImageJ plugin as described in the Materials and Methods section. The location of each cell above the volume threshold determined in Fig. 2C was used to create a combined distribution map for each group on each dpi. The density map was generated using MATLAB and visualises the areas of highest (red) and lowest (blue) cell density. Each density map is normalised to its own highest and lowest values; thus, it only visualises distribution, not total tumour burden. An illustration of the variation between replicates is given in Fig. S4.

In the fish treated with Aza, there was an increased heart rate at 2 dpi (Fig. 6E). The effect could be a stress reaction of multiple injections of the cytostatic drug. In contrast to DNR, the effect of Aza on the heart of zebrafish is little studied, but one report showed reduced survival, malformations and cardiac effects such as pericardial oedema and reduced ventricular volume at 3 dpf when injected with the drug at the 1 to 4 cell stage (Yang et al., 2019). In humans, cases of pericardial effusion and pericarditis have been reported as a result of Aza treatment (Goo et al., 2019; Newman et al., 2016). In our tests, pericardial effusion as an oedema surrounding the heart was observed in 2 out of 12 of the Aza recipients at 3 dpi, but none of the recipients of PBS injections (Fig. S5). This could indicate that the heart of the zebrafish larvae responds to Aza in a similar manner as the human heart.

In this study we performed intravenous injections of DNR and Aza. Administration of drugs through the embryo water is a more frequently applied method, and while administration through water could give a much more predictable and stable drug concentration, it is not always known to which extent the different drugs are absorbed through the skin of the zebrafish. Moreover, Aza is highly unstable in aqueous solutions and for our purpose not a viable route of administration.

Conclusion

To be able to fully exploit the multitude of different data available from a high-content model like zebrafish, it is imperative with an analytical tool which efficiently process raw data into quantitative or qualitative measurement. Precise information on essential parameters

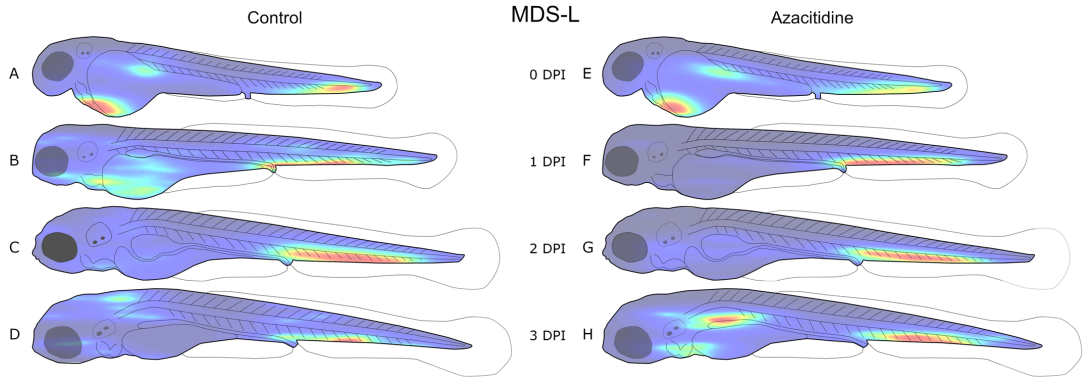

Fig. 4. Distribution of MDS-L cells in zebrafish larvae after intravenous injection with azacitidine. 4 nL of a 10 10^6 cells·ml^{-1} CellTracker™ Deep-Red-stained MDS-L cell suspension was injected into 18 zebrafish larvae at 2 dpf, and either left untreated (A-D, *n*=9) or treated with daily 4 nL injections of 1 mM azacitidine (E-H, *n*=9). Each larva was imaged daily using confocal microscopy, and the images analysed using our ImageJ plugin as described in the Materials and Methods section. The location of each cell above the volume threshold determined in Fig. 2D was used to create a combined distribution map for each group on each dpi. The density map was generated using MATLAB and visualises the areas of highest (red) and lowest (blue) cell density. Each density map is normalised to its own highest and lowest values; thus, it only visualises distribution, not total tumour burden. An illustration of the variation between replicates is given in Fig. S4C and D.

Biology Open (2022) 11, bio059530. doi:10.1242/bio.059530

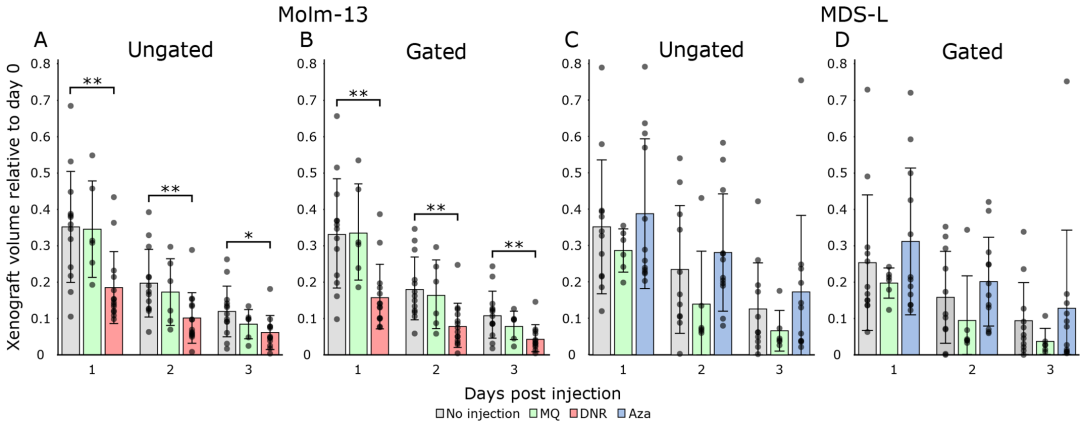

Fig. 5. Tumour burden of Molm-13 and MDS-L in zebrafish larvae with or without anti-cancer treatment. Molm-13 and MDS-L cells were stained with CellTracker™ Deep-Red and 4 nL of a 10 10^6 cells·ml^{-1} suspension engrafted into zebrafish larvae 2 dpf by injection into the posterior cardinal vein. Following engraftment, the larvae were imaged daily using spinning disk confocal microscopy. Treatment of Molm-13 cell-xenografted larvae consisted of a single 4 nL 1 mM daunorubicin injection at the day of the transplant, whereas MDS-L engrafted larvae were given daily injections of 4 nL 1 mM azacitidine. Control samples consisted of transplanted larvae without injection as well as larvae injected with 4 nL Milli-Q® water at the day of transplantation for Molm-13 and daily for MDS-L. Imaging and treatment were continued until the larvae reached 5 dpf. Using our software tool, fluorescent cells were counted and segmented based on the confocal images. The total volume of all segmented objects in larvae engrafted with Molm-13 and MDS-L are shown in A and C, respectively. Using the volume threshold of 1000 µm^3 determined from the images in Fig. 2C and D, the filtered total cell volume was determined (B and D). n=15 except for MQ-injected larvae, where n=6. Significance between injected larvae and non-injected controls were found using two-tailed Welch's t-test. Not annotated: P>0.05, *P≤0.05, **P≤0.01.

like total tumour burden, location of cancer cells, tumour development over time, and size and intensity of fluorescent objects, is needed to for instance evaluate the efficacy of a therapy, or to understand disease progression. Whereas previous analytical software programs are efficient with respect to automation and time, loss of data during processing occurs for instance in the process of image flattening. This can result in reduced ability to analyse single-cell parameters like size, intensity, or precise location. The software

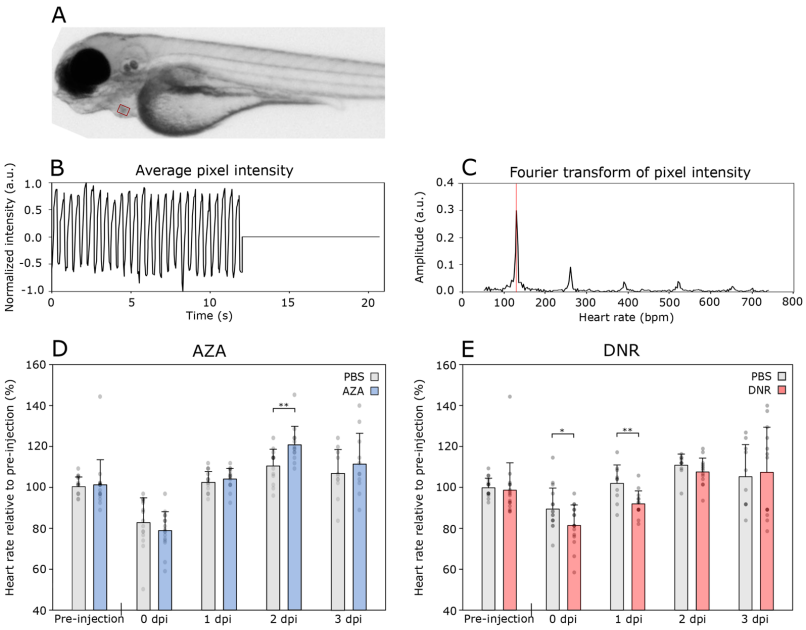

Fig. 6. Aza and DNR effects on zebrafish heart rate. The zebrafish larvae heart rate in the cardiotoxicity assays was found by filming the zebrafish for 12 s and using a self-written ImageJ macro to calculate the heart rate from the obtained video as described in the Materials and Methods section. (A) Still image from a film analysing zebrafish larvae heart rate. The red rectangle marking the region of interest (ROI) for pixel intensity measurement. (B) Average pixel intensity in the ROI. (C) Fourier transform of pixel intensity from the ROI to calculate beats per minute (BPM). (D) Heart rate of zebrafish larvae injected with 4 nL PBS (n=11) or Aza (1 mM, n=11). (E) Heart rate of zebrafish larvae injected with 4 nL PBS (n=10) or DNR (1 mM, n=13). For the Aza-test, the zebrafish larvae were injected daily after Pre-injection, 1 dpi and 2 dpi measurements. For the DNR-test, the zebrafish larvae were injected once, after the Pre-injection observation. The heart rate was related to the average heart rate of the control group pre-injection. Significance found using two-tailed Welch's t-test. Not annotated: P>0.05, *P≤0.05, **P≤0.01.

Biology Open (2022) 11, bio059530. doi:10.1242/bio.059530

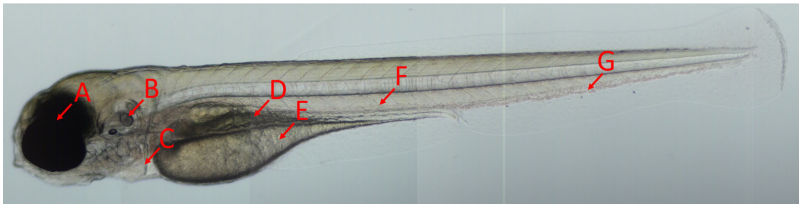

Fig. 7. Overview of the zebrafish larva. A zebrafish larva imaged at 4 dpf using bright field microscopy. The arrows indicate the eyes (A), otolith (B), heart (C), gut (D) and yolk sac (E). Intravenous injections were performed in the posterior cardinal vein (F) down-stream from the caudal vein (G).

tool presented in this paper performs automatic segmentation of fluorescent objects without losing information like size, volume, fluorescent intensity, or spatial distribution in the 3D space. While the software was designed for the analyses of leukaemia cells, it can readily be used to analyse other fluorescent objects, for instance zebrafish cells expressing fluorescent proteins or other xenografted cells. The software can also be adapted to analyse any confocal image stack containing fluorescent objects. Since there are only a few steps which require user interaction, namely setting the outline of the zebrafish larvae, and removing background fluorescence, the risk for subjectivity or user-generated errors in data analyses is also reduced. In the future, we envision that also definition of the larva outline and removal of background fluorescence can be automated as well. Then, the need for user interaction in data analyses is eliminated, which will further increase the efficiency and quality of data acquisition from confocal images.

MATERIALS AND METHODS

Materials

Microinjection pipettes for cell transplantation (VESbv-11-0-0-55) and microinjection pipettes for drug injection (VICbl-4-0-0-55), were from BioMedical Instruments (Zöllnitz, Germany). Daunorubicin (DNR, Cerubidine) was from Sanofi-Aventis (Paris, France). Azacitidine (Aza, A2385), RPMI-1640 Medium (R5886), Foetal bovine serum (FBS, F7524), L-glutamine (G7513), Penicillin-Streptomycin (P0781) were from Sigma-Aldrich (St. Louis, MO, USA). Ethyl 3-aminobenzoate methanesulfonate (Tricaine E10521) was from Merck Life Sciences (Darmstadt, Germany). Recombinant Human IL-3 Protein (IL-3, 203-IL-010) was from BioTechne (Minneapolis, MN, USA) and CellTracker™ Deep Red Dye (C34565) was from Thermo Fisher Scientific (Waltham, MA, USA).

Methods

Zebrafish maintenance

The transparent zebrafish (*Danio rerio*) line Casper was used (White et al., 2008). Fertilised zebrafish eggs were obtained from the zebrafish facility at the University of Bergen. This facility is run according to the European Convention for the Protection of Vertebrate Animals used for Experimental and Other Scientific Purposes. The zebrafish eggs, embryos and larvae were kept in Petri dishes with E3 medium (5 mM NaCl, 0.17 mM KCl and 0.33 mM $MgSO_4$) added methyl blue at 28.5°C. Petri dishes were cleaned daily by removing debris or dead embryos/larvae. After injection of cancer cells, the zebrafish larvae were kept at 31°C as a compromise between the 28.5°C preferred by the larvae and 37°C the injected cells. All zebrafish larvae were euthanised at 5 dpf. For euthanasia, the zebrafish larvae were first kept on ice for at least 20 min before being frozen at −20°C over-night.

Cell line maintenance

The AML cell line Molm-13 (Matsuo et al., 1997). and MDS cell line MDS-L (Rhyasen et al., 2014) were cultured at 37°C in a 5% CO_2 atmosphere in RPMI medium. The medium was enriched with 10% FBS, 20 mM L-glutamine, 100 IU ml^{-1} penicillin and 0.1 mg ml^{-1} streptomycin. For the MDS-L cells, the medium was additionally enriched with IL-3 to a concentration of 25 ng ml^{-1}. During maintenance, both cell lines were kept at a concentration between 100.000 and 1.000.000 cells·ml^{-1}.

In vivo cell experiments

Cell staining

The cells were stained using CellTracker™ Deep-Red Dye following the manufacturer's protocol. In brief, cells were centrifuged at 90 RCF for 5 min, the medium removed, and the cells resuspended in fresh serum free RPMI medium with 20 µM CellTracker™ staining solution. The cells were incubated with the CellTracker™ staining solution for 30 min at 37°C before being centrifuged at 90 RCF for 5 min and resuspended in fresh medium to a concentration of approximately 10 million cells·ml^{-1} for injection into zebrafish larvae.

Transplantation of human leukaemia cells in zebrafish larvae

Zebrafish larvae at 2 dpf in the long-pec stage according to the developmental stages proposed by Kimmel et.al., were anesthetised using a 0.7 mM tricaine solution and mechanically dechorionated under a microscope using forceps (Kimmel et al., 1995). A microinjection pipette with an inner diameter of 11 µm was filled with CellTracker™ Deep Red-stained cell suspension and mounted onto a Narishige MMN-5 with MMO-220A (Narashige, Tokyo, Japan) micromanipulator system and connected to an Eppendorf FemtoJet 4x microinjector (Eppendorf, Hamburg, Germany). The injection pressure and time were adjusted to achieve an injection volume of 4 nL. The anesthetised zebrafish larvae were placed on a 2% agarose bed and injected into the posterior cardinal vein as illustrated in Fig. 7. After injection, the zebrafish were kept under anaesthesia and transferred to 18 well chamber slides (µ-Slides, Ibidi, Gräfelfing, Germany). Imaging was performed on an Andor Dragonfly 505 confocal system (Andor Technology, Belfast, Northern Ireland) equipped with an inverted Nikon Ti-E microscope using a Nikon CFI Plan Apochromat lambda 10x objective (Nikon, Tokyo, Japan). The brightfield channel was used to visualise the larva, while a 700/38 nm band-pass filter with a 637 nm excitation laser was used to track the injected cancer cells.

After confocal imaging, half of the larvae were additionally injected into the posterior cardinal vein with an anti-cancer drug, using the same protocol as for cell injections apart from using an injection pipette with an inner diameter of 4 µm. DNR injections were only performed once on the same day as cell injections, while Aza was injected daily after each confocal imaging due to the molecule's short half-life in aqueous solutions. The dosage of DNR was chosen to be below that which could severely affect heart function, but still show significant activity in *in vitro* cell assays. For Aza-treatment of MDS-L transplanted larvae, we only could use the maximal tolerable dose, since the MDS-L cells are therapy-resistant. Transplanted larvae injected with the same volume of MQ were also imaged to find if injection itself affected cell growth.

The following days, the zebrafish larvae were imaged daily using confocal microscopy. Prior to reaching 120 h post-fertilization (5 dpf), all larvae were euthanised. The acquired confocal images were analysed using the self-written software tool.

Software tool for image processing

A plugin for the image processing software ImageJ (Version 1.53c; Schneider et al., 2012) was written in Java using JDK 1.8. The plugin was written using the integrated development environment Apache NetBeans IDE 13. A graphical overview of the software tool's workflow is given in Fig. 1A.

The software starts by flattening each confocal stack to a 2D representation. Importing the confocal image files is enabled using the

Bio-Formats library (Linkert et al., 2010). The brightfield channels are flattened by utilizing code from the Stack-Focuser plugin originally written by Michael Umorin, but slightly modified to suit our needs (https://imagej.nih.gov/ij/plugins/stack-focuser.html). Fluorescent channels are flattened using a max projection. Following flattening, the borders of the larvae are manually selected by the user. Using the selected outline, the angle of the larva is determined by the selection boundary's Feret angle, while position of the yolk sac is determined using a distance map by identifying the furthest internal point from the boundary. Using the position and orientation of each larva, a montage can automatically be created for each larva from the day of injection to the day of euthanasia.

For cell segmentation, the level of background fluorescence is determined manually by the user, as well as masking of any sources of high autofluorescence, such as iridophores, the gastrointestinal tract and yolk sac. Cell segmentation is performed using a watershed algorithm found in the mcib3d library, with the code slightly modified to increase segmentation speed in our application (Ollion et al., 2013). To find starting points for the watershed algorithm, the fluorescent stack is first pre-processed using a 3D-median filter with radius 3 for x and y, and 2 for z. This is followed by a local maximum filter with a cut-off value of the predetermined background fluorescence. Using the obtained seed image as a starting point, a watershed is performed on the fluorescent stack. This process is repeated for each larva for each daily acquisition, and the detected objects stored.

Following cell segmentation, a size distribution of each detected object is created. From this distribution, a size range for viable cells is determined. Using this size range as a filter, the cell count and total cell volume in each larva is exported for further analysis.

From the location-data obtained from the segmentation process, a heatmap is constructed to visualise cell distributions. X- and Y-coordinates of segmented cells for all larva within the same group and day are combined and a heatmap generated using MATLAB (R2021 Update 2) with a modified version of the Data Density Plot plugin supplied by Malcolm McLean (https://www.mathworks.com/matlabcentral/fileexchange/31726-data-density-plot). All heatmaps are normalised to facilitate the visualization of the cell distribution.

Cardiotoxic assay

2 dpf zebrafish larvae were intravenously injected with the drugs. To ensure that the effect of temperature and tricaine was similar in all larvae, the zebrafish larvae were exposed to 0.7 mM tricaine and left in room temperature for at least 30 min prior to recording heart rate. The zebrafish larvae then were injected with either of the following into the PCV: 4 nL DNR (1 mM), Aza (1 mM) or PBS as control. Due to the rapid decomposition of Aza, the injection of this drug and PBS for the representative control group was repeated at three and four dpf. DNR and its PBS control group was only injected at 2 dpf.

To determine heart rate, each larva was filmed for 12 s using a Leica M205 stereo microscope fitted with Leica DFC3000 G camera and the Leica Application Suite X software. At 2 dpf, the zebrafish larvae were filmed both before (Pre-injection) and directly after (0 dpi) the injection. This was to observe whether there were immediate toxic effects of the drugs. For simplicity, the time points are related to the first injection for all groups.

The heart rate was found using a self-written macro for ImageJ. To determine the heart rate, a region around the heart is selected (Fig. 6A). The macro measures the average intensity in each frame of the video and normalises the values to a range between -1 and 1. To comply with the requirements of the fast Fourier transform (FFT) algorithm utilised by ImageJ, artificial measurements with the value zero are added to the measurement list until the total number of measurements equals a power of two (Fig. 6B). After performing the FFT, the heart rate is determined to be the fundamental frequency of the plot (Fig. 6C).

Statistical analyses

The data in all bar charts is presented as average with standard deviation. Statistical significance between groups was determined using a two-tailed Welch's *t*-test performed using RStudio for Windows, version 2022.02.2 Build 485 (RStudio, PCB, Boston, MA, USA).

Acknowledgements

We thank the Molecular Imaging Centre (MIC) at the University of Bergen for support and training on confocal microscopy, as well as the zebrafish facility at the University of Bergen for access to E3 medium and mature zebrafish for breeding.

Competing interests

The authors declare no competing or financial interests.

Author contributions

Conceptualization: J.-L.F., L.H.; Methodology: J.-L.F.; Software: J.-L.F.; Validation: J.-L.F., I.N.R.; Formal analysis: J.-L.F., I.N.R.; Investigation: J.-L.F.; Resources: K.E.F., A.O.K.; Writing - original draft: J.-L.F., I.N.R., L.H.; Writing - review & editing: I.N.R., K.E.F., A.O.K., L.H.; Visualization: J.-L.F., I.N.R.; Supervision: A.O.K., L.H.; Project administration: L.H.; Funding acquisition: K.E.F., A.O.K., L.H.

Funding

This project was funded by the Western Norway Health Authorities (grant no.: F-12533) and Nordforsk (the NordForsk Nordic Center of Excellence "NordAqua") (grant no.: 82845), Astri og Edvard Riisøens legat, and the Norwegian Society for Children's Cancer (grant nos: 180007 and 190004). Open Access funding provided by University of Bergen: Universitetet i Bergen. Deposited in PMC for immediate release.

Data availability

The following software was used in this research:

ImageJ (Version 1.53c, (Schneider et al., 2012)) can be obtained from https://imagej.nih.gov/ij/.

The Bio-Formats library (Linkert et al., 2010) can be obtained from https://github.com/ome/bioformats.

The Stack-Focuser plugin for ImageJ can be obtained from https://imagej.nih.gov/ij/plugins/stack-focuser.html.

The mcib3d library (Ollion et al., 2013) can be obtained from https://github.com/mcib3d/mcib3d-core

MATLAB (R2021 Update 2) can be obtained from https://se.mathworks.com/products/matlab.html.

The data density plot plugin for MATLAB can be obtained from https://www.mathworks.com/matlabcentral/fileexchange/31726-data-density-plot.

RStudio for Windows, version 2022.02.2 Build 485 can be obtained from https://www.rstudio.com/products/rstudio/.

The software tool presented in this publication is available as an ImageJ java-plugin at https://zenodo.org/10.5281/zenodo.7383160 and source code at https://github.com/Jfo004/ConfocalCellSegmentation.

References

Carreira, M. J., Vila-Blanco, N., Cabezas-Sainz, P. and Sánchez, L. (2021). ZFTool: a software for automatic quantification of cancer cell mass evolution in Zebrafish. *Applied Sciences* **11**, 7721. doi:10.3390/app11167721

Cazzola, M. (2020). Myelodysplastic Syndromes. *N Engl. J. Med.* **383**, 1358-1374. doi:10.1056/NEJMra1904794

Döhner, H., Weisdorf, D. J. and Bloomfield, C. D. (2015). Acute Myeloid Leukemia. *N Engl. J. Med.* **373**, 1136-1152. doi:10.1056/NEJMra1406184

Fenaux, P., Mufti, G. J., Hellstrom-Lindberg, E., Santini, V., Finelli, C., Giagounidis, A., Schoch, R., Gattermann, N., Sanz, G., List, A. et al. (2009). Efficacy of azacitidine compared with that of conventional care regimens in the treatment of higher-risk myelodysplastic syndromes: a randomised, open-label, phase III study. *Lancet Oncol.* **10**, 223-232. doi:10.1016/S1470-2045(09)70003-8

Goo, K., Uy, R. and Roswarski, J. (2019). Azacitidine-associated pleuropericardial effusion in myelodysplastic syndrome: A case report. *J. Oncol. Pharm. Pract.* **25**, 1248-1252. doi:10.1177/1078155218784762

Gore, A. V., Pillay, L. M., Venero Galanternik, M. and Weinstein, B. M. (2018). The zebrafish: A fintastic model for hematopoietic development and disease. *Wiley Interdiscip. Rev. Dev. Biol.* **7**, e312. doi:10.1002/wdev.312

Han, Y., Zhang, J., Qian, J. and Hu, C. (2015). Cardiotoxicity evaluation of anthracyclines in zebrafish (Danio rerio). *J. Appl. Toxicol.* **35**, 241-252. doi:10.1002/jat.3007

Kimmel, C. B., Ballard, W. W., Kimmel, S. R., Ullmann, B. and Schilling, T. F. (1995). Stages of embryonic development of the zebrafish. *Dev. Dyn.* **203**, 253-310. doi:10.1002/aja.1002030302

Linkert, M., Rueden, C. T., Allan, C., Burel, J.-M., Moore, W., Patterson, A., Loranger, B., Moore, J., Neves, C., Macdonald, D. et al. (2010). Metadata matters: access to image data in the real world. *J. Cell Biol.* **189**, 777-782. doi:10.1083/jcb.201004104

Liu, H. (2021). Emerging agents and regimens for AML. *J. Hematol. Oncol.* **14**, 49. doi:10.1186/s13045-021-01062-w

Maciag, M., Wnorowski, A., Mierzejewska, M. and Plazinska, A. (2022). Pharmacological assessment of zebrafish-based cardiotoxicity models. *Biomed. Pharmacother.* **148**, 112695. doi:10.1016/j.biopha.2022.112695

Matsuo, Y., MacLeod, R. A., Uphoff, C. C., Drexler, H. G., Nishizaki, C., Katayama, Y., Kimura, G., Fujii, N., Omoto, E., Harada, M. et al. (1997). Two acute monocytic leukemia (AML-M5a) cell lines (MOLM-13 and MOLM-14) with interclonal phenotypic heterogeneity showing MLL-AF9 fusion resulting from an occult chromosome insertion, ins(11;9)(q23;p22p23). *Leukemia* **11**, 1469-1477. doi:10.1038/sj.leu.2400768

Mikut, R., Dickmeis, T., Driever, W., Geurts, P., Hamprecht, F. A., Kausler, B. X., Ledesma-Carbayo, M. J., Marée, R., Mikula, K., Pantazis, P. et al. (2013). Automated processing of zebrafish imaging data: a survey. *Zebrafish* **10**, 401-421. doi:10.1089/zeb.2013.0886

Molina, B., Chavez, J. and Grainger, S. (2021). Zebrafish models of acute leukemias: current models and future directions. *Wiley Interdiscip. Rev. Dev. Biol.* **10**, e400. doi:10.1002/wdev.400

Newman, M., Malla, M. and Gojo, I. (2016). Azacitidine-induced pericarditis: a case series. *Pharmacotherapy* **36**, 443-448. doi:10.1002/phar.1733

Ollion, J., Cochennec, J., Loll, F., Escudé, C. and Boudier, T. (2013). TANGO: a generic tool for high-throughput 3D image analysis for studying nuclear organization. *Bioinformatics (Oxford. England* **29**, 1840-1841. doi:10.1093/bioinformatics/btt276

Paik, E. J. and Zon, L. I. (2010). Hematopoietic development in the zebrafish. *Int. J. Dev. Biol.* **54**, 1127-1137. doi:10.1387/ijdb.093042ep

Poss, K. D., Wilson, L. G. and Keating, M. T. (2002). Heart regeneration in zebrafish. *Science (New York, N.Y.)* **298**, 2188-2190. doi:10.1126/science.1077857

Rhyasen, G. W., Wunderlich, M., Tohyama, K., Garcia-Manero, G., Mulloy, J. C. and Starczynowski, D. T. (2014). An MDS xenograft model utilizing a patient-derived cell line. *Leukemia* **28**, 1142-1145. doi:10.1038/leu.2013.372

Saygin, C. and Carraway, H. E. (2021). Current and emerging strategies for management of myelodysplastic syndromes. *Blood Rev.* **48**, 100791. doi:10.1016/j.blre.2020.100791

Schneider, C. A., Rasband, W. S. and Eliceiri, K. W. (2012). NIH Image to ImageJ: 25 years of image analysis. *Nat. Methods* **9**, 671-675. doi:10.1038/nmeth.2089

Siolas, D. and Hannon, G. J. (2013). Patient-derived tumor xenografts: transforming clinical samples into mouse models. *Cancer Res.* **73**, 5315-5319. doi:10.1158/0008-5472.CAN-13-1069

Sullivan, C., Matty, M. A., Jurczyszak, D., Gabor, K. A., Millard, P. J., Tobin, D. M. and Kim, C. H. (2017). Chapter 4 - Infectious disease models in zebrafish. In *Methods in Cell Biology: The Zebrafish* (ed. H. W. Detrich, M. Westerfield and L. I. Zon), pp. 101-136: Academic Press.

White, R. M., Sessa, A., Burke, C., Bowman, T., LeBlanc, J., Ceol, C., Bourque, C., Dovey, M., Goessling, W., Burns, C. E. et al. (2008). Transparent adult zebrafish as a tool for in vivo transplantation analysis. *Cell Stem Cell* **2**, 183-189. doi:10.1016/j.stem.2007.11.002

Yamamoto, D., Sato, D., Nakayama, H., Nakagawa, Y. and Shimada, Y. (2019). ZF-Mapper: simple and complete freeware for fluorescence quantification in zebrafish images. *Zebrafish* **16**, 233-239. doi:10.1089/zeb.2018.1683

Yang, Q., Wu, F., Wang, F., Cai, K., Zhang, Y., Sun, Q., Zhao, X., Gui, Y. and Li, Q. (2019). Impact of DNA methyltransferase inhibitor 5-azacytidine on cardiac development of zebrafish in vivo and cardiomyocyte proliferation, apoptosis, and the homeostasis of gene expression in vitro. *J. Cell. Biochem.* **120**, 17459-17471. doi:10.1002/jcb.29010

Zhu, J.-J., Xu, Y.-Q., He, J.-H., Yu, H.-P., Huang, C.-J., Gao, J.-M., Dong, Q.-X., Xuan, Y.-X. and Li, C.-Q. (2014). Human cardiotoxic drugs delivered by soaking and microinjection induce cardiovascular toxicity in zebrafish. *J. Appl. Toxicol.* **34**, 139-148. doi:10.1002/jat.2843

The RAC1-inhibitor EHop-016 attenuates AML cell migration and enhances the efficacy of daunorubicin in MOLM-13 transplanted zebrafish larvae

Anette Lodvir Hemsing*[a,b], anette.hemsing@uib.no

Jan-Lukas Førde*[a,c], jan-lukas.forde@uib.no

Håkon Reikvam[a,b], hakon.reikvam@uib.no

Lars Herfindal[c], lars.herfindal@uib.no

[a] Department of Medicine, Haukeland University Hospital, pb 1400, 5021 Bergen, Norway

[b] Department of Clinical Science, University of Bergen, Jonas Lies vei 87, 5021 Bergen, Norway

[c]Centre for Pharmacy, Department of Clinical Science, University of Bergen, 5021 Bergen Norway

* The authors contributed equally

Corresponding author: Professor Lars Herfindal, Department of Clinical Science, Jonas Lies vei 87, 5021 Bergen, Norway. E-mail address: lars.herfindal@uib.no

Keywords: AML; Rac1; zebrafish larvae; cell migration; homing; therapy

Abstract

Ras-related C3 botulinum toxin substrate 1 (Rac1) is a GTPase implicated in cell migration and homing of hematopoietic cells to the hematopoietic niche, commonly overexpressed in acute myeloid leukemia (AML). This can lead to quiescence of leukemic blasts in the niche and reduced response to therapy. We investigated the Rac1 inhibitor EHop-016 on AML by assessing its effects on MOLM-13 cells *in vitro* and in zebrafish larvae, regarding cell motility and therapeutic potential in combination with daunorubicin (DNR). *In vitro* assessment of proliferation and viability was by measurement of ^{3}H-thymidine incorporation and detection of Annexin V/PI positive cells. Cell motility was evaluated by measurement of migration in a transwell system. Fluorescently stained MOLM-13 cells were injected into zebrafish larvae, and individual cells followed by confocal microscopy. Cell accumulation in the caudal hematopoietic tissue (CHT) was studied using a 12-hour timelapse, while *in vivo* efficacy of DNR, EHop-016 or a combination was investigated over 24 h.

The *in vitro* results showed that EHop-016 acted synergistically in combination with DNR in reducing the viability of MOLM-13 cells (Bliss synergy score above 10%). Non-toxic concentrations of EHop-016 reduced cell migration. These findings were reproduced in zebrafish larvae: larvae receiving both DNR and EHop-016 had significantly reduced tumor burden compared to the untreated control or single treatments. The accumulation of MOLM-13 cells in the CHT was reduced in larvae receiving EHop-016 treatment.

Our findings demonstrate that targeting Rac1 in AML holds promise as a complementary treatment to established chemotherapy and should be further investigated.

Abbreviations

AML – Acute myeloid leukemia

CHT – Caudal hematopoietic tissue

DNR – Daunorubicin

dpf – Days post fertilization

FBS – Fetal bovine serum

LSC – leukemic stem cells

LSD – Least significant difference

MTD – Maximum tolerable dose

PBS – phosphate-buffered saline

Rac1 – GTPase Ras-related C3 botulinum toxin substrate 1

Introduction

Acute myeloid leukemia (AML) is a blood- and bone-marrow cancer characterized by the clonal expansion of immature myeloid cells. The standard chemotherapy regimen of seven days of cytarabine and three days of daunorubicin (DNR) was developed more than 50 years ago and has since then undergone only minor changes (Lichtman 2013). About half of AML patients still relapse within five years of diagnosis (Bertoli et al. 2017). Relapsed AML and high age are associated with poor prognosis, where long-lasting curative outcome is an exception. In the last decade, molecular therapies targeting specific aberrant proteins in AML cells like FLT3, BCL-2, and IDH1/2 have been developed and implemented as additions to traditional chemotherapy or hypomethylating agents. However, some patients fail to respond to these therapies, for instance, because their leukemic blasts harbor no druggable target proteins or develop resistance after treatment (Garitano-Trojaola et al. 2021; Yao et al. 2022).

The GTPase Ras-related C3 botulinum toxin substrate 1 (Rac1) is identified as a possible novel target for AML therapy (Garitano-Trojaola et al. 2021). This protein is commonly overexpressed in AML by upstream activation, such as from growth factors or via constitutively active mutated FLT3 (Wang et al. 2009). Commonly, Rac1 is involved in the homing and engraftment of hematopoietic cells to the bone marrow niche downstream of the activated membrane receptors CXCR4 and CD44 (Cancelas et al. 2006; Turley et al. 2002). Accordingly, Wang et al. demonstrated reduced homing to and interaction with the bone marrow niche in the AML cell line KG1-a with an induced dominant negative variant of Rac1, and furthermore, a reduced fraction of cells in a quiescent state. It has been shown that the transition of cells from a quiescent state to an active state renders them more vulnerable to chemotherapy (Wang et al. 2013). Wu and colleagues found improved efficacy of anthracyclines when Rac1 was silenced with shRNA in a mouse model of AML (Wu et al. 2019). Garitano-Trojaola et al. showed that overexpression of Rac1 altered the cytoskeletal organization of AML cells, the adhesion to surrounding cells, and induced the expression of the anti-apoptotic protein BCL-2. Combined FLT3-, BCL-2-, and Rac1 inhibition could re-establish drug sensitivity in a midostaurin (FLT3 inhibitor)-resistant MOLM-13 AML cell line (Garitano-Trojaola et al. 2021).

Transient inhibition of Rac1 with the first-generation inhibitor NSC23766 was investigated by Cancelas et al. using a single intraperitoneal dose in a non-cancer C57BL/6 mouse model. This induced a doubling of hematopoietic stem cells and progenitors in the peripheral blood after six hours, returning to baseline values 24 hours after treatment (Cancelas et al. 2005). The second-generation Rac1 inhibitor EHop-016 is more potent and has demonstrated antiproliferative and proapoptotic effects in the low micromolar range on patient-derived AML cells (Hemsing et al. 2022). It was reported as a synthesized derivate from NSC23766 in 2012. Also, it reduced directed cell migration in a breast cancer cell line at a concentration that did not affect the cell viability (Montalvo-Ortiz et al. 2012). Ehop-016 is more selective towards Rac1 than Eht1864, used by Garitano-Trojaola and colleagues to study migration of cancer cells (Shutes et al. 2007). Having established that Rac1 is an interesting target in AML, we wanted to investigate if Rac1 inhibition with EHop-016 could affect cell migration *in vitro* and the homing of AML cells to the hematopoietic niche *in vivo*. Furthermore, we wanted to investigate if combining Rac1-inhibition with DNR could give a synergistic anti-AML response.

Our investigations of leukemic cell migration were undertaken on the human AML cell line MOLM-13, which harbors an *FLT3*-ITD mutation, and using zebrafish larvae as a model system. The zebrafish (Danio rerio) has emerged as a useful and relevant tool for drug development and toxicity studies in cancer research.

Compared to mammalian models, zebrafish have high fecundity, low cost, and easy maintenance, and their small size and transparency during the embryo and larval stage allow for *in vivo* single-cell studies using confocal microscopy (Førde et al. 2022). In the early stages of development, from two days post fertilization (dpf) to five dpf, the caudal hematopoietic tissue (CHT) located in the ventral tail region is the main site of hematopoiesis. This is then gradually replaced by the thymus and caudal parts of the kidneys from three and four dpf, respectively (Gore et al. 2018). Zebrafish have genetics compared to humans, with approximately 70% of human genes having at least one orthologue in zebrafish (Choi et al. 2021). Important for our research, Tulotta et al. have demonstrated cross-communication between human CXCR4 and zebrafish CXCL12 (ligand of CXCR4) in zebrafish xenografts (Tulotta et al. 2016).

Method and materials

Materials

The MOLM-13 cell line (DSMZ.no ACC 554, (Matsuo et al. 1997)) was obtained from the German Collection of Microorganisms and Cell Cultures GmbH (Braunschweig, Germany). After acquisition of the cells, they were verified, and frozen in aliquots. The cells were defrosted from these verified batches regularly. Tricaine (cat.no: E10521), RPMI 1640 (cat.no: R5886), penicillin-streptomycin (cat.no: P0781 and P4458), L-glutamine (cat.no: G7513), dimethyl sulfoxide (DMSO) (cat.no: D2650), and fetal bovine serum (FBS) (cat.no: F7524 and S181B-500) were purchased from Merck KgaA (Darmstadt, Germany) and VWR (Radnor, PA, USA). Human CXCL12 (cat.no: 300-28A) was purchased from PeproTech Inc (Cranbury, NJ, USA). Flat-bottomed 96- and 24-well plates were from VWR (Radnor, PA, USA), µ-Slide 18-well confocal chamber slides from Ibidi (Gräfelfing, Germany), and transwell inserts with 8 µm pore size from Corning (Glendale, AZ, USA). The ^{3}H-thymidine incorporation proliferation assay (cat.no: NET027A) was purchased from PerkinElmer Inc (Waltham, MA, USA), and the Annexin V/Propidium Iodide (PI) assay (cat.no: 640928) from Nordic BioSite (Täby, Sweden). For cell injections, micropipettes with a 13 µM inner diameter (cat.no: VESbv-13-0-0-55) were purchased from BioMedical Instruments (Zöllnitz, Germany). The cell staining kit CellTracker™ Deep Red Dye (cat.no C34565) was purchased from ThermoFisher Scientific (MA, USA).

EHop-016 (N4-(9-Ethyl-9H-carbazol-3-yl)-N2-(3-morpholin-4-yl propyl)-pyrimidine-2,4-diamine) was purchased from Merck KGaA (Darmstadt, Germany) and dissolved in DMSO to a stock concentration of 20 mM (8.6 mg/ml). DNR (Cerubidin®) from Sanofi (Paris, France) was dissolved in milli-Q water from Merck KGaA (Darmstadt, Germany) to a concentration of 8.87 mM (5 mg/ml). Stock solutions of the drugs were stored at -80 °C. The compounds were defrosted and diluted in RPMI 1640, phosphate-buffered saline (PBS), or E3 zebrafish medium on the day of the experiments.

Cell maintenance and experimental conditions

Cell maintenance

The human AML MOLM-13 cell line was cultured at 37 °C with 5% CO_2 in RPMI 1640 medium supplemented with 10% FBS, 50 IU/ml penicillin, 50 µg/ml streptomycin, and 0.2 mM L-glutamine. Routine testing for Mycoplasma infection was performed using a MycoAlert™ mycoplasma detection kit (cat.no: LT07-418, Lonza, Basel, Switzerland). No infection was detected during this study. The culture conditions during experiments were identical unless otherwise specified.

Proliferation assay

The ^{3}H-thymidine proliferation assay was carried out in a flat-bottomed 96-well plate with 20 000 MOLM-13 cells per well. Vehicle control RPMI 1640, EHop-016, and/or DNR were added to a final 200 µl cell suspension volume in RPMI 1640 with 10% FBS. The plates were incubated for 48 h before adding 20 µl (1 µCi) ^{3}H-thymidine per well. After six h incubation, the plates were harvested, and nuclear incorporation was determined by liquid scintillation counting. Each experiment was performed in triplicate, and relative proliferation compared to untreated controls was calculated from the medians (Stapnes et al. 2007).

Flow cytometric detection of apoptotic cells

The Annexin V/PI assay was conducted to detect and quantify apoptosis. MOLM-13 cells suspended in culture media were seeded in flat-bottomed 24-well plates at 5.0 x 10^{5} cells/ml and added with vehicle control (RPMI 1640) or increasing concentrations of either EHop-016, DNR or a combination of both. The cells were incubated for 48 h before being harvested, placed on ice, and washed twice with 4 °C PBS. The cells were double stained with Annexin V and PI according to the manufacturer's protocol before data acquisition on a FACSVerse™ flow cytometer (BD Biosciences, San Jose, Ca, USA). A total of 20 000 events were collected per sample. Flow cytometry data were handled in FlowJo v10.8.1 (BD, Ashland, OR, USA); data analysis included gating to remove debris and doublets and adjusting for autofluorescence of DNR using the AutoSpill function.

Measurement of MOLM-13 cell migration

MOLM-13 cells were seeded in a flat-bottomed 24-well plate at 1.0 x 10^{6} cells/ml. Vehicle control RPMI 1640 or EHop-016 was added to a final concentration of 6 µM or 8 µM in RPMI 1640 medium supplemented with 0.5% FBS. The plate was incubated for 20 h. The cells were then harvested, centrifuged at 200 rcf for 5 min, and resuspended in RPMI 1640 without FBS. The viability was determined by counting the fraction of cells excluding trypan blue using a hemacytometer. The migration assay was performed in 24-well plates fitted with transwell inserts with 8 µm pore size. The upper compartment was loaded with 2.0 x 10^{5} viable cells in 200 µl RPMI 1640 without FBS. The lower compartment contained 600 µl of RPMI 1640 with either 10% FBS or 100 ng/ml CXCL12. After six h of incubation, the cells in the lower well were collected by centrifugation, resuspended in 100 µl 0.9% NaCl and counted with trypan blue exclusion. To ensure that reduced cell count in the acceptor well was not due to cell death from the treatments, the cells were resuspended in RPMI with 10% FBS without EHop-016 and cultured for 48h before a new assessment of viability.

Zebrafish larva handling and experimental conditions

Zebrafish larva handling

The zebrafish (Danio rerio) line Casper was used in this project (White et al. 2008). Adult zebrafish were kept at, and fertilized zebrafish eggs obtained from, the zebrafish facility at the Department of Bioscience, University of Bergen. This facility is run according to the European Convention for the Protection of Vertebrate Animals used for Experimental and Other Scientific Purposes. The experiments on larvae were terminated at five days post fertilization, and thus do not require approval from the Norwegian Food Safety Authorities. Fertilized zebrafish eggs were incubated at 28.5 °C in E3 medium (5 mM NaCl, 0.17 mM KCl, 0.33 mM $MgSO_4$, and 10 µM methyl blue as antifungal agent). Debris and dead larvae were removed daily. Between 24 h to 48 h post-fertilization, zebrafish larvae were dechorionated using forceps. During experiments with transplanted human cancer cells, the incubation temperature was raised to 31 °C. The zebrafish larvae were euthanized when reaching five dpf by cooling on ice for at least 30 min before being frozen at -20 °C overnight.

While the developing zebrafish is termed embryo prior to the protruding-mouth stage at 72 h post fertilization (Kimmel et al. 1995), for simplicity and to avoid confusion, zebrafish in all stages are called larva in this publication.

Transplantation of MOLM-13 cells by intravenous injection

Prior to injection, MOLM-13 cells were stained with CellTracker™ Deep Red according to the manufacturer's protocol. In brief, cells were centrifuged at 130 rcf for 5 min and resuspended in RPMI 1640 medium without FBS. The cell tracker staining solution was added to a final concentration of 20 µM, and the cells were incubated at 37 °C in a 5% CO_2 atmosphere for 30 min. Next, the cells were centrifuged and resuspended in RPMI 1640 medium with 10% FBS. Cell suspensions of 1.0 x 10^7 cells/ml in RPMI 1640 medium were injected using glass micropipettes with a beveled tip and inner diameter of 13 µm. The micropipettes were mounted in an injection setup with an MMO-220A micromanipulator system (Narashige, Tokyo, Japan), Eppendorf FemtoJet 4x microinjector (Eppendorf, Hamburg, Germany), and Leica M205 stereo microscope (Leica, Wetzlar, Germany). Injection pressure and time were adjusted to result in an injection droplet with a 200 µm diameter (approximately 4 nl) in peanut oil. Dechorionated zebrafish larvae were anesthetized using an E3 medium containing 0.7 mM tricaine before injection. The anesthetized zebrafish larvae were placed on 2% agarose beds and injected into the posterior cardinal vein (PCV) (Figure 3A, red arrow). Micropipettes for drug and PBS injections were self-drawn using a P-1000 micropipette Puller from Sutter Instrument (Novato, CA, US).

Toxicity assay of EHop-016 in zebrafish larvae

Two administration routes were tested to establish toxicity: intravenous injection and the addition of drugs in the E3 medium. For injections, zebrafish larvae at two dpf in the long pec stage (Kimmel et al. 1995) were injected intravenously with EHop-016 dilutions (10 µM or 100 µM in Milli-Q water) or Milli-Q water following the injection method described earlier in the method section. For in-water exposure, a dilution series of EHop-016 in E3 medium was created in a 96-well plate. One dechorionated zebrafish larva in the long pec stage was placed in each well. Visual toxic effects were assessed daily using microscopy, with abnormalities in the cardiovascular system (such as pericardial oedema, affections in heart-rate blood flow) and other visual abnormalities (such as developmental defects) being investigated.

To visualize blood flow, the larvae were sedated, and videos recorded under a microscope. The image series was filtered using a 3x3 median filter to reduce noise and new images were generated by calculating the standard deviation in pixel intensity across each time frame. Areas with high standard deviation indicate movement in the image along time frames. The standard deviation image was then overlayed on a still frame of the original image series and colored red. Image processing was performed in FIJI v. 2.14.0 (Schindelin et al. 2012).

Cell migration timelapse

The biodistribution of MOLM-13 cells in zebrafish larvae was investigated using a 12-hour timelapse. Dechorionated zebrafish larvae at one dpf in the pharyngula period (Kimmel et al. 1995) were incubated overnight in E3 medium with or without 20 µM EHop-016 in-water. The following day, CellTracker™ Deep Red stained MOLM-13 cells were injected into the PCV. Immediately following injection, the zebrafish larvae were placed in confocal chamber slides containing E3 medium with or without 20 µM EHop-016. Imaging was performed using an Andor Dragonfly 505 confocal system (Andor Technology, Belfast, Northern Ireland) equipped with an inverted Nikon Ti-E microscope with a Nikon CFI Plan Apochromat lambda 10x objective (Nikon, Tokyo, Japan). Imaging of the fluorescent cancer cells was performed using a 637 nm excitation laser and 700/38 nm band-pass filter. The timelapse was performed over 12 h, with image acquisition every 10 min.

The number of MOLM-13 cells in the CHT was counted in a 724 µm x 121 µm (600 pix x 100 pix) bounding box positioned at the posterior end of the yolk sac and aligned with the ventral side of the notochord as shown in Figure 3A (red box) at 0 h, three h, six h, and 12 h following the start of the timelapse.

In vivo EHop-016 efficacy assay

Zebrafish larvae were dechorionated at one dpf and the EHop-016 group pre-incubated overnight with 20 µM EHop-016 in E3 medium. The same day, MOLM-13 cells were stained with CellTracker™ Deep Red and further incubated in RPMI 1640 medium with 10% FBS with or without 5 µM EHop-016. The following day, the prepared cells were injected into the zebrafish larva PCV. The EHop-016 group and combination group received cells pre-treated with EHop-016. The larvae were then imaged by confocal microscopy and injected with 4 nl 1 mM DNR or PBS into the PCV.

The zebrafish larvae were imaged using the same setup used for time-lapse imaging. The obtained confocal images were processed using an ImageJ plugin for batch-processing of cell segmentation(Førde et al. 2022), followed by statistical analysis.

Data analysis

Statistical analyses were performed in GraphPad Prism v. 9.5.1 (GraphPad Software, San Diego, CA, USA) and SPSS v. 27 (IBM Corp. Armonk, NY, USA). The half-maximal effective concentration (EC_{50}) values were calculated from dose-response experiments using non-linear regression analysis. A two-way ANOVA with Fisher's Least Significant Difference (LSD) test was used to compare treatment groups for the *in vitro* cell migration data and the *in vivo* experiments. Paired t-tests were used to compare paired data before and after treatment. *P*-values < 0.05 were considered statistically significant.

The efficacy of the drugs and their combinations by the Annexin V/PI assay was determined by studying the combined percentages of apoptotic and necrotic cells in each sample, termed inhibition. Following analysis, the results for each sample were corrected with a weighted baseline correction calculated with the following formula:

$$I_{corrected} = I_{measured} - I_{baseline} * \frac{100 - I_{measured}}{100 - I_{baseline}}$$

Where $I_{corrected}$ is the inhibition after baseline correction, $I_{measured}$ the measured inhibition, and $I_{baseline}$ the average of the untreated controls.

The synergy score for cell experiments was determined by subtracting a calculated inhibition from the measured inhibition for each combination. The Bliss method was used to calculate a theoretical inhibition for each combination (Bliss 1939). These calculations were performed using the web resource SynergyFinder Plus (Zheng et al. 2022). A score between -10 and 10% indicates an additive effect, below -10% an antagonistic effect, and above 10% a synergistic effect.

Results

Effects of EHop-016 on MOLM-13 proliferation, viability and migration in vitro

The ^{3}H-thymidine assay demonstrated that EHop-016 had an antiproliferative effect on MOLM-13 cells after 48 h incubation with an EC_{50} of 6.1 µM (95% confidence interval (CI) 5.9-6.4 µM) (Figure 1A). To identify whether the reduced ^{3}H-thymidine incorporation could be due to cell death, we investigated the viability and amount of apoptosis in cells treated with EHop-016 using the Annexin V/PI assay. EHop-016 reduced the number of viable MOLM-13 cells with an EC_{50} of 11.3 µM after 48 h incubation (data not shown).

Next, MOLM-13 cells were treated with EHop-016 in combination with DNR for 48 h to reveal synergistic effects. The baseline corrected results of the apoptosis assay are shown in Figure 1C and are the average of two replicates for each combination. The Bliss synergy score shown in Figure 1D was calculated using these values. For the combinations including 7.5 µM EHop-016 or 10 nM DNR a synergy score within the range of ±10% was observed, indicating an additive interaction at these concentrations. At higher concentrations of both drugs, except for the 50 nM DNR and 10 µM EHop-016 combination, the score was higher than 10% indicating a synergistic interaction.

Since Rac1 is involved in hematopoietic cell migration, we next investigated to which extent EHop-016 affected the migration of MOLM-13 cells using FBS or CXCL12 as chemoattractants. Untreated cells preferred 10% FBS and CXCL12 to RPMI without attractants (fold change > 1.5). Pretreatment for 20 h with 8 µM EHop-016 reduced the migration toward both chemoattractants compared with their untreated controls ($p < 0.001$ towards 10% FSB and $p < 0.001$ towards CXCL12, two-way ANOVA with Fisher's LSD test) and compared with 6 µM treatment ($p = 0.003$ towards 10% FBS and $p < 0.001$ towards CXCL12) (Figure 1E). To assess the viability of the treated cells, they were washed and resuspended in RPMI with 10% FBS without EHop-016 for 48 h. The fraction of viable cells was not affected by EHop-016 compared to untreated control cells (data not shown).

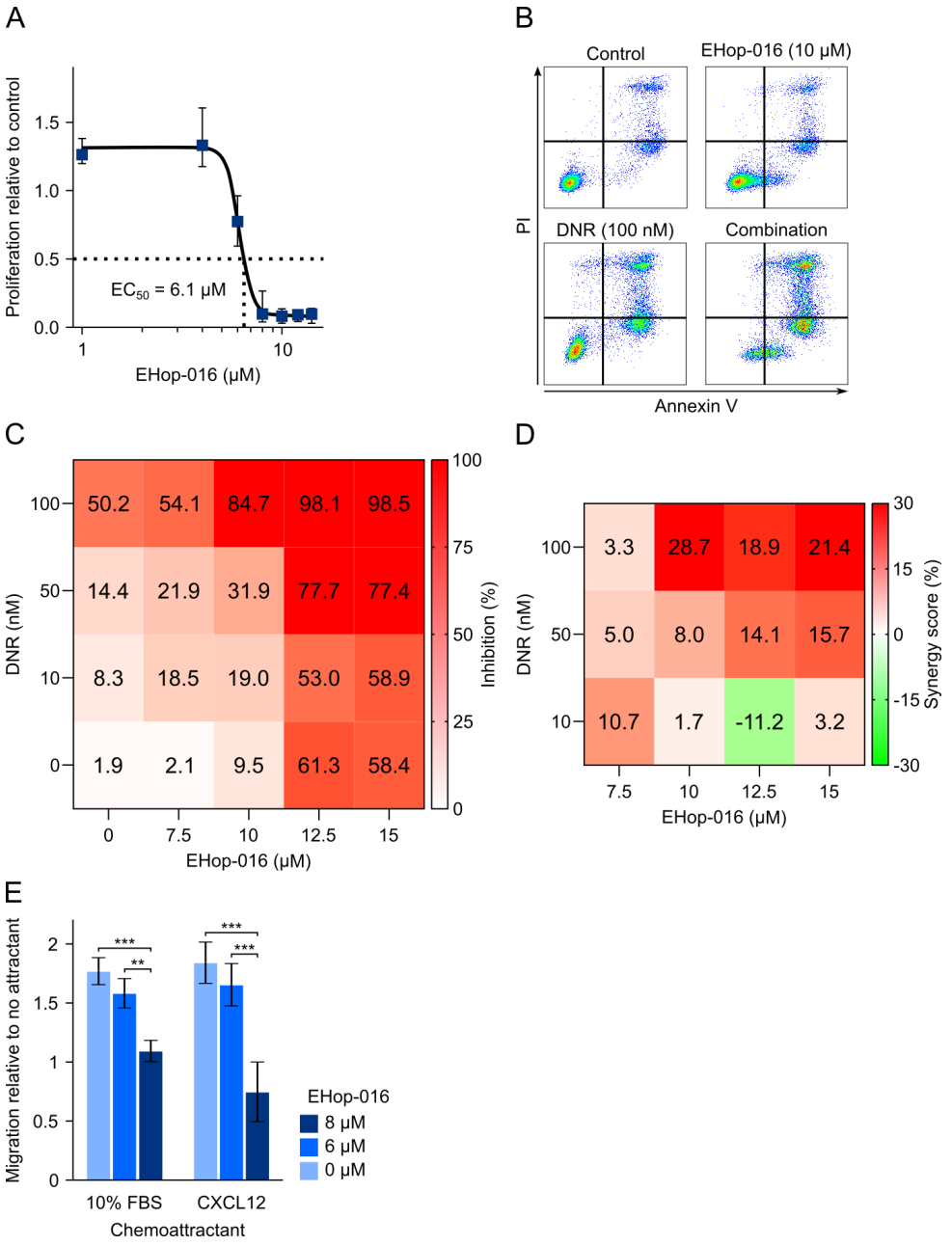

Figure 1 – EHop-016 induces cell death and attenuates migration of MOLM-13 cells *in vitro*. A: The antiproliferative effect of EHop-016 on MOLM-13 cells after 48 h incubation was measured using a ^{3}H-thymidine assay. The data represented are relative to the untreated control and are the median of three replicates with a 95% confidence interval. **B-D:** The reduction of viability and the induction of apoptosis and necrosis were evaluated using flow cytometric analyses on Annexin V/Propidium iodide (PI) stained cells. Before analysis, MOLM-13 cells were incubated for 48 h with EHop-016, Daunorubicin (DNR), or a combination. Gating to separate Annexin V and PI negative and positive cells was performed as shown in **B**. A heatmap of the percentage of non-viable cells (inhibition) according to different combination treatments is presented in **C**, each performed in duplicate. **D:** The synergy score was calculated as the deviation from the theoretical inhibition calculated

by the Bliss method. Here, a synergy score of ±10% indicates an additive interaction, below -10% an antagonistic interaction, and above 10% synergy. **E:** The ability of EHop-016 to inhibit migration was evaluated using a transwell migration assay. The MOLM-13 cells were incubated for 20 h with a deficit of FBS (0.5%) and with or without EHop-016. Following incubation, the cells were left for six h to migrate to a lower well containing 10% FBS or 100 ng/ml CXCL12 as chemoattractants or cell medium without FBS as a negative control. The ratio of migrated cells relative to the control is presented as the mean and standard deviation (n = 3). * $p \leq 0.05$, ** $p \leq 0.01$, *** $p \leq 0.001$, two-way ANOVA with Fisher's Least Significant Difference (LSD) test.

Toxic effects of EHop-016 on zebrafish larvae

Before commencing the efficacy studies on zebrafish larvae, we needed to establish the maximum tolerable dose (MTD) of EHop-016 in zebrafish larvae. The toxic effects were investigated for both in-water and intravenous administration. In-water administration started at two dpf. Administration of 100 µM EHop-016 in E3 medium resulted in the death of all larvae during the first 24 hours of exposure (Figure 2A). Of the eight larvae treated with 50 µM, three were found dead two days after administration, and the remaining died three days after drug administration. In the larvae surviving 50 µM treatment until two days after administration, we observed adverse effects on the circulatory system. One of the surviving larvae had a cardiac arrest and subsequently no blood circulation. Additionally, two other larvae had heartbeats but no blood circulation, and an obstruction was detected in the ventral tail area (Figure 2B). None of the larvae exposed to EHop-016 concentrations below 50 µM died or showed signs of toxicity like circulatory defects during the experiment. Additionally, zebrafish larvae were injected intravenously with 4 nl 100 µM EHop-016, 10 µM EHop-016, or Milli-Q water at two dpf. No toxic effects were observed in these larvae until euthanasia at five dpf. Based on these results, we determined the MTD of EHop-016 in zebrafish larvae to be 25 µM when administered in-water and at least 100 µM as one 4 nl bolus intravenous injection.

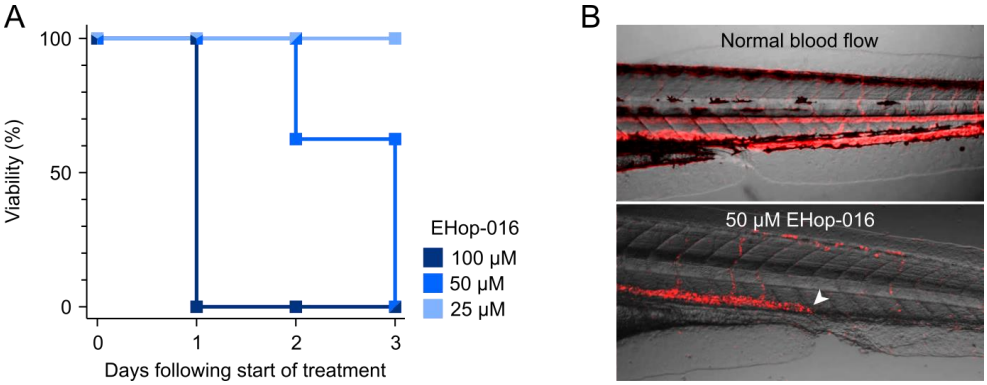

Figure 2 – Toxicity of EHop-016 in zebrafish larvae. Zebrafish larvae were dechorionated at two dpf and placed in a 96-well plate with one larva per well. EHop-016 diluted to different concentrations in E3 medium was added to each well. The zebrafish larvae were screened daily for visual toxic effects until euthanasia at five dpf. **A**: Viability of the zebrafish larvae incubated in different concentrations of EHop-016 for three days. N = 8 larvae in each group. **B:** Visualization of normal and obstructed blood flow from video recording of larvae without treatment or treated with 50 µM EHop-016 for 24 h. Visualization was done by overlaying the standard deviation in pixel intensity across time frames (red) on a still video frame. Normal blood flow is shown above, while a larva treated with 50 µM EHop-016 is shown below. The white arrow marks the point of obstructed blood flow in the caudal hematopoietic tissue (CHT).

EHop-016 reduces the accumulation of MOLM-13 cells in the caudal hematopoietic tissue

To investigate how EHop-016 treatment affected cell migration *in vivo*, a 12-hour timelapse was recorded on zebrafish transplanted with fluorescently labeled MOLM-13 cells. We have previously shown that MOLM-13 cells accumulate to the CHT (see Figure 3A for localization in the larvae) after intravenous injection (Førde et al. 2022), where hematopoiesis occurs in the zebrafish larvae. We found that MOLM-13 cells accumulated in the CHT during the first 12 hours after transplant (Figure 3B and C. However, in larvae treated with 20 µM EHop-016 in-water, there was less accumulation of cells in the CHT. A comparison of the number of cells in the CHT of EHop-016-treated larvae at 12 hours and the start of the experiment gave no significance (paired t-test). Untreated larvae had significantly higher number of cells in the CHT than EHop-016 treated larvae over the duration of the experiment ($p < 0.01$, two-way ANOVA).

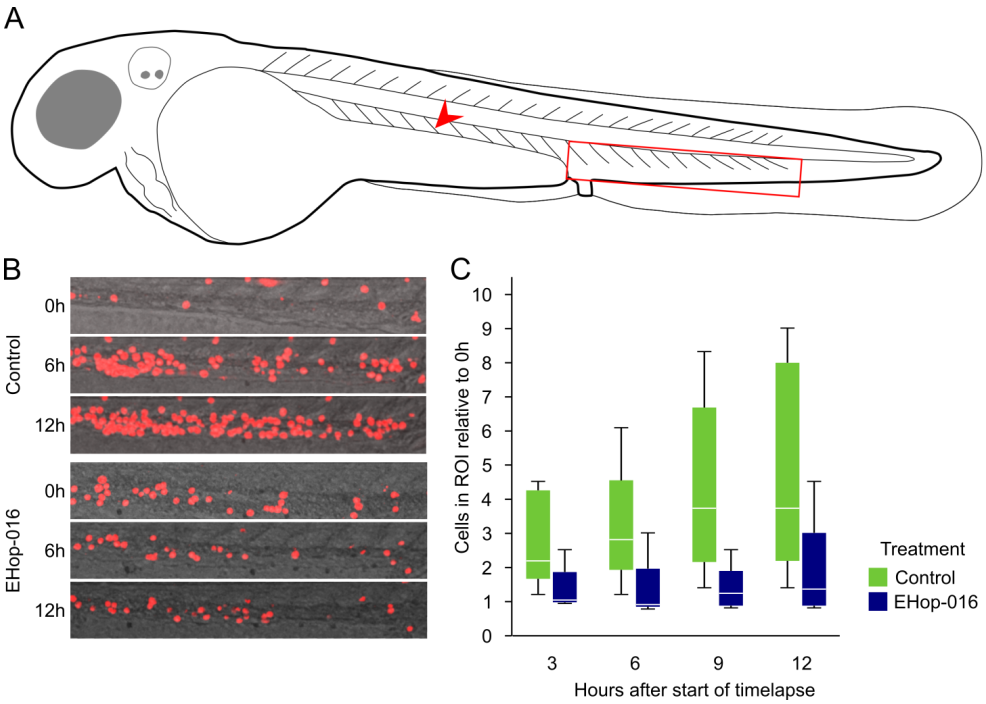

Figure 3 – Inhibited migration of injected MOLM-13 cells to the CHT. Zebrafish larvae were dechorionated and incubated in E3 medium with or without 20 µM EHop-016. The following day, the zebrafish larvae were injected with MOLM-13 cells stained using CellTracker™ Deep Red. Immediately following cell transplantation, a 12-hour timelapse was conducted with images of the tail regions acquired every 10 minutes using confocal microscopy. The number of transplanted cancer cells was determined in a 724 µm x 121 µm (600 pix x 100 pix) region in the tail including the CHT. This region of interest (ROI) is illustrated as a red rectangle in **A**, and a red arrow indicates the injection site. In **B:** confocal images show accumulation of MOLM-13 cells in the CHT of a control and an EHop-016-treated larva at zero, six, and 12 h after injection. **C**: For each zebrafish larva, the count of MOLM-13 cells in the ROI was calculated relative to the count at the start of the timelapse. The data are shown as boxplots, n = 5. See main text for description of statistical significances.

The combination of EHop-016 and DNR reduces the tumor burden *in vivo*

The proapoptotic effect of EHop-016 by itself and in combination with DNR was evaluated in zebrafish larvae injected with MOLM-13 cells. To ensure optimal drug exposure to EHop-016, we utilized pretreatment of both larvae and cancer cells. Progression of tumor burden can be represented as AML cell count or total volume of AML cells, both relative to the count of AML cells before treatment. The two approaches were used since the segmentation process can in some cases lead to nearby cells being counted as one, thereby influencing the cell count, while cell volume measure can sometimes be affected by changes in fluorescence intensity. The relative change of cell count or total volume of MOLM-13 cells (Figure 4A and C, respectively) was calculated to find the tumor progression over the first 24 hours. Of the four treatments (vehicle control, DNR, EHop-016, and combination of DNR and EHop-016), only the combination of DNR and EHop-016 significantly reduced the tumor burden (p = 0.043 for cell count and 0.018 for cell volume, paired sample t-test, see Figure 4A and C respectively). No significant changes in tumor burden were found in control larvae or larvae treated with EHop-016 (20 µM in-water) alone. There was an apparent decrease in tumor burden in larvae treated with DNR without EHop-016 (4 nl 1 mM injection of DNR), but this was not significant when compared with tumor burden before treatment (paired sample t-test: p = 0.12 for count and 0.054 for volume).

To compare how the different treatments affected tumor burden, the relative changes in MOLM-13 cell count and total volume from two dpf to three dpf were log-transformed. Compared to the control group, the groups receiving treatment, except volume measurements of EHop-016 alone, exhibited a significantly lower AML cell count and total volume (Figure 4B and D). Furthermore, the larvae treated with EHop-016 and DNR in combination had significantly lower total cell volume than those treated with either drug alone ($p < 0.001$ compared with EHop-016 and p = 0.007 compared with DNR) (Figure 4D). Taken together, these data show that combining DNR with EHop-016 is more efficient than either drug alone.

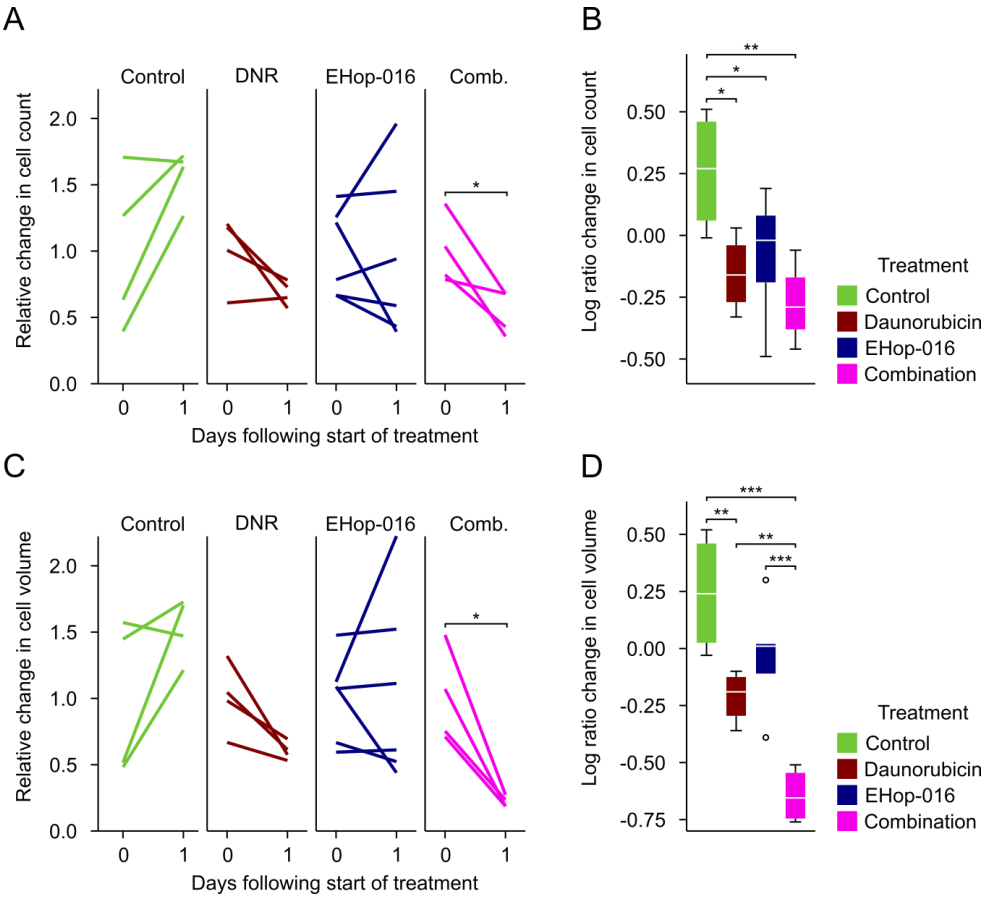

Figure 4 – *In vivo* efficacy of EHop-016 and DNR alone or in combination. Zebrafish larvae at one dpf were dechorionated and divided into four groups: Control without treatment, single treatment with EHop-016 or DNR, and a combined treatment of both drugs. Larvae in the EHop-016 and combination group were pre-treated with 20 µM EHop-016 in E3 medium for 24 h before injection with MOLM-13 cells stained with CellTracker™ Deep Red. The cells in the EHop-016 and combination group were also pre-treated with 5 µM EHop-016. At two dpf, the fluorescently stained cells were intravenously injected into the zebrafish larvae. Larvae in the DNR and combination group were injected with 4 nl 1 mM DNR in PBS. Images were acquired at two dpf and three dpf using confocal microscopy. The resulting images were processed as described in the methods section and in (Førde et al. 2022). Larvae that had ten or fewer cancer cells immediately after injection were excluded. The change in cancer cell count and total cancer cell volume are shown in **A** and **C**, respectively, with larvae in each group represented by a unique color. All values were taken relative to the respective average for all larvae in the group at two dpf. A log-transform of the relative changes in each group for cancer cell count and volume are shown in boxplots **B** and **D**, respectively. n = 4 for all groups except EHop-016, where n = 6. For statistical analysis, a paired samples test was performed for the line plots in A and C, and an ANOVA with Fisher's LSD test in B and D. * $p \leq 0.05$, ** $p \leq 0.01$, *** $p \leq 0.001$. If no significance is indicated, $p > 0.05$, i.e. not significant.

Discussion

In this study, we demonstrate the potential of pharmacological inhibition of Rac1 in AML therapy using the molecule EHop-016 on MOLM-13 AML cells *in vitro* and *in vivo*. The zebrafish larva was chosen as a model system for the *in vivo* studies, particularly since they allow for high-resolution visualization of single-cell migration. EHop-016 was administered to the larvae by adding it to the water. The observed toxic effects of in-water treatment indicate uptake of the drug. Even though it is difficult to precisely determine the concentration in the zebrafish larval circulation after in-water administration, it will reduce the unnecessary stress of repeated drug injections and ensure continuous exposure to the drug. This amends for the short half-life of EHop-016 found in mice, about 4.5 h after intraperitoneal administration, presumably due to combined renal and hepatic elimination (Humphries-Bickley et al. 2015).

In the zebrafish larvae, the CHT is the major site of hematopoiesis between two to five dpf, thereby serving as a likely migration target for leukemic cancer cells (Gore et al. 2018), including MOLM-13 (Førde et al. 2022). Our finding that EHop-016 inhibits AML cell migration *in vitro* (Figure 1E) was also confirmed *in vivo* (Figure 3). However, whether the observed reduction of accumulation in the CHT was due to altered attraction or anchoring to the CHT, altered migration of the cells, or modulated cell-to-cell adhesion in the vascular endothelium is not known (Timmerman et al. 2015). While zebrafish have endothelial and stromal cells producing chemoattractants like CXCL12, this production is low in the early larval stage (Glass et al. 2011), which could suggest that our observations are due to generally reduced cell motility rather than reduced response to chemoattractants.

The antiproliferative and proapoptotic effects of EHop-016 *in vitro* are in line with reported findings on other cancer cells. EHop-016 decreased the cell viability and induced apoptosis on breast cancer cell lines (Borrero-García et al. 2021) and gallbladder cancer cell lines (Jiang et al. 2021). Likewise, EHop-016 reduced the tumor burden in a breast cancer mouse model (Castillo-Pichardo et al. 2014). Our study demonstrates that EHop-016 potentiates the effect of DNR (Figure 1D) and induces a significantly decreased tumor burden *in vivo* in the combination treatment group (Figure 4). Combination treatment was previously successful with EHop-016 and paclitaxel in a lung cancer cell line (Yang et al. 2019), with NSC23766 and cisplatin and carboplatin in breast and lung cancer cell lines (Li et al. 2020) and with Eht1864 and DNR in the AML cell line OCI-AML3 (Ramos et al. 2022). No *in vivo* experiments with the combination of Rac1 inhibition and anthracyclines have previously been reported. Still, our data suggests that this may be a promising therapeutic strategy, which merits investigations in other cancers as well.

The concept of inhibiting leukemic cell attachment to the bone marrow niche combined with chemotherapy has been investigated using other targets and drugs. In AML, one of the obstacles for successful treatment is insufficient eradication of the quiescent leukemic stem cells (LSC) from the bone marrow niche or extramedullary sites, where they evade the toxic effects of chemotherapy, leading to a later relapse or refractory disease (Wang et al. 2013). The CXCR4 antagonist BL-8040 is currently being investigated with cytarabine in clinical trials for AML to induce mobilization of leukemic blasts into the peripheral blood (Borthakur et al. 2021). DeAngelo and colleagues have reported the encouraging clinical results of an inhibitor of the cell adhesion molecule E-selectin/CD62E, also present in leukemic cells and LSCs (DeAngelo et al. 2022). However, the advantage of targeting a downstream effector molecule, like Rac1, is that it affects events downstream of several adhesion molecules and receptors. Thus, inhibition might both reduce the homing to the hematopoietic niche and induce a more vigorous mobilization of leukemic cells and the LSC, as seen by Jia and colleagues when they combined targeting of CXCR4 and E-selectin/CD62E *in vitro* in AML (Jia et al. 2023).

At an in-water concentration of 50 µM, toxic effects occurred in the zebrafish larvae, manifested as reduced and sometimes blocked blood flow (Figure 2B). This might relate to the decreased endothelial tube formation, which has been demonstrated on umbilical vein endothelial cells after 24 h treatment with EHop-016 (Castillo-Pichardo et al. 2014). This study also reported a reduction in the number of blood vessels on the surface of breast cancer tumors in a mouse model treated with EHop-016. While no toxicity was noted in the adult mice, our model's zebrafish larvae are still undergoing development with substantial angiogenesis, which could increase their susceptibility to this effect. We have no indications that the reduced blood circulation is due to aggregation of thrombocytes, present in zebrafish from 36 h post fertilization (Gregory and Jagadeeswaran 2002). On the contrary, the first-generation Rac1-inhibitor NSC23766 inhibited platelet aggregation and lamellipodia formation by thrombin (Akbar et al. 2007).

No Rac1 inhibitor has so far entered a clinical trial. The short half-life of EHop-016 in mice might suggest a twice-a-day dosing regimen, an infusion, or a controlled-release formulation to maintain sufficient time for the drug to exert the desired effect on AML cells. Our experiment was performed with DNR in combination with EHop-016, but possible longer-term effects with other drug combinations, such as both DNR and cytarabine or a BCL-2 inhibitor, could reveal even greater therapeutic potential.

Conclusion

The signaling molecule Rac1 is an interesting target in AML, being implicated in several cellular processes and downstream of many receptors. The Rac1 inhibitor EHop-016 can attenuate the migration of MOLM-13 cells to the CHT in a zebrafish larva model and likely therefore enhance the proapoptotic effect of DNR both *in vitro* and *in vivo*. Our research supports the notion from other experiments that Rac1 targeting can contribute to improved therapy outcomes in AML and should be further evaluated in *in vivo* studies.

Acknowledgements

We thank the zebrafish facility at the University of Bergen for access to E3 medium and zebrafish for breeding.

Funding

This research received funding from Western Norway Regional Health Authority to ALH (Grant no. F-11001) and JLF (Grant no. F-12533), and from the Norwegian Society for Children's Cancer to LH (Grant Nos. 180007 and 190004). The funders had no role in study design, analysis or preparation of the manuscript.

CRediT authorship contribution statement

Anette L. Hemsing: Conceptualization, Methodology, Investigation, Formal analysis, Visualization, Writing original draft, review & editing

Jan-Lukas Førde: Conceptualization, Methodology, Software, Investigation, Formal analysis, Visualization, Writing original draft, review & editing

Håkon Reikvam: Conceptualization, Methodology, Resources and funding

Lars Herfindal: Conceptualization, Methodology, Formal analysis, Resources and funding, Writing - review & editing

Declaration of Competing Interest

The authors declare that they have no known competing financial interests or personal relationships that could have appeared to influence the work reported in this paper.

Publication bibliography

Akbar, H.; Kim, J.; Funk, K.; Cancelas, J. A.; Shang, X.; Chen, L. et al. (2007): Genetic and pharmacologic evidence that Rac1 GTPase is involved in regulation of platelet secretion and aggregation. In *Journal of thrombosis and haemostasis : JTH* 5 (8), pp. 1747–1755. DOI: 10.1111/j.1538-7836.2007.02646.x.

Bertoli, Sarah; Tavitian, Suzanne; Huynh, Anne; Borel, Cécile; Guenounou, Sarah; Luquet, Isabelle et al. (2017): Improved outcome for AML patients over the years 2000-2014. In *Blood Cancer Journal* 7 (12), p. 635. DOI: 10.1038/s41408-017-0011-1.

Bliss, C. I. (1939): The Toxicity of Poisons Applied Jointly. In *Annals of Applied Biology* 26 (3), pp. 585–615. DOI: 10.1111/j.1744-7348.1939.tb06990.x.

Borrero-García, Luis D.; Del Mar Maldonado, Maria; Medina-Velázquez, Julia; Troche-Torres, Angel L.; Velazquez, Luis; Grafals-Ruiz, Nilmary; Dharmawardhane, Suranganie (2021): Rac inhibition as a novel therapeutic strategy for EGFR/HER2 targeted therapy resistant breast cancer. In *BMC Cancer* 21 (1), p. 652. DOI: 10.1186/s12885-021-08366-7.

Borthakur, Gautam; Ofran, Yishai; Tallman, Martin S.; Foran, James; Uy, Geoffrey L.; DiPersio, John F. et al. (2021): BL-8040 CXCR4 antagonist is safe and demonstrates antileukemic activity in combination with cytarabine for the treatment of relapsed/refractory acute myelogenous leukemia: An open-label safety and efficacy phase 2a study. In *Cancer* 127 (8), pp. 1246–1259. DOI: 10.1002/cncr.33338.

Cancelas, Jose A.; Jansen, Michael; Williams, David A. (2006): The role of chemokine activation of Rac GTPases in hematopoietic stem cell marrow homing, retention, and peripheral mobilization. In *Experimental Hematology* 34 (8), pp. 976–985. DOI: 10.1016/j.exphem.2006.03.016.

Cancelas, Jose A.; Lee, Andrew W.; Prabhakar, Rethinasamy; Stringer, Keith F.; Zheng, Yi; Williams, David A. (2005): Rac GTPases differentially integrate signals regulating hematopoietic stem cell localization. In *Nat Med* 11 (8), pp. 886–891. DOI: 10.1038/nm1274.

Castillo-Pichardo, Linette; Humphries-Bickley, Tessa; La Parra, Columba de; Forestier-Roman, Ingrid; Martinez-Ferrer, Magaly; Hernandez, Eliud et al. (2014): The Rac Inhibitor EHop-016 Inhibits Mammary Tumor Growth and Metastasis in a Nude Mouse Model. In *Translational Oncology* 7 (5), pp. 546–555. DOI: 10.1016/j.tranon.2014.07.004.

Choi, Tae-Young; Choi, Tae-Ik; Lee, Yu-Ri; Choe, Seong-Kyu; Kim, Cheol-Hee (2021): Zebrafish as an animal model for biomedical research. In *Exp Mol Med* 53 (3), pp. 310–317. DOI: 10.1038/s12276-021-00571-5.

DeAngelo, Daniel J.; Jonas, Brian A.; Liesveld, Jane L.; Bixby, Dale L.; Advani, Anjali S.; Marlton, Paula et al. (2022): Phase 1/2 study of uproleselan added to chemotherapy in patients with relapsed or refractory acute myeloid leukemia. In *Blood* 139 (8), pp. 1135–1146. DOI: 10.1182/blood.2021010721.

Førde, Jan-Lukas; Reiten, Ingeborg Nerbø; Fladmark, Kari Espolin; Kittang, Astrid Olsnes; Herfindal, Lars (2022): A new software tool for computer assisted in vivo high-content analysis of transplanted fluorescent cells in intact zebrafish larvae. In *Biology open* 11 (12). DOI: 10.1242/bio.059530.

Garitano-Trojaola, Andoni; Sancho, Ana; Götz, Ralph; Eiring, Patrick; Walz, Susanne; Jetani, Hardikkumar et al. (2021): Actin cytoskeleton deregulation confers midostaurin resistance in FLT3-mutant acute myeloid leukemia. In *Commun Biol* 4 (1), p. 799. DOI: 10.1038/s42003-021-02215-w.

Glass, Tiffany J.; Lund, Troy C.; Patrinostro, Xiaobai; Tolar, Jakub; Bowman, Teresa V.; Zon, Leonard I.; Blazar, Bruce R. (2011): Stromal cell-derived factor-1 and hematopoietic cell homing in an adult zebrafish model of hematopoietic cell transplantation. In *Blood* 118 (3), pp. 766–774. DOI: 10.1182/blood-2011-01-328476.

Gore, Aniket V.; Pillay, Laura M.; Venero Galanternik, Marina; Weinstein, Brant M. (2018): The zebrafish: A fintastic model for hematopoietic development and disease. In *Wiley interdisciplinary reviews. Developmental biology* 7 (3), e312. DOI: 10.1002/wdev.312.

Gregory, Michael; Jagadeeswaran, Pudur (2002): Selective labeling of zebrafish thrombocytes: quantitation of thrombocyte function and detection during development. In *Blood Cells, Molecules, and Diseases* 28 (3), pp. 418–427. DOI: 10.1006/bcmd.2002.0527.

Hemsing, Anette Lodvir; Rye, Kristin Paulsen; Hatfield, Kimberley Joanne; Reikvam, Håkon (2022): NPM1-Mutated Patient-Derived AML Cells Are More Vulnerable to Rac1 Inhibition. In *Biomedicines* 10 (8). DOI: 10.3390/biomedicines10081881.

Humphries-Bickley, Tessa; Castillo-Pichardo, Linette; Corujo-Carro, Francheska; Duconge, Jorge; Hernandez-O'Farrill, Eliud; Vlaar, Cornelis et al. (2015): Pharmacokinetics of Rac inhibitor EHop-016 in mice by ultra-performance liquid chromatography tandem mass spectrometry. In *Journal of chromatography. B, Analytical technologies in the biomedical and life sciences* 981-982, pp. 19–26. DOI: 10.1016/j.jchromb.2014.12.021.

Jia, Yannan; Zhang, Weiguo; Basyal, Mahesh; Chang, Kyung Hee; Ostermann, Lauren; Burks, Jared K. et al. (2023): FLT3 inhibitors upregulate CXCR4 and E-selectin ligands via ERK suppression in AML cells and CXCR4/E-selectin inhibition enhances anti-leukemia efficacy of FLT3-targeted therapy in AML. In *Leukemia* 37 (6), pp. 1379–1383. DOI: 10.1038/s41375-023-01897-x.

Jiang, Ze-Bin; Ma, Bing-Qiang; Feng, Zongfeng; Liu, Shao-Guang; Gao, Peng; Yan, Hui-Ting (2021): miR-365 inhibits the progression of gallbladder carcinoma and predicts the prognosis of Gallbladder carcinoma patients. In *Cell cycle (Georgetown, Tex.)* 20 (3), pp. 308–319. DOI: 10.1080/15384101.2021.1874694.

Kimmel, C. B.; Ballard, W. W.; Kimmel, S. R.; Ullmann, B.; Schilling, T. F. (1995): Stages of embryonic development of the zebrafish. In *Developmental dynamics : an official publication of the American Association of Anatomists* 203 (3), pp. 253–310. DOI: 10.1002/aja.1002030302.

Li, Qingjian; Qin, Tao; Bi, Zhuofei; Hong, Huangming; Ding, Lin; Chen, Jiewen et al. (2020): Rac1 activates non-oxidative pentose phosphate pathway to induce chemoresistance of breast cancer. In *Nat Commun* 11 (1), p. 1456. DOI: 10.1038/s41467-020-15308-7.

Lichtman, Marshall A. (2013): A historical perspective on the development of the cytarabine (7days) and daunorubicin (3days) treatment regimen for acute myelogenous leukemia: 2013 the 40th anniversary of 7+3. In *Blood cells, molecules & diseases* 50 (2), pp. 119–130. DOI: 10.1016/j.bcmd.2012.10.005.

Matsuo, Y.; MacLeod, R. A.; Uphoff, C. C.; Drexler, H. G.; Nishizaki, C.; Katayama, Y. et al. (1997): Two acute monocytic leukemia (AML-M5a) cell lines (MOLM-13 and MOLM-14) with interclonal phenotypic heterogeneity showing MLL-AF9 fusion resulting from an occult chromosome insertion, ins(11;9)(q23;p22p23). In *Leukemia* 11 (9), pp. 1469–1477. DOI: 10.1038/sj.leu.2400768.

Montalvo-Ortiz, Brenda L.; Castillo-Pichardo, Linette; Hernández, Eliud; Humphries-Bickley, Tessa; La Mota-Peynado, Alina de; Cubano, Luis A. et al. (2012): Characterization of EHop-016, novel small molecule inhibitor of Rac GTPase. In *Journal of Biological Chemistry* 287 (16), pp. 13228–13238. DOI: 10.1074/jbc.M111.334524.

Ramos, Débora Felícia Vieira; Mancuso, Rubia Isler; Contieri, Bruna; Duarte, Adriana; Paiva, Luciana; Melo Carrilho, Jeferson de et al. (2022): Rac GTPases in acute myeloid leukemia cells: Expression profile and biological effects of pharmacological inhibition. In *Toxicology and applied pharmacology* 442, p. 115990. DOI: 10.1016/j.taap.2022.115990.

Schindelin, Johannes; Arganda-Carreras, Ignacio; Frise, Erwin; Kaynig, Verena; Longair, Mark; Pietzsch, Tobias et al. (2012): Fiji: an open-source platform for biological-image analysis. In *Nature methods* 9 (7), pp. 676–682. DOI: 10.1038/nmeth.2019.

Shutes, Adam; Onesto, Cercina; Picard, Virginie; Leblond, Bertrand; Schweighoffer, Fabien; Der, Channing J. (2007): Specificity and mechanism of action of EHT 1864, a novel small molecule inhibitor of Rac family small GTPases. In *The Journal of biological chemistry* 282 (49), pp. 35666–35678. DOI: 10.1074/jbc.M703571200.

Stapnes, Camilla; Døskeland, Anne P.; Hatfield, Kimberley; Ersvaer, Elisabeth; Ryningen, Anita; Lorens, James B. et al. (2007): The proteasome inhibitors bortezomib and PR-171 have antiproliferative and proapoptotic effects on primary human acute myeloid leukaemia cells. In *British journal of haematology* 136 (6), pp. 814–828. DOI: 10.1111/j.1365-2141.2007.06504.x.

Timmerman, Ilse; Heemskerk, Niels; Kroon, Jeffrey; Schaefer, Antje; van Rijssel, Jos; Hoogenboezem, Mark et al. (2015): A local VE-cadherin and Trio-based signaling complex stabilizes endothelial junctions through Rac1. In *J Cell Sci* 128 (16), pp. 3041–3054. DOI: 10.1242/jcs.168674.

Tulotta, Claudia; Stefanescu, Cristina; Beletkaia, Elena; Bussmann, Jeroen; Tarbashevich, Katsiaryna; Schmidt, Thomas; Snaar-Jagalska, B. Ewa (2016): Inhibition of signaling between human CXCR4 and zebrafish ligands by the small molecule IT1t impairs the formation of triple-negative breast cancer early metastases in a zebrafish xenograft model. In *Disease models & mechanisms* 9 (2), pp. 141–153. DOI: 10.1242/dmm.023275.

Turley, Eva A.; Noble, Paul W.; Bourguignon, Lilly Y. W. (2002): Signaling properties of hyaluronan receptors. In *The Journal of biological chemistry* 277 (7), pp. 4589–4592. DOI: 10.1074/jbc.R100038200.

Wang, Jiying; Rao, Qing; Wang, Min; Wei, Hui; Xing, Haiyan; Liu, Hang et al. (2009): Overexpression of Rac1 in leukemia patients and its role in leukemia cell migration and growth. In *Biochemical and Biophysical Research Communications* 386 (4), pp. 769–774. DOI: 10.1016/j.bbrc.2009.06.125.

Wang, Ji-Ying; Yu, Pei; Chen, Shuying; Xing, Haiyan; Chen, Yirui; Wang, Min et al. (2013): Activation of Rac1 GTPase promotes leukemia cell chemotherapy resistance, quiescence and niche interaction. In *Molecular oncology* 7 (5), pp. 907–916. DOI: 10.1016/j.molonc.2013.05.001.

White, Richard Mark; Sessa, Anna; Burke, Christopher; Bowman, Teresa; LeBlanc, Jocelyn; Ceol, Craig et al. (2008): Transparent adult zebrafish as a tool for in vivo transplantation analysis. In *Cell stem cell* 2 (2), pp. 183–189. DOI: 10.1016/j.stem.2007.11.002.

Wu, Min; Li, Li; Hamaker, Max; Small, Donald; Duffield, Amy S. (2019): FLT3-ITD cooperates with Rac1 to modulate the sensitivity of leukemic cells to chemotherapeutic agents via regulation of DNA repair pathways. In *1* 104 (12), pp. 2418–2428. DOI: 10.3324/haematol.2018.208843.

Yang, Juze; Qiu, Qiongzi; Qian, Xinyi; Yi, Jiani; Jiao, Yiling; Yu, Mengqian et al. (2019): Long noncoding RNA LCAT1 functions as a ceRNA to regulate RAC1 function by sponging miR-4715-5p in lung cancer. In *Mol Cancer* 18 (1), p. 171. DOI: 10.1186/s12943-019-1107-y.

Yao, Kun; Liu, Hua; Yu, Shui; Zhu, Haohao; Pan, Jie (2022): Resistance to mutant IDH inhibitors in acute myeloid leukemia: Molecular mechanisms and therapeutic strategies. In *Cancer Letters* 533, p. 215603. DOI: 10.1016/j.canlet.2022.215603.

Zheng, Shuyu; Wang, Wenyu; Aldahdooh, Jehad; Malyutina, Alina; Shadbahr, Tolou; Tanoli, Ziaurrehman et al. (2022): SynergyFinder Plus: Toward Better Interpretation and Annotation of Drug Combination Screening Datasets. In *Genomics, proteomics & bioinformatics* 20 (3), pp. 587–596. DOI: 10.1016/j.gpb.2022.01.004.

Graphic design: Communication Division, UiB / Print: Skipnes Kommunikasjon AS

uib.no

ISBN: 9788230855829 (print)
9788230857625 (PDF)